Corso di Dottorato in Ingegneria dell'Innovazione Tecnologica
Dipartimento di Ingegneria
ING-IND/16- Tecnologie e Sistemi di Lavorazione

NEW PERSPECTIVES ON LIGHTWEIGHT SHEET METAL ALLOYS MANUFACTURING BY SINGLE POINT INCREMENTAL FORMING

IL DOTTORE
ING. MARCO GUCCIARDI

IL COORDINATORE
CHIAR.MO PROF. SALVATORE GAGLIO

IL TUTOR
CHIAR.MO PROF. LIVAN FRATINI

IL CO-TUTOR
CHIAR.MO PROF. GIANLUCA BUFFA

Table of contents

Acknowledgements

This dissertation is the outcome of my research carried out during the last three years at the Department of Engineering of the University of Palermo. First, I would like to thank my advisor, prof. Livan Fratini, together with prof. Gianluca Buffa, which supported me through my doctoral studies with their mentoring and guidance. I also gratefully thank prof. Hitomi Yamaguchi Greenslet, who hosted and helped me during my stay at the University of Florida. Thanks to all my colleagues and co-workers from the MTG and the NTML groups that assisted and accompanied me in this journey. Finally, many thanks to my family and friends who always supported and encouraged me.

Abstract

In the last decades, the use of lightweight alloys has been spreading in almost any industrial field thanks to the relevant weight reduction allowed by the use of such materials. On the other hand, lightweight alloys show poor formability at standard conditions. The conventional manufacturing processes, such as deep drawing process, result to be ineffective in imposing large deformations over these materials, limiting the complexity of obtained geometry. To overcome formability limitation affecting lightweight sheet metal alloys, new unconventional forming processes have been developed over the years. Among them, Incremental forming processes meet the current needs of industrial sector looking for flexibility, limited setup costs, high customization features for medium/small batches production. The Single Point Incremental Forming (SPIF) is an Incremental forming technique which locally deforms the workpiece by means of a tool mounted on CNC machine. The simplicity of the setup, together with enhanced formability limitations compared to conventional sheet metal process have drawn the attention of many researches and industrial areas. Nevertheless, the presence of a maximum wall angle (α) represents a limit to SPIF applications for parts characterized by steeper walls as, until now, no sound part can be obtained in a single forming step.

In this dissertation, two innovative SPIF variants are presented. Multi-Directional multi-path SPIF and Magnetic Field-Assisted SPIF (M-SPIF) are meant to extend formability limits of lightweight materials in conventional SPIF. Experimental and numerical campaigns are described to better evaluate the process mechanics, the influence of process parameters on the final results, stress and strain distribution of the formed parts.

Graphical Abstract
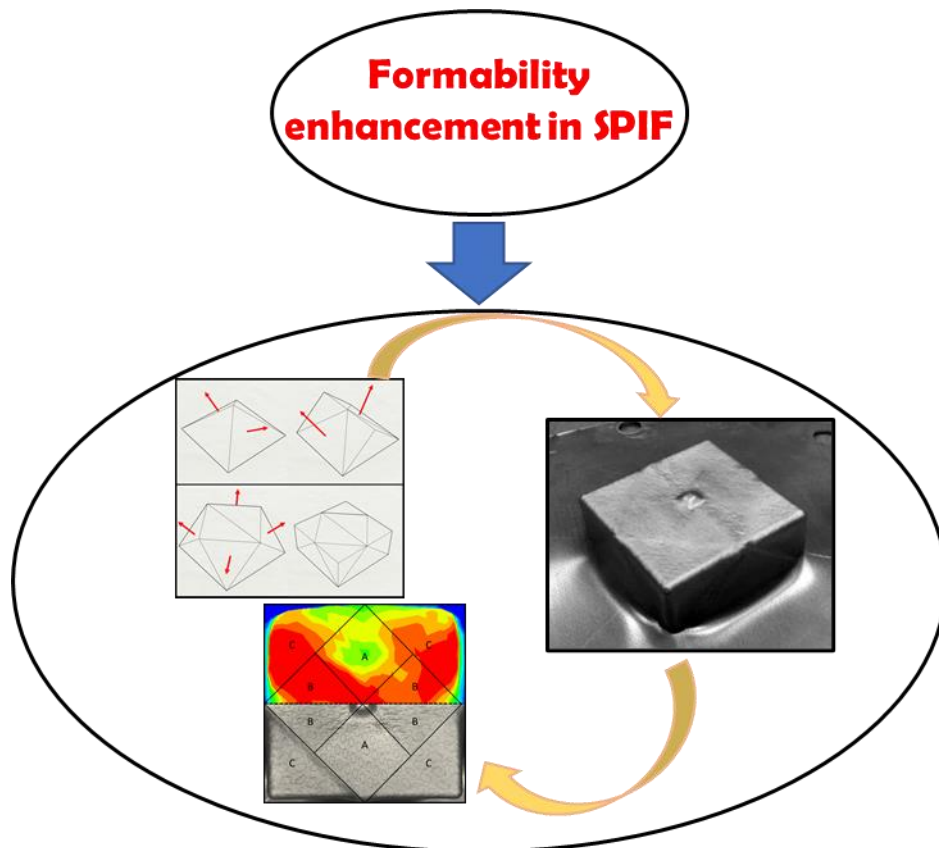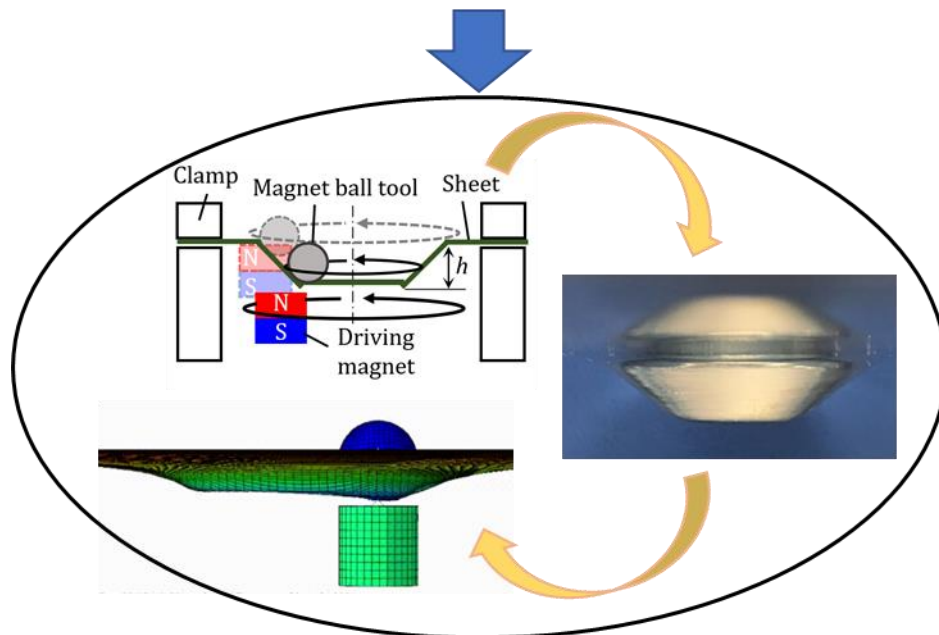
List of Abbreviations

AA	Aluminium Alloys
AHSS	Advanced High Strength Steel
ASIF	Asymmetric incremental Forming
c	clearance
CAD	Computer Aided Design
CAM	Computer Aided Manufacturing
CGA	Circular Grid Analysis
CNC	Computerized Numerical Control
EAF	Electrically-Assisted Forming
EHIF	Electric Hot Incremental Forming
EMIF	Electromagnetic Incremental Forming
FEM	Finite Elements Method
FFL	Fracture Limit Line
FLC	Forming Limit Curve
HDD	Hydroforming by deep Drawing
HSS	High Strength Steel
ISF	Incremental Sheet Forming
LASPIF	Laser-Assisted Single Point Incremental Forming
LDW	Limiting Drawing Ratio

MPF	Multipoint Forming Process
MPSF	Multipoint Sandwich Forming
M-SPIF	Magnetic Field-Assisted Single Point Incremental Forming
PID	Proportional-Integral-Derivative
RMB$_z$	Rigid Body Motion along Z
RPF	Rubber Pad Forming
SHF	Sheet Hydroforming Process
SPIF	Single Point Incremental Forming
VPF	Viscous Pressure Forming
α	Wall angle
Δh	change in truncated cone height
Δr	toolpath radius decrement
Δz	vertical stepdown

Dissertation Structure

This paragraph provides an overview of the dissertation's general structure in order to provide the links between the different sections and their respective contents. This dissertation is composed by five main chapters and each of them is further divided into paragraphs and subparagraphs numbered accordingly. The topics covered by each of these sections are briefly described in the following lines.
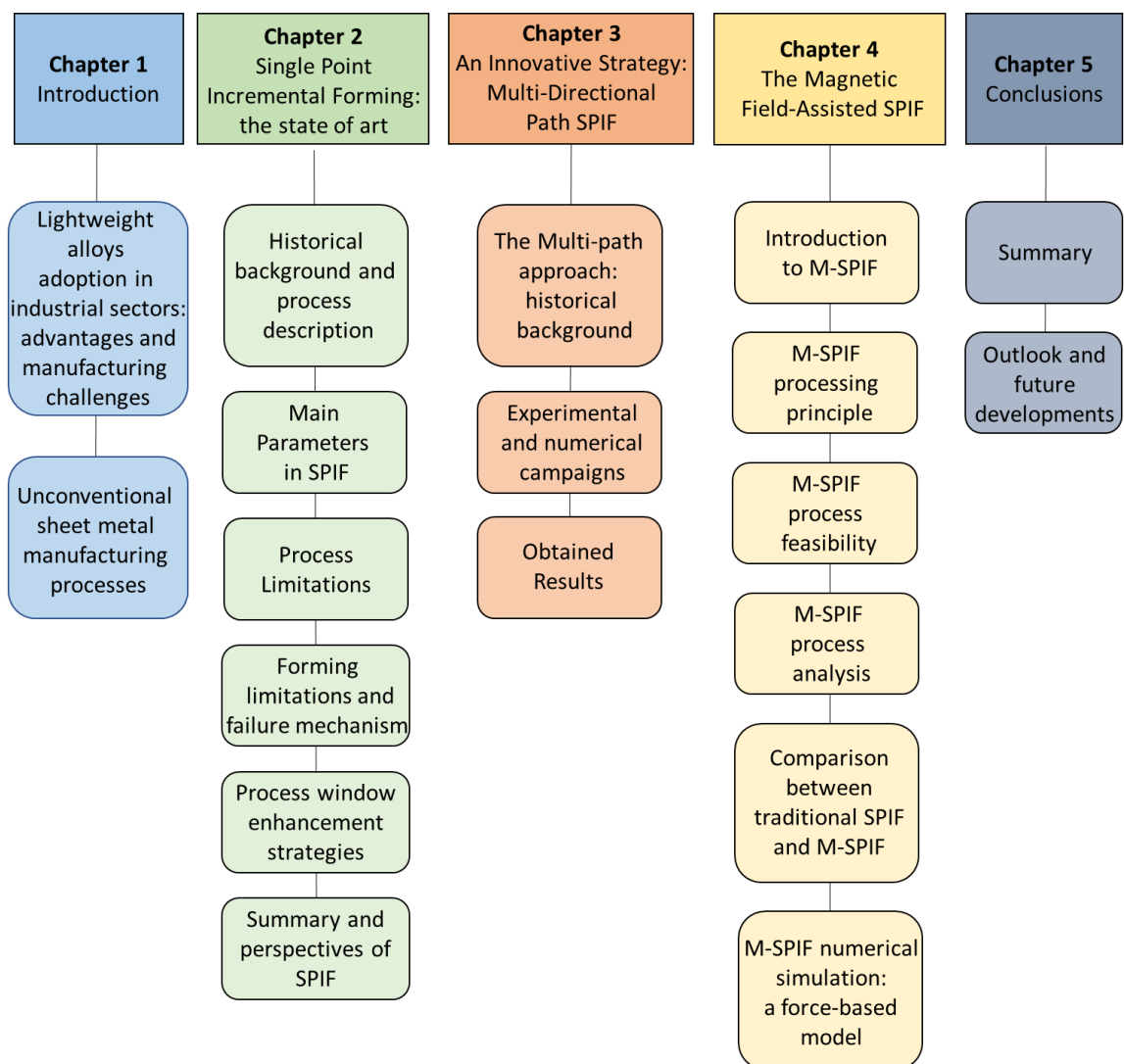

Figure 1 *Dissertation structure scheme.*

Chapter 1, namely "Introduction", deals with the general introduction to the lightweight sheet metal alloys adoption in different industrial sectors, with particular focus on the main developed unconventional sheet metal manufacturing processes to overcome formability limitations characterizing the above-mentioned material category.

Chapter 2, namely "Single Point Incremental Forming: the state of art", contains the analysis of the state of the art of the Single Point Incremental Forming, dealing with the process description (Paragraph 2.1), its main parameters (Paragraph 2.2), the main limitations affecting SPIF process (Paragraph 2.3), the forming limitations and the onset of failure (paragraph 2.4), the developed process window enhancement strategies over the years (Paragraph 2.5), finally focusing on the further evolutions of SPIF process (Paragraph 2.6).

Chapter 3, namely "An Innovative Strategy: Multi-Directional Path SPIF", focuses on the first of the innovative SPIF strategies being analysed: Multi-Directional Path SPIF [84]. After presenting the literature review in Paragraph 3.1, the experimental and numerical campaigns carried out to investigate the Multi-Directional Path SPIF process are hence described in Paragraph 3.2, while Paragraph 3.3 describes the obtained results in terms of final geometry, thickness and strain distribution.

Chapter 4, namely "The Magnetic Field-Assisted SPIF", focuses on the second brand-new SPIF strategy being analysed: Magnetic Field-Assisted SPIF (M-SPIF) [102], [103]. In Paragraph 4.1 the process background is described, then the processing principle is presented in Paragraph 4.2. Paragraph 4.3 presents the carried-out analysis after a first feasibility test, followed by a second experimental campaign focused on the process parameters analysis. In Paragraph 4.5 the experimental and numerical comparison between traditional SPIF and M-SPIF is provided, finally, the development of a force-based numerical model as a prediction tool for M-SPIF applications is provided in Paragraph 4.6.

Chapter 5, namely "Conclusion", provides a summary of the general results obtained for both Multi-Directional Path SPIF and M-SPIF processes, highlighting the advances of the state of the art enabled by the research presented in this dissertation (Paragraph 5.1). Paragraph 5.2 finally provides a general outlook of the investigated process, focusing on the possible future developments of this work.

1. Introduction

1.1. Lightweight alloys adoption in industrial sectors: advantages and manufacturing challenges

In the recent years, an increasing demand of so-called *lightweight materials* has been recorded in most of the main industrial sectors, such as aerospace and automotive ones. The reasons behind this widespread trend have to be searched for current needs and boundary conditions characterizing the abovementioned industrial areas. Both aerospace and automotive industries share the common target of lightweight components production, in order to manufacture complex structures with multiple features and materials, as well as to reduce energy and CO_2 emissions. Over the years, high-strength steel (HSS), aluminium, magnesium and titanium alloys have taken place of conventional materials, such as mild steel, in order to manufacture components with a higher *strength-to-weight* ratio. As reported from *Lihui et al.* [1], the adoption of advanced high-strength steel (AHSS) alloys for automotive chassis components has sharply increased to both reduce vehicle weight and improve safety. Figure 1.1 shows how AHSS steels are being used mainly in chassis components, such as the A-pillar, B-pillar, bumper, roof rail, rocker rail and tunnel. Noteworthy vehicle models and flagship companies have seen a wide and quick implementation of these advanced steels (Dual phase, martensitic and boron steels) in their production chains, such as the Mercedes C-class, jumping from 38% to 74% AHSS in its body redesign.
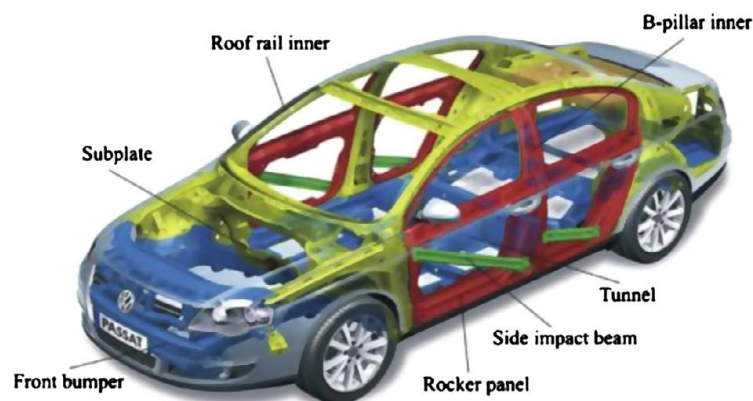

Figure 1.1 Adoption of HSS steels in body frame of a mid-class vehicle (Source: [1]).

Aluminium alloys represent the most widespread option as raw material for panel structures. The employed aluminium alloy type as well as its heat treatment, are depending on purpose(s) to be accomplished [2]. Some Al-alloys applications for automotive and aircraft industries, according to their mechanical properties, are reported in Table 1.1. Precipitation-hardened aluminium alloys, specifically AA7xxx family, are the main candidates for outer panel structures due to their good strength properties, which are furtherly increased from the typical T6 heat treatment for the automotive industry (Figure 1.2a).

Table 1.1 *Properties and application cases of typical aluminium alloys in automotive and aircraft industries (Source: [2]).*

Industry	Alloy grade	Main chemical composition	Density (kg/m³)	Strength/Density (Pa/(kg.m⁻³))	Applications
Automotive	AA5052	Al-Mg	2680	72,000	Interior panels and components, truck bumpers and body panels
	AA5754		2670	86,000	Inner body panels, splash guards, heat shields, air cleaner trays and covers, structural and weldable parts, load floor
	AA6016-T4	Al-Mg-Si	2700	81,500	Outer panels and structural sheets (Europe)
	AA6111-T4		2710	103,000	Outer and inner panels (North America)
	AA7020-T6	Al-Zn-Mg	2780	127,000	Potential applications for A pillar and B pillar
Aircraft	AA7055-T7751	Al-Zn-Mg	2860	222,000	Case of fuselage
	AA7075-T73		2810	180,000	Upper wing skins, stringers and horizontal/vertical stabilizers
	AA2024-T3	Al-Cu-Mg	2780	1,740,000	Upper wing structure
	AA2199-T8	Al-Cu-Li	2640	152,000	Fuselage and lower wing structure

On the aircraft industries side, AA7xxx and AA2xxx represent the best choices due to their high strength and decent corrosion resistance (Figure 1.2b). Nevertheless, corrosion resistance property of AA7xxx results to be poor at T6 condition with peak strength, making necessary the application of an over-aged treatment for these alloys, such as T73, in order to respect the all-condition aerospace standard requirements. Al-Li alloys, such as 2099, which exhibit low density, high stiffness and good fatigue resistance properties, are widely used in wing structures.
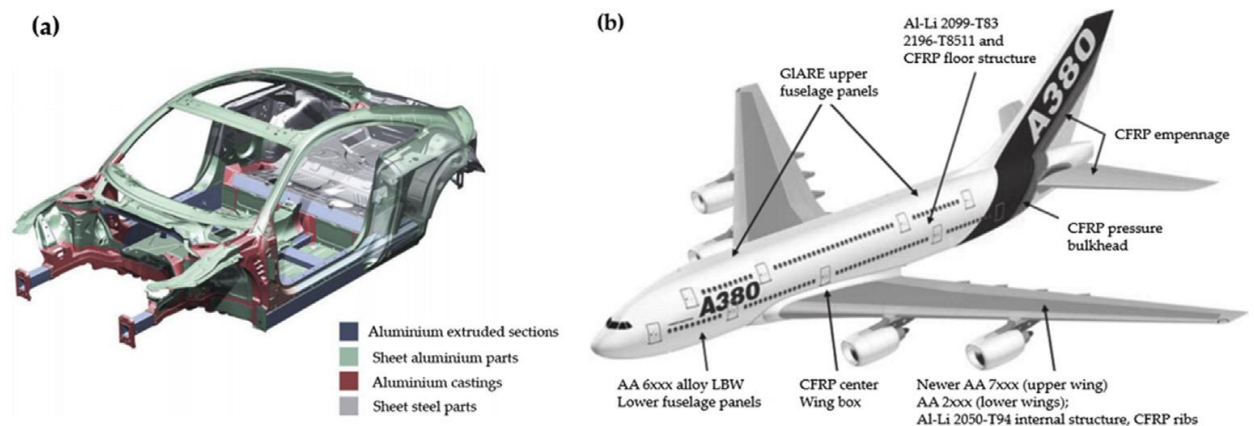
Figure 1.2 *Aluminium alloys applications in body structures manufacturing: a) automotive sector; b) aerospace sector (Source: [2]).*

Often limited by high costs, titanium alloys application has been recorded a wider and wider diffusion. This trend is not only justified by *light-weighting* purposes, but also the need to guarantee high mechanical properties at high temperatures as well as a high corrosion resistance in hostile environments [3]. Figure 1.3 shows some interesting titanium parts applications in automotive sector over the years. Higher-performance titanium alloys adoption for mufflers is justified by high temperatures and salt corrosion these components are constantly exposed to (Figure 1.4). For CORVETTE Z06 (by Chevrolet/GM) a titanium (Cp-TiGr.2) exhaust system was installed in 2001 to reduce mass, then improve performances. Titanium application resulted in a 11.7 kg dual muffler assembly, achieving a 41% weight reduction and enhancing performance standards. LFA by Lexus also applied a titanium muffler made of Ti-ASN with the high temperature salt damage corrosion in 2010.
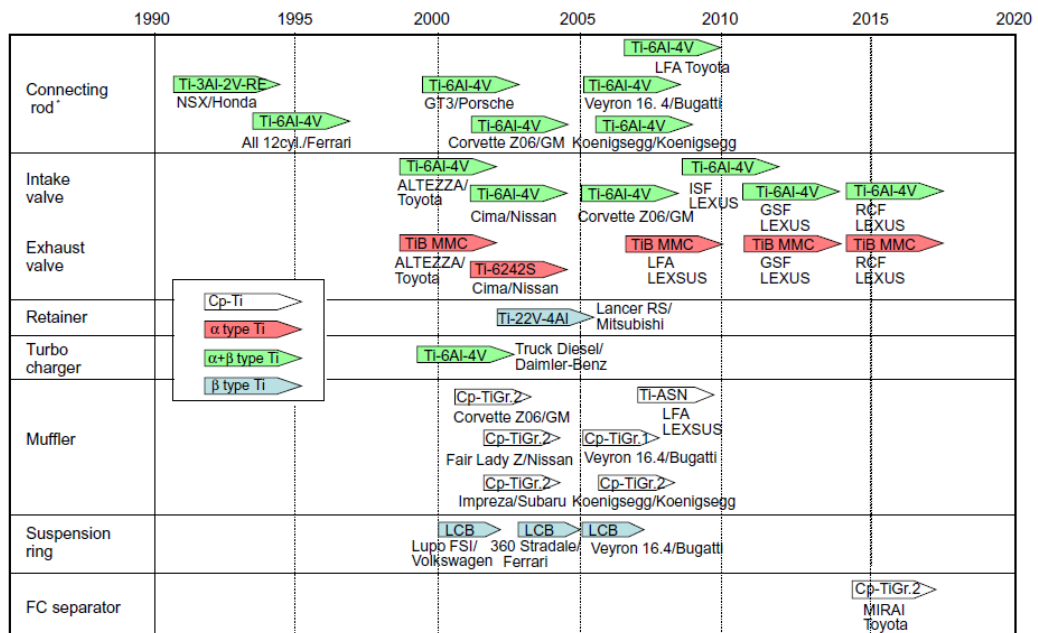

Figure 1.3 *Timeline of typical titanium parts application in the automotive sector (Source: [3]).*

Figure 1.4 *Commercial exhaust system made of titanium (Source: [3]).*

13

With the ongoing revolution involving powertrain systems, more and more components made of titanium have come up for hybrid vehicles (HVs), plug-in hybrid vehicles (PHVs), fuel cell vehicles (FCVs), and electric vehicles (EVs). A typical example of such new applications is the titanium fuel separator in the fuel cell (FC) installed within an FCV, which has to exhibit high specific strength for weight saving and high corrosion resistance due to severe working conditions. From this perspective, MIRAI (by Toyota), which has been commercially sold since 2016, shows a remarkable total amount of titanium per automobile (especially for engine components) if compared with other competitors' models with a comparable batch size.

Titanium alloys' unique features can also be exploited in advanced industrial applications, such as the design of supersonic aircrafts. Table 1.2 illustrates the current (and future) guideline for both structure and engine design of a supersonic aircraft, depending on its cruise speed. The high melting point of titanium (1668 °C) ensures that the heat due to friction would not have any backward effects on aircraft skeleton. Moreover, the very low thermal expansion (8.6 μm m^{-1} K^{-1}) at 25 °C for titanium ensures the thermal stability of the aircraft at supersonic speed. On the engine side, the operating temperature window in a compressor section is usually in the range of 500–600 °C, making high-specific strength corrosion-resistant titanium alloys an optimum choice for this kind of application [4].

Table 1.2 Materials selection guide for designing current and future supersonic aircrafts (Source: [4]).

Aircraft part	Current supersonic with cruise speed up to 2.0 Mach Possible material(s) to be selected	Current supersonic with cruise speed: 2.0–4.0 Mach Possible material(s) to be selected	Future hypersonic with cruise speed above 4.0 Mach Possible material(s) to be selected
Structure	Fuselage: Al: 2090-T651; 7075-T6; 8090-T651 (nose)	Fuselage: CFRP: PMR-15, PMR-11-55, or similar high-modulus composites; or new type 2-mm Al–Zn–Mg–Sc–Zr alloy	Fuselage: polyimides, BMIs, CEs, graphite fiber–phthalonitrile, or FGM (ceramic–metal composite)
	Skeleton: Ti–6Al–4V or other Ti Wings: commercial grade CFRP	Skeleton: high perf. Ti alloy Wings: CFRP: PMR-15, PMR-11-55, or similar composites; or Ti alloy	Skeleton: titanium aluminides, or high perf. Ti Alloy wings: mesh-protected CFRP, polyimides, BMIs, CEs, or stainless steel, or Ti alloy
Engine	Compressor: Ti alloy Combustor & Turbine TBC coated superalloys: SC alloys, DS blades; P/M IN-792 disc, and others	Compressor: Ti–6Al–2Sn–4Zr–6Mo or similar Ti alloy Combustor & turbine TBC coated Ni-base superalloys: SC alloys (TMS-75, Rene'N6, CMSX-lfl), MA superalloys; DS blades; P/M IN-792 disc, or advanced alloys	Compressor: advanced Ti alloy Combustor & Turbine TEBC coated superalloys: Mo-based superalloys; or aluminum-added ceramic composite; or other advanced material

Recognized as the lightest structural metal, magnesium and its alloys have always drawn the attention of those industrial sectors at the perpetual pursuit of structural weight reduction, fuel energy savings and CO_2 emissions limitation [5]. The high specific strength of Mg encouraged its use in racing cars. Dominant types of cast magnesium alloys in the automotive industry include the Mg-Al-based alloy series, such as the AZ and AM alloys [6]. Volkswagen was the first company to adopt Mg in powertrain units of its Beetle model in 1930s. In 1968 Porsche also developed a casting technique using Mg for the engine blocks.

In addition to lightweight, magnesium alloys show a range of interesting properties such as excellent castability, machinability, damping capacity, heat dissipation and electro-magnetic shielding characteristics. These qualities make Mg alloys suitable for several automotive parts manufacturing, such as seat frames, wheels, housings, transmissions cases, engine blocks, steering wheels column in automobiles (Figure 1.5).
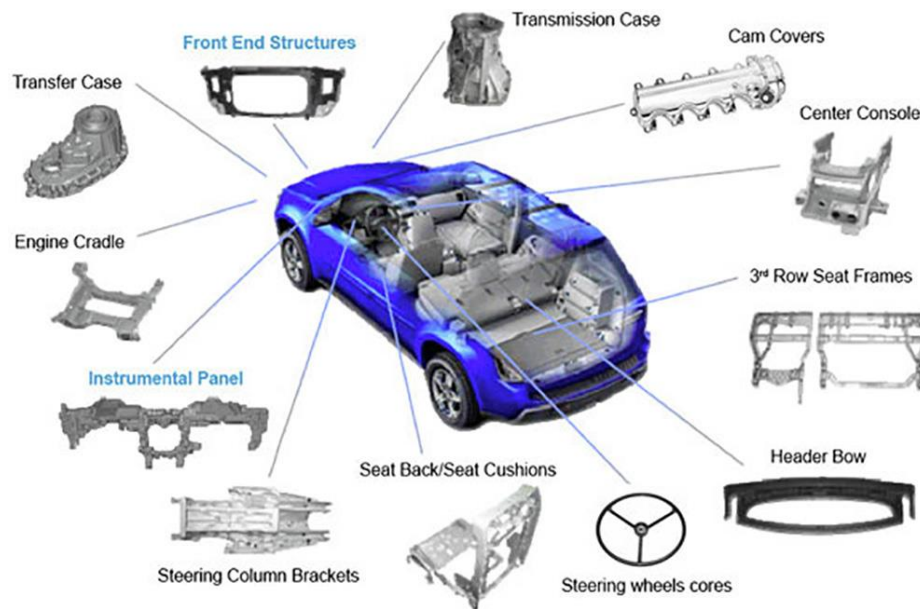
Figure 1.5 *Magnesium-based components in automobiles (Source: [5]).*

Magnesium alloy AZ31 is frequently adopted in aircraft applications due to its low density and good mechanical properties. B-36 Bomber aircraft (containing 19,000 lbs of magnesium) and Titan I rocket (1100 lbs in magnesium sheet) can be cited as remarkable Mg alloys applications in the past. Nowadays, the most relevant Mg applications in aircrafts include the thrust reverser (for Boeing 737, 747, 757, 767 models), gearbox (Rolls-Royce), engines, and helicopter transmission casings. On the military aircraft side, the Eurofighter Typhoon, Tornado, and F16, also take advantage from the lightweight characteristics of magnesium alloys, which are adopted for transmission casings.

In addition to automotive and aerospace industries, different lightweight materials are currently adopted in several biomedical applications, depending on the specific task to be accomplished. Originally employed in dentistry implants (starting from 1950s), Ti-alloys were gradually used for bone implants because of their congenial features. Indeed, titanium is meant as a non-toxic material to the human body, even at high quantities. Moreover, titanium fatigue performances turn out to be unaltered in corroding media. The in vitro and

in vivo tests showed that Ti element is both safe for human body and exhibits high osseointegration (*i.e.* the formation of a direct interface with bones without intervening soft tissues) [7]. These properties make titanium and its alloys highly suitable for biomedical applications, but some limitations including stress shielding (leading to bone re-fracture) may compromise the bio-effectiveness of those devices made by 'inert' metals (titanium alloys, stainless steel, cobalt-chromium alloys). Furthermore, in order to avoid potential hostile effects after fracture healing, a second surgery operation is often required to remove the temporary implant. In this perspective, one of the main advantages of magnesium (Mg) alloys-based implants over standard permanent metal implants is their biodegradability [8]. Magnesium-based implants can gradually degrade via corrosion within human body. On functional side, magnesium mechanical strength, which is close to cortical bone one, may address concerns on re-fracture or unsatisfactory healing outcome to the fracture site by reducing stress shielding.

All the above-mentioned applications describe the lightweight alloys potential as multi-purpose materials, able to fulfil different needs depending on the application field. Although their remarkable qualities, these materials show poor formability in conventional sheet metal forming processes at standard conditions. Aluminium alloys have a lower formability than mild steel, typically adopted in industrial applications. As a proof of that, aluminium exhibits a lower LDW (*limiting drawing ratio*) value than steel for deep drawing operations. Elongation at break of Magnesium barely reaches 10% at room temperature, negatively affecting the amount of imposed plastic deformation on sheet metal, then the final object complexity. Similarly, titanium alloys show poor formability if compared with mild steel at same conditions. Therefore, the current challenge in automotive, aerospace and R&D sectors consists in manufacturing lightweight structures with these materials, overcoming their formability limits by using innovative strategies and processes in sheet metal forming contest.

1.2. Unconventional sheet metal manufacturing processes

All over the last decades, the documented tendencies in sheet metal forming area have been mainly pertained to the development of non-conventional forming methods for difficult-to-form lightweight materials, especially for automotive and aircraft applications. The current market targets, characterized by small-batch production and a never-ending product innovation voted to satisfy specific customer's requirements, led to the development of modern machines (together with the design of suitable structures) to increase their specific performances in terms of production flexibility and production costs [9].

It is possible to identify two main advancing directions concerning sheet metal forming:

- On one hand, the design of innovative moulding processes, namely *Flexible-Die Forming*, based on flexible materials adoption (such as elastomers, liquids or gas) in place of one of the dies to reduce costs. Rubber-Die forming and Hydroforming processes belong to this specific category.

- On the other hand, *Incremental Sheet Forming* processes (ISF), in which the final component shape does not depend on die geometry anymore, but is determined by the assigned path to a small forming object, have been developed. By editing the toolpath, it is possible to obtain more and more complex geometries, then achieving the desired goal of process flexibility.

In the next paragraphs, some of the most important unconventional sheet metal processes are described, with a particular focus on the non-axisymmetric incremental forming.

1.2.1 Flexible-Die forming

The sheet metal manufacturing techniques belonging to this process family are characterized by the implementation of a pressure–transfer medium as a female die (or punch) or a female punch (or die) [10]. The adopted medium can be polyurethane, oil, viscous medium, rubber or compressed air. Flexible-die forming technology has been covering an important role as one of the most adopted forming technologies for thin-walled components. Together with *Viscous Pressure forming* (VPF) and *Hydroforming by Deep Drawing* (HDD), these technologies are being developed quickly, thanks to both experimental case studies and numerical analysis tools [11], [12].

Rubber-Pad Forming (RPF) process presents a rubber pad on the form block. The rubber pad acts as a hydraulic fluid, which applies a uniformly distributed pressure on workpiece surface as it is pressed within the form block. Due to some interesting advantages like reduced spring-back phenomenon and the absence of surface scratches on the blank during forming operation (thus a higher surface quality of the final part), RPF is widely used in many real-life industrial applications [9], [13]. Flexible forming processes, including stamping, deep drawing or bending, are widely used in the aircraft industry to deform difficult-to-form materials by a conventional deep drawing process. In this regard, *Irthiea et al*. [14] reported the results of FE simulation and experimental study on micro deep drawing processes of 304 stainless steel sheets using a flexible die. Two novel approaches were considered with regard to a positive and a negative initial gap between the adjustment ring, the workpiece and the blank holder (Figure 1.6). The experimental results, as well as the numerical model output, revealed the capability of the proposed technique to produce micro metallic cups with high quality and a large aspect ratio.
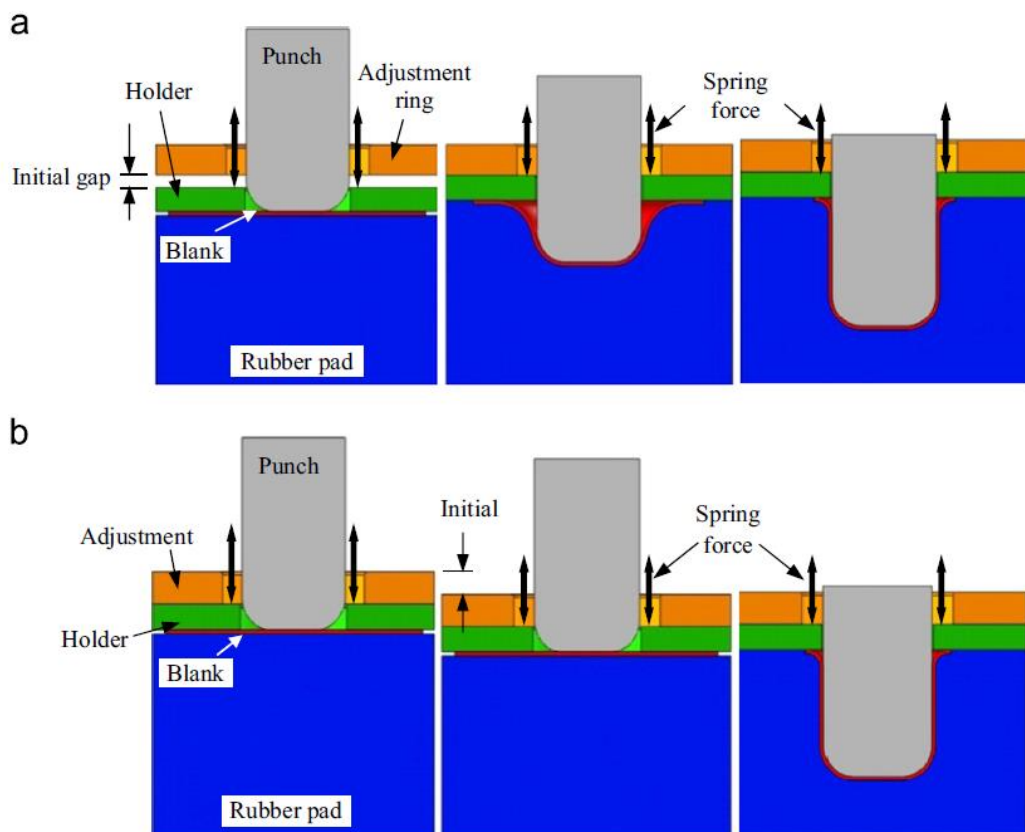

Figure 1.6 *Rubber-Pad Forming technology with (a) positive and (b) negative initial gap (Source: [14]).*

The *Multipoint Forming* process (MPF) employs a reconfigurable matrix of pins, which can move along the normal direction to the die base and, depending on every single adjustable pin position, create different die surfaces. In addition, a reconfigurable tool consisting in a large number of adjustable pins, can be paired with the adjustable die in order to change the final shape of manufactured part [15]. Over the years, several designs of reconfigurable tools have been developed with the aim to manufacture different geometries [16]. The MPF process is very flexible, allowing quick changes in tool configuration and minimizing the cost item attributed to the adoption of a new one [17]. In the perspective of tool costs reduction compared with conventional reconfigurable MPF tools, the *Multipoint Sandwich Forming* (MPSF) was developed. Pins are adopted in the bottom die only with a wider disposition (Figure 1.7); in this way, a fewer of them are required to span a given area, while their height is adjusted manually using their threaded shanks. The upper die is made of urethane. To provide a continuous surface for the bottom die, a steel sheet is deformed between the appropriately positioned pins and the urethane upper die [15].
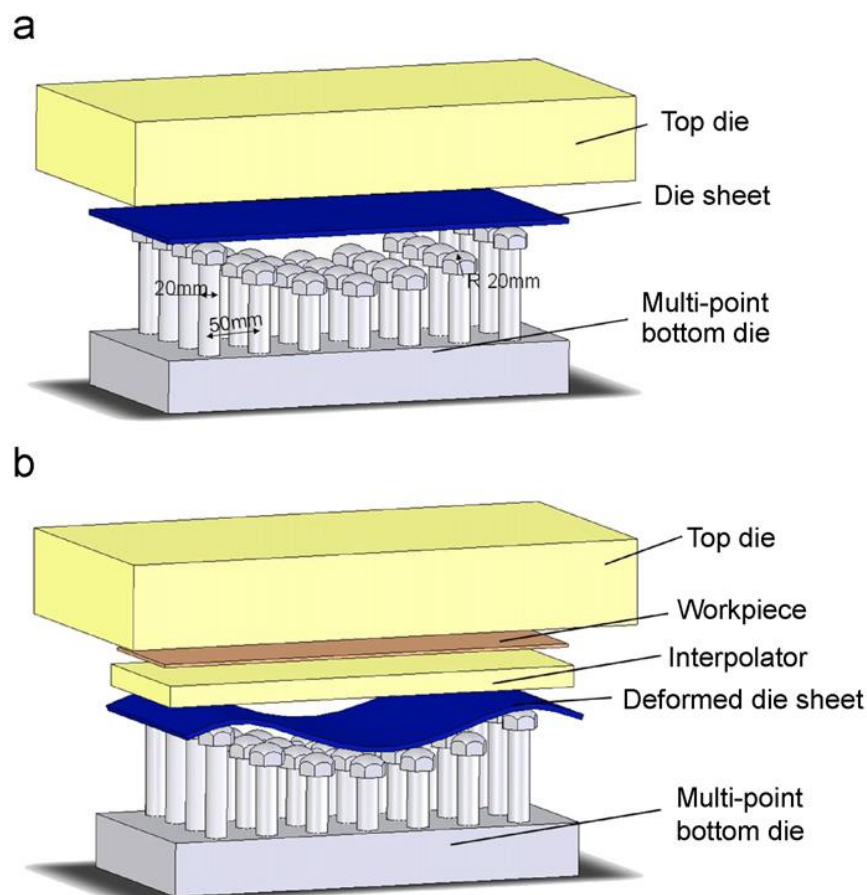
Figure 1.7 MPSF process setup. (a) setup for die sheet deformation and (b) set up for workpiece deformation (Source:[15]).

Hydroforming is a near-net shape metal forming process allowing to manufacture complicated shapes by means of fluid pressure instead of (or together with) traditional mechanical forces. Some peculiar features, such as the ability to create re-entrant features, reduced thinning, together with enhanced mechanical properties, make this process attractive in a wide range of industrial applications [18]. These advantages are mainly a direct consequence of both the working fluid ability to exert a uniform pressure all over the material surface, and the fluid pressure regulation during the forming cycle based upon an optimized load path. The *Sheet Hydroforming Process* (SHF) is typically performed using either a cavity die or a punch; the punch hydroforming variant is commonly known as hydromechanical deep drawing [19]. The processing principle of both SHF variants are represented in Figure 1.8. The process choice depends on the geometrical complexity as well as the draw depth of the part to be formed. If a part has a complicated surface (e.g., with many different bulges), a cavity die represents the best option. If the part has a cylindrical geometry and a simple (flat or curved) surface, a solid punch will be beneficial as it can perform a deeper draw [20].
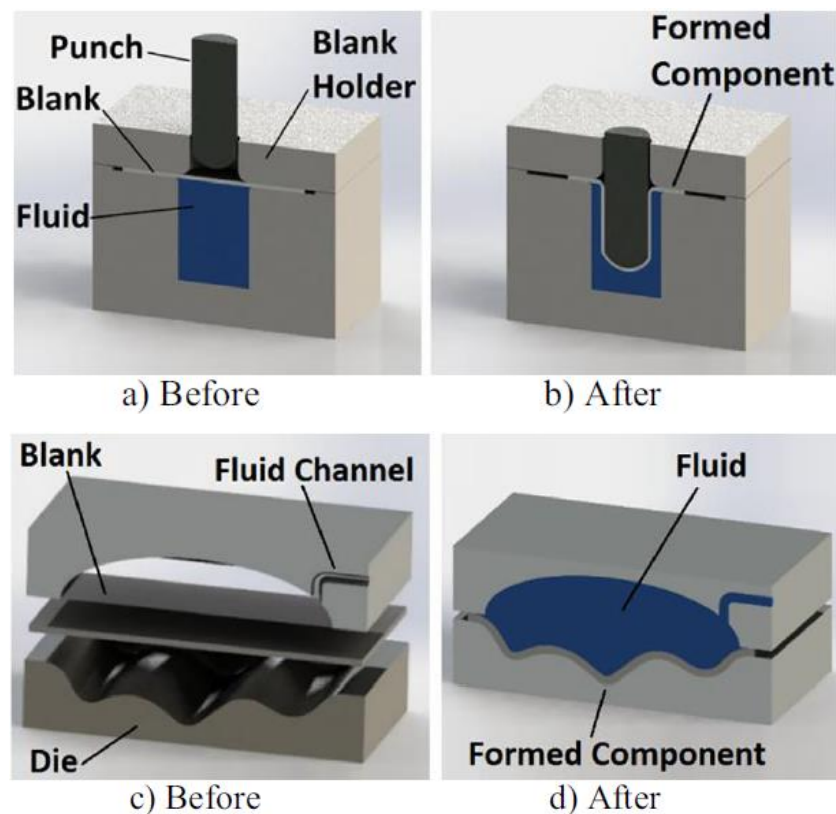

Figure 1.8 Schematic illustration of punch (a, b) and cavity (c, d) hydroforming (Source: [18]).

1.2.2. Incremental Sheet Forming

This process category shares a common approach of material localised deformation under the tool, thus lower forming forces are required to obtain the desired geometry. Moreover, a simple and non-dedicated tool provides high process flexibility, together with a net-shape forming potential. Compared to conventional sheet metal processes, the formed components obtained by ISF show high quality surface finish and improved mechanical strength [21]. The most adopted sheet metal incremental forming processes for industrial applications are *Spinning*, *Shear Spinning and Non-Axisymmetric Incremental Forming*.
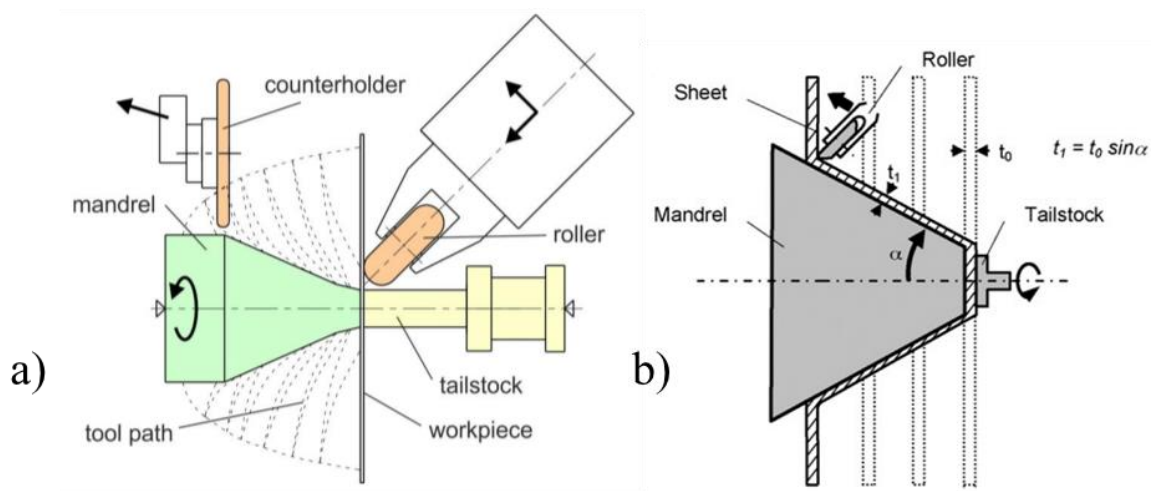
Figure 1.9 *a) Spinning process setup (Source: [9]) and b) Shear Spinning process setup (Source: [21]).*

Spinning is the shaping of a rotating disc or draw piece by applying local pressure using a spinning tool (Figure 1.9a). A forming tool, in the form of a mandrel or a roller, can roll or slide over the sheet surface. A typical feature of the spinning process is that the starting blank thickness changes within only a very small range. The deformed disc or blank gradually assumes the shape of the spinning block, which is usually made of metal. In case of spinning components with complex shapes, partial or uniform spinning blocks can be used. The spinning tool and workpiece perform a rotational motion. Spinning ability is measured by the limiting spinning ratio, which is the ratio of the maximum original blank diameter that can be successfully spun forming a cup, in a single pass, to the mandrel diameter [22], [23].

Differently from conventional spinning, in *Shear Spinning* the sheet thickness is intentionally reduced while the part diameter keeps constant, equal to the blank diameter. As the roller traces the shape of the mandrel at a fixed distance, a blank of initial thickness t_0 is

reduced to a thickness t_1, where the final thickness t_1 is related to the wall angle α by the well-known sine law (Figure 1.9b). The work hardening phenomenon improves the mechanical properties of spun components. Hence, this often eliminates the requirement for any additional heat treatment to be carried out on finished parts [24], [25]. Shear spinning is widely used to manufacture components in the aerospace, aviation and automotive industries [21], [26]. Hard-to-deform materials at room temperature, such as titanium alloys [27], nickel-based alloys [28], [29] and stainless steel [30], are commonly processed by using the shear spinning process.

Based on the same Shear spinning logic, a new type of incremental forming technology, namely *Asymmetric Incremental Forming* (ASIF), was proposed in the early '90. This kind of processes are merely a consequence of the introduction of CNC mills and CAD software with toolpath postprocessors into the industrial production chain. The idea was first introduced in a patent in 1967 [31], even though an adequate process automation was not available at that time. The term 'die-less', as applied to this process, was used in that patent for the first time.
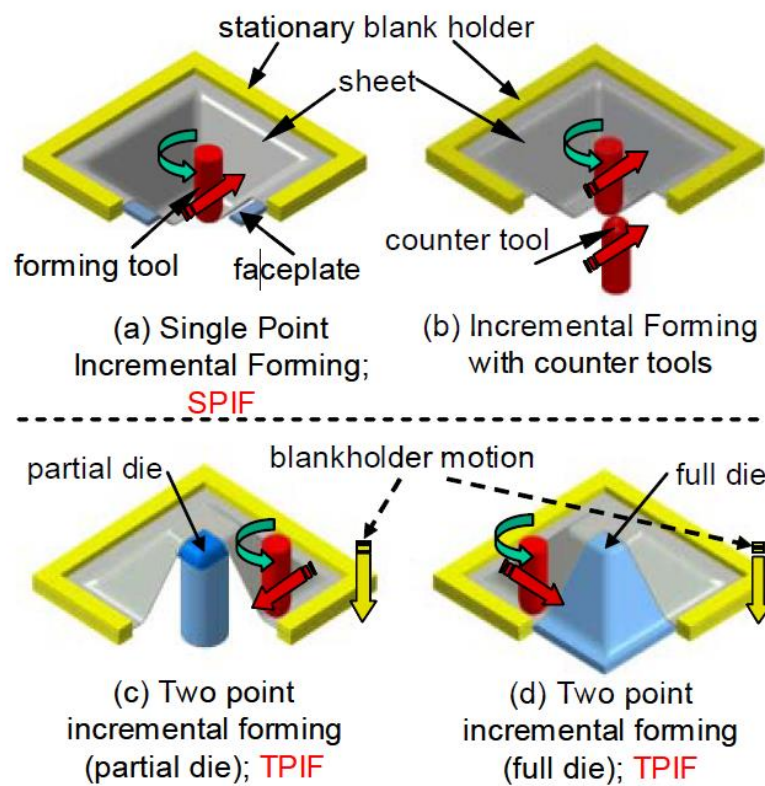

Figure 1.10 Asymmetric Single Point Incremental Forming variants (Source:[34]).

Asymmetric Incremental Forming can be performed using either a machine specifically designed for the process or a three-axis CNC mill, which is widely diffused over the world. Although machines have been designed specifically for this process, AISF of sheet can be carried out by anyone having access to a three-axis CNC mill and off-the-shelf software, which generates machine toolpaths. Figure 1.10 shows the different configurations that are included in the group of asymmetric incremental sheet forming (ASIF) techniques. It can be observed that three of the processes meet the above criteria. The fourth, Figure 1.10, uses a full die and does not meet the "die-less" criteria. However, it is related directly to the other processes and it is being used successfully to make rapid prototype shapes. Hence it is included in the list of die-less forming techniques.

The adoption of conventional forming techniques for sheet metal processing is more time-consuming and costly for those processes which are recently applied in small-batch production. Consequently, there is a need to disseminate an alternative process to reduce the manufacturing costs related to individual parts production, such as medical implants. Processes which show benefits in this respect are methods of incremental sheet forming which do not require the manufacture of dies for operation and have the ability to shape elements on a conventional CNC milling machine [9].

In this perspective, *Single Point Incremental Forming* (SPIF) shows interesting features in terms of flexibility, setup costs and availability, part customization, rapid prototyping. In the next chapter, the state-of-art of SPIF will be debated, taking a look on process potentials in lightweight sheet metal alloys manufacturing and its future developments.

2. Single Point Incremental Forming: the state of art

2.1. *Historical background and process description*

The *Single Point Incremental Forming* (SPIF) in its most basic form is characterised by continuously superimposing local deformations in a sheet until a final shape is reached. These deformations are applied on the workpiece by small tool, moving along a predefined path and describing the desired geometry or any corrected tool path finally yielding to the target shape [32]. This process provides an higher degree of flexibility than other forming processes as it does not require a dedicated die to form the final geometry. This aspect results in reduced lead-time and equipment costs. As a result, SPIF is a relatively fast and cheap solution for small-batch production of sheet metal parts. On the other hand, the process itself is quite slow if compared to traditional forming processes, such as stamping and deep drawing, lacks the ability to form steep wall angle parts in a single pass and is faced with limited forming limits and dimensional accuracy [33]. The localised nature of the deformation zone around the tool, leads to lower forming forces than conventional sheet forming processes. This keeps the strength requirements of the positioning system that drives the tool quite low [34]–[36]. As mentioned before, the first declaration of an apparatus and process for incremental forming was filed as a patent by *Leszak* in 1967 [31]. The hardware components typically used in SPIF are depicted in Figure 2.1.
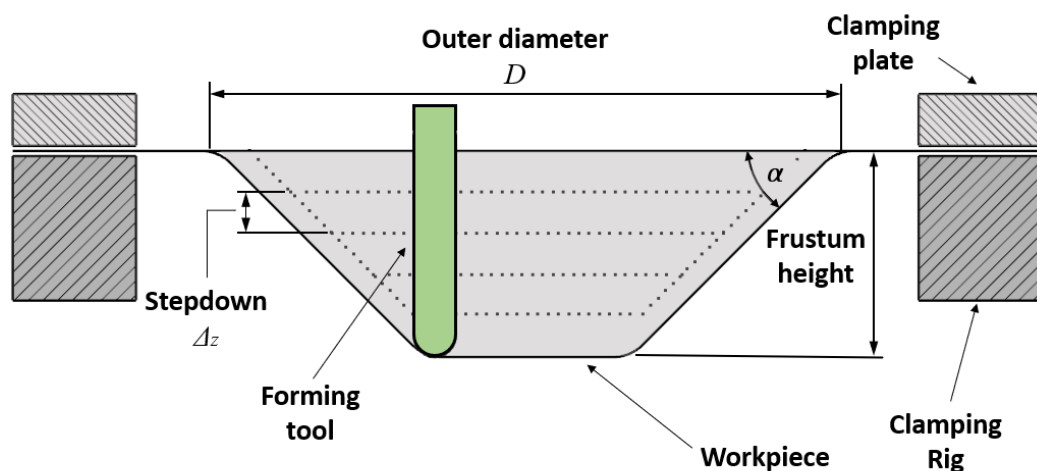
Figure 2.1 Schematic overview of the hardware components for conventional SPIF.

SPIF process deforms the sheet through a relative movement between tool and sheet, allowing Incremental Forming to be performed on most multi-axes positioning systems. The three orthogonal axes used for most SPIF machines can be employed for a wide variety of parts manufacturing. The *Asymmetric Single Point Incremental Forming* (SPIF) research performed by *Jeswiet et al.* [37] and *Filice et al.* [38] in the early '00 showed that the SPIF forming method can be performed on a standard three-axis CNC mill. This includes the application of CAD/CAM software to plan the process toolpath, making possible an easier fabrication of complex parts. Working parts can be prepared directly from CAD data with a minimum of dedicated tooling. These can be either Rapid Prototypes or small volume production runs. For pragmatic reasons many research institutes have chosen to adapt conventional milling machines as a SPIF experimental platform, proving the viability of these alterations and ease of adoption by industry and workshops. Although stiff, these machines are most often not optimised for high dynamic behaviour and high axial forces. Articulated robots are the second most popular used equipment for their versatility and low cost (Figure 2.2a). However, low stiffness and absolute accuracy are a great drawback of these platforms.

Figure 2.2 *Different hardware setups for single point incremental forming process (Source: [33]).*

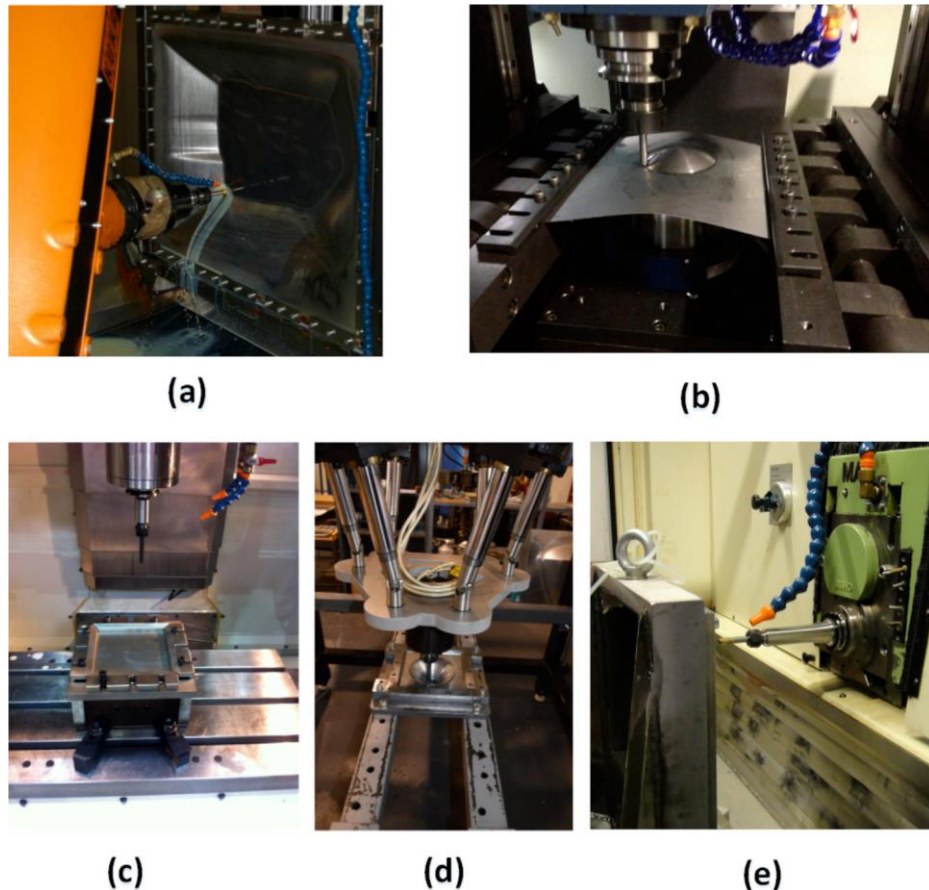Generally speaking, SPIF shows lower force values compared to conventional processes due to the small deformation zone. *Aerens et al*. [39] carried out an experimental study with the aim to create a factorial model for force prediction. The authors found out that material, tool size, incremental step size between contours (Δz) and wall angle (α) of the part are the main influencing parameters. *Marabuto et al.* [40] provided an overview of forming forces obtained by different research institutes on a variety of materials and thicknesses, and concluded that 13kN along the main tool axis and 6.5kN as in-plane force component are sufficient for most industrially relevant parts.

As the SPIF tool performs a contouring operation, tool paths rapidly grow with increased part sizes and make the process time consuming. To further extend SPIF application to wider size batches production, *Ambrogio et al.* [41] and *Vanhove et al.* [42] experimented with a high speed variant of SPIF for axisymmetric part manufacturing, proving that no negative effect were detected by increasing the strain rate in SPIF. Moreover, for some materials, such as aluminium 5xxx series, an increase in formability was observed at high strain rates values. In the abovementioned studies, tool federate values were increased from the conventional 2 m/min up to extremes of 600 m/min. This seems to justify the need for highly dynamic machines in the optics of larger batch sizes production.

The small contact area between tool and sheet results in high contact pressure and considerable surface friction. By using lubrication and a net rolling of the tool over the sheet, surface deterioration and reduced formability through friction rather than dragging can be counteracted. *Jeswiet et al*. [34] provided an overview considering the optimal axial rotational speed of a driven tool compared to the wall angle of the part, while a spindle free-rotating tool will rotate at optimal speed automatically. From *Lu et al.* [43] observations, it was concluded that an increased surface quality and formability can be obtained using an oblique roller-ball tool, allowing the tool tip to rotate in all directions (Figure 2.3c). Lubrication further reduces the friction between the tool and the sheet. A wide variety of oils, greases and waxes are being used in SPIF. *Azevedo et al.* [44] concluded that, as the hardness of the sheet material increases, the required viscosity of the lubrication decreases. Besides the surface and formability effects on the final part, the significant friction in SPIF plays a key role in tool wear, then in choice of the tool material. Naturally the tool needs to be hard, leading to the adoption of specific materials, such as tool steel (HSS) and carbide tools [45]. To further increase hardness these tools are often (surface) hardened and/or coated with conventional coatings suited for cutting tools (TiN, CrN).
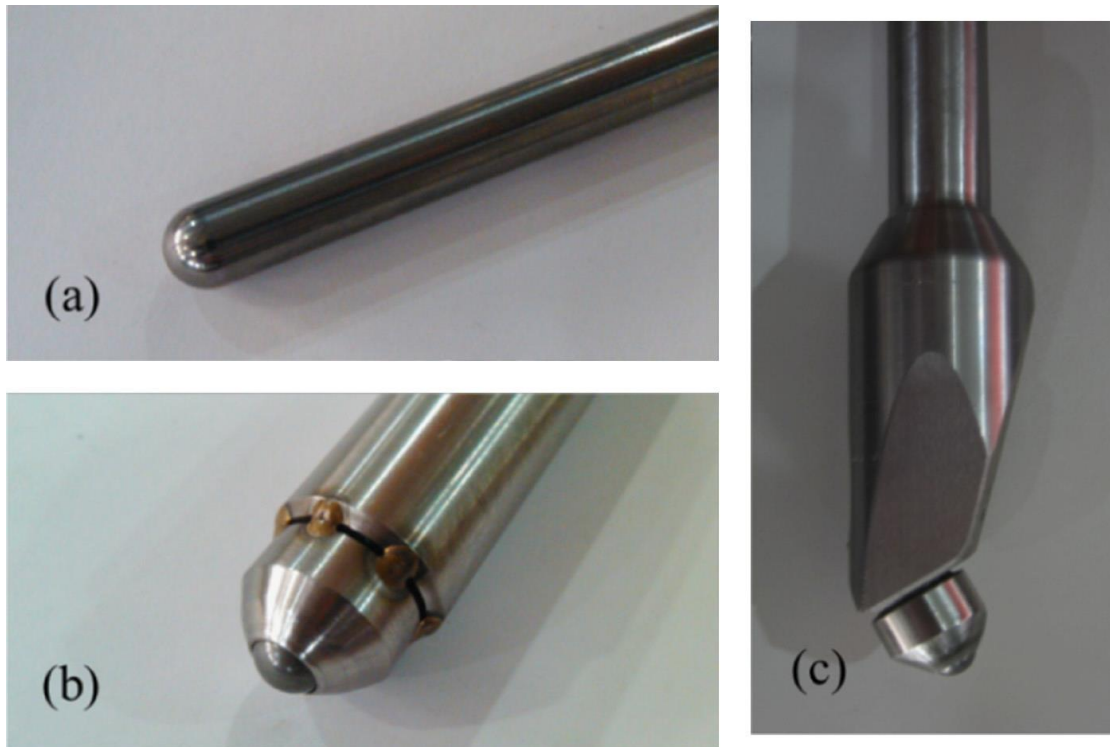
Figure 2.3 *Different SPIF tool types. a) classic rigid tool, b) tool with vertical roller-ball (VRB) and c) tool with oblique roller-ball (ORB) (Source: [43]).*

In order to clamp the workpiece during SPIF operation, rigid blank holders are adopted (see Figure 2.1). These generic clamping systems allow to install dedicated supports or backing plates, helping to limit undesirable deformation of the blank in an early stage of the forming process. Rigid support in the immediate forming zone proximity guarantees a higher accuracy and reduces scrap material related to extended transition areas between the current part geometry and clamped workpiece edge. The sheet is typically clamped on the blank holder using bolts and clamping plates along the workpiece edges. Finite element simulations by *Bouffioux et al*. [46] demonstrated that limited sliding can significantly affect the tool force required to form an indent shape. As reference, a sliding effect of 0.08mm was found to result in a 16 % force reduction on the tool. Therefore, in order to obtain reproducible results, the applied torque on each clamping bolt has to be constant and high enough to prevent sliding.

2.2. *Main Parameters in SPIF*

Although parts can be made using a single generic tool, the tool size is an influencing factor in the SPIF process. *Aerens et al.* [39] reported that increased process forces increase as the tool size increases. Likewise, a decrease in formability has been observed while increasing the tool size [47]. Usually, the tool size is limited by different factors, such as high forces, the smallest detail to be produced and/or the machine limits. Then, the diameter of the ball-head must be chosen. A wide range of tool diameters is used, starting with small diameters of few millimetres and going up to tool diameters of 100 mm for large part manufacturing. A bigger tool diameter requires much more power because of the wider angle of contact involved. The adopted diameter depends on the smallest concave radius required in the part. It also has an influence upon the surface quality and/or the manufacturing time [34].

The material parameter, draw angle α, defined in Figure 2.1 plays a key role in SPIF process. The largest designed draw angle in the part (α_d) must be less than the material parameter (α_{max}), the maximum value of the draw angle, which is a material characteristic. A design engineer can check from the CAD drawing if α_{max} has been reached and by making judicious choices when embedding the part in the sheet surface, α_d can often be made smaller than α_{max}. Once the part has been embedded in the surface of the sheet metal the comparison between α_d and α_{max} will show if the part can be made in one pass, two passes or several passes, after which toolpaths can be generated. *Jeswiet et al.* [34], on the basis of multiple research studies, established in their 2005 CIRP keynote paper the guidelines regarding the effect of every single process parameters -namely the thickness of the sheet metal, the draw angle α, the incremental step down Δ_z, the tool federate and the tool size – on formability, forming forces and surface finishing of manufactured parts by SPIF. The abovementioned guideline lists as follows:

Formability side:
- Formability increases with higher sheet-to-workpiece relative velocities, with a trade-off of higher surface roughness.
- Formability decreases with thinner sheet.
- Smaller tool size gives increased formability.
- Anisotropy has an influence upon formability, with greater formability being achieved with smaller diameter tools in the transverse direction.

- Sheet formability decreases with increasing increment step size, Δ_z.

The effect of increment step size, Δ_z:
- Large increment steps, Δ_z, give a higher roughness.
- The increment step size, Δ_z, can influence not only the surface roughness but also cause an orange peel effect.
- The size of the orange peel effect can be influenced by the incremental step size, Δ_x and Δ_y, and the draw angle.

The effect of the draw angle α:
- There is a limitation on the maximum draw angle α that can be formed in one pass.
- With increasing draw angle α, the sheet thickness reaches a minimum value where fracture occurs as a consequence.
- There is a strong dependence of the deformed sheet thickness on the draw angle α, which can lead to inhomogeneous thickness distributions in the final part.
- Knowing the parameter α_{max} for a material at a specific thickness, a designer can take the first step in deciding if a sheet metal part can be made in one pass without tearing, or if a two pass or multiple pass sequence should be used.

Forces side:
- Peak forces can be observed in the area where failure occurs at maximum draw angles, α_{max},
- Increasing the vertical step size Δ_z increases forces,
- Larger tool diameters increase forming forces.
- Increasing vertical step size Δ_z has a much lower impact when compared to draw angle and tool size.

2.3. *Process Limitations*

As mentioned in Paragraph 2.1, the SPIF toolpath rapidly grows as the part size increases, making the process high time-consuming. This is one of the main process limitations, relegating it to medium/small-batch production cases. To partially solve the problem, then to further extend SPIF applications, high speed variant of SPIF for axisymmetric part manufacturing were performed by *Ambrogio et al.* [41] and *Vanhove et al.* [42], proving that no negative effect were detected by increasing the strain rate in SPIF. This also entails the adoption of highly dynamic machines which represent an additional cost of setup.

Another key issue in SPIF consists in the achievable accuracy. *Jeswiet et al*. [34] reported that, while most industrial parts require an accuracy of ±0.5 mm, it is observed that parts produced by SPIF have significantly higher dimensional inaccuracies. Indeed, the geometrical accuracy in SPIF is limited by the absence of a die supporting the workpiece while formed by the SPIF tool. The obtained accuracy in SPIF processes also depends on the stiffness of the adopted setup. In this perspective, milling machines are stiffer than industrial robots: therefore, manufactured parts by using milling machines are inclined to be more accurate. Lots of strategies aiming to improve the attainable geometrical accuracy in SPIF were described by *Micari et al.* [48] and *Essa et al.* [49], such as the adoption of flexible support, counter pressure, multipoint and back drawing incremental forming and the use of optimized toolpath trajectories. Concerning toolpath optimization for the improvement of geometry accuracy, *Duflou et al.* [50] have demonstrated the improvement of accuracy in laser-assisted SPIF using compensated toolpaths. Another approach was proposed by *Mohammadi et al.* [51], performing an in-process laser-assisted hardening to create regions in a sheet metal part with high stiffness thereby reducing the effect of interactions among different part features, then improving the final component accuracy.

Additional noteworthy issue is related to secondary operations on the sheet metal component once processed. Indeed, trimming operations are often required at the top contour for many industrial applications. Such an operation can lead to significant distortion in the final part due to compressive stresses generated during SPIF process. This undesired drawback can be mitigated by using stress-relieving heat treatment to the formed sheet metal component [52].

2.4. Forming limitations and failure mechanism

Jeswiet et al. [34] observed that the forming limits in SPIF process can be characterized by the *maximum wall angle* (α_{max}) before failure occurs. The authors concluded that the maximum angle is dependent on the material type, sheet thickness and process parameters such as tool radius, stepdown, feedrate, local temperature of the sheet, etc. Two types of parts are commonly used to determine this specific angle: (i) constant wall angle parts (typical of truncated cone shapes) or (ii) variable wall angle parts (such as a hyperboloid cup). *Behera et al.* [33] provided a list of several wall angles for different materials, which is shown in Table 2.1. However, for parts with a varying wall angle, the wall angle at failure depends on the geometric shape being formed, with a value that can exceed the estimated one for constant wall angle parts by ~4°, as published by *Hussain et al.* [53].

Table 2.1 *Maximum achievable wall angle for different materials (Source: [33]).*

Material	Formed specimen geometry	Tool diameter (mm)	Thickness (mm)	Max. achievable wall angle
65Cr2	Truncated cone	10	0.5	57°
AA 1050-O	Truncated cone	10	1.5	76°
AA 2024-T3	Truncated cone	10	1.0	42°
AA 3003-O	Truncated cone	10	0.85	70°
AA 3003-O	Truncated cone	10	1.2	71°
AA 3003-O	Truncated cone	10	2	76°
AA 3103	Truncated cone	10	1.5	75°
AA 5086-H111	Truncated cone	10	0.8	62°
AA 5182	Truncated cone	10	1.25	64°
AA 5182	Truncated cone	25.4	0.93	63°
AA 5754 (AlMg3)	Truncated cone	10	1	64°
AA 5754 (AlMg3)	Truncated cone	10	1.5	71°
AA 6111-T4P	Truncated cone	25.4	0.93	53°
AA 6114-T4	Truncated cone	12	1.0	60°
AISI 304	Truncated cone	10	0.4	63°
Brass	Truncated cone	12	1	40°
Copper	Truncated cone	12	1	65°
DC01	Truncated cone	10	1	67°
DC04	Truncated cone	10	1	64°
DDQ	Truncated cone	12	1	70°
DP600	Varying wall angle conical frustum	16	1	68°
DP780	Varying wall angle conical frustum	16	1	45°
DP1000	Varying wall angle conical frustum	16	1	39°
HSS	Truncated cone	12	1	65°
Ti grade 2	Truncated cone	10	0.5	47°
TiAl6V4	Truncated cone	10	0.6	32°
Polyamide	Varying wall angle conical frustum	10, 15	2, 3	75.4° [a]
Polyvinyl chloride	Varying wall angle conical frustum	10, 15	2, 3	75.4° [a]
Polyethylene	Varying wall angle conical frustum	10, 15	2, 3	81° [b]

[a] This is an average over tests with varying tool diameter, sheet thickness and initial drawing angle.
[b] This is a peak over tests with varying tool diameter, sheet thickness and initial drawing angle.

Due to its peculiar local and incremental deformation approach, SPIF process significantly enhances the achievable stretch and formability in sheet metal relative to conventional stamping operations as defined by the *Forming Limit Curve* (FLC) [34], [38].

All over the years, formability/fracture curves for SPIF were being developed and verified, and then often compared to a traditional FLC gathered from stamping processes, despite the significant increase in strain values [54]. Such a fact is displayed in Figure 2.4, showing a Fracture forming limit diagram containing the conventional forming limit curve (FLC), the fracture limit line (FFL) and the fracture points obtained from conical and pyramidal SPIF operations on AA1050-H111 sheet blanks with 1-1.5-2mm thickness values.

The overall consensus was that the formability limits in SPIF were much higher than those found in conventional stamping due to the localization of plastic deformation [32]. *Eyckens* [55] explains why conventional forming limits diagrams fail for SPIF. The reasons ascribed are that conventional FLCs are valid only under the assumptions of linear strain path, negligible through thickness shear, plane stress and deformation caused primarily by membrane forces with no bending. These conditions are not met in conventional incremental forming.
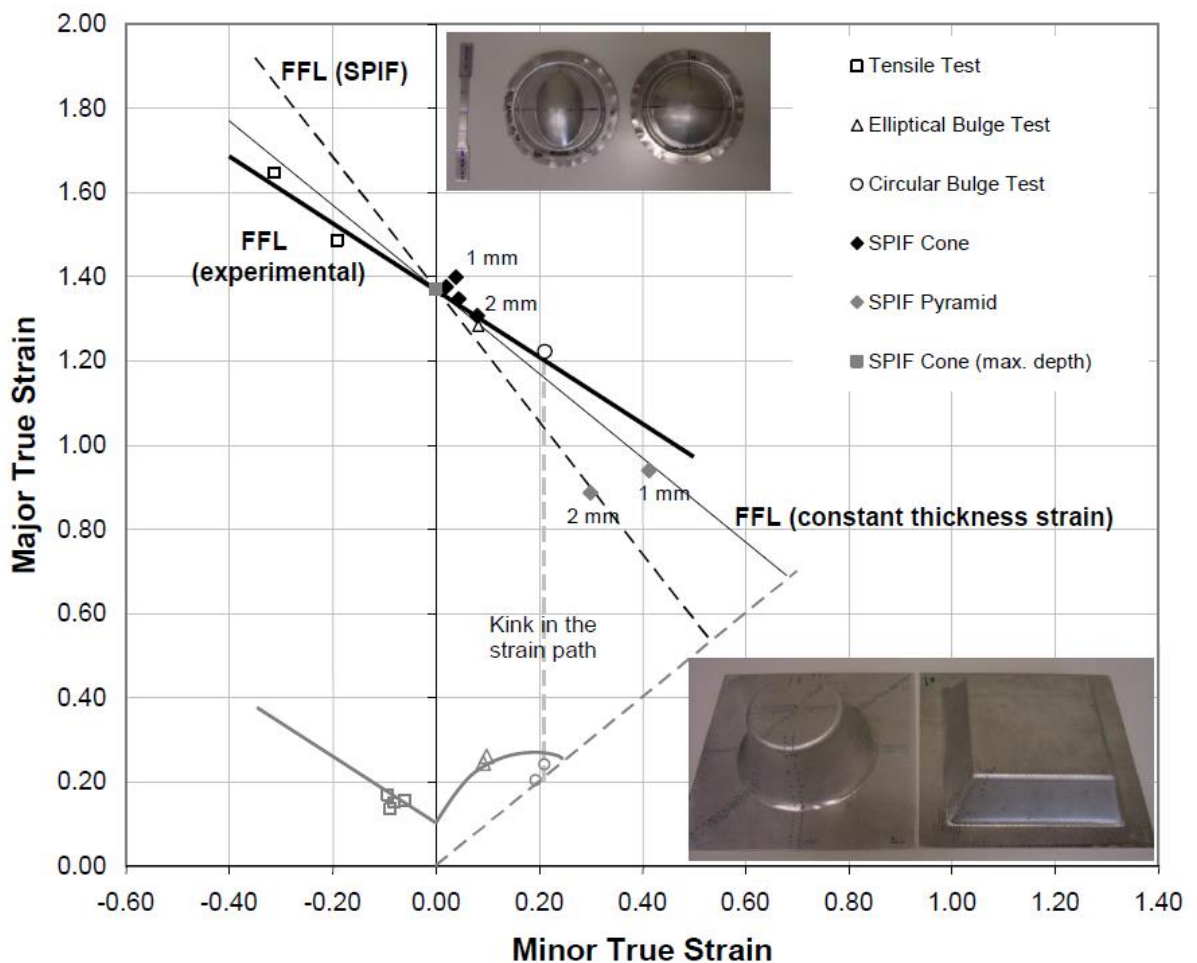

Figure 2.4 Fracture Forming Limit diagram, comparison with conventional FLD curve (Source: [54]).

However, later studies attempted to further explain the specific material failure mechanisms present in incremental sheet forming, leading to a variety of theories within the field. One school of thought is that formability in SPIF is limited by necking and that a stabilizing effect exists caused by either significant through-the-thickness shear or by serrated strain paths arising from cyclic, local plastic deformation [56]–[58]. On the other hand, there has been experimental evidence to support the avoidance of necking prior to failure. This thought was furtherly justified by noting that the forming limits in SPIF can be approximated in the principal strain domain thanks to straight lines with negative slopes of $\varepsilon_1 + \varepsilon_2 = q$ placed near the fracture forming limit [34], [54], [58], [59].
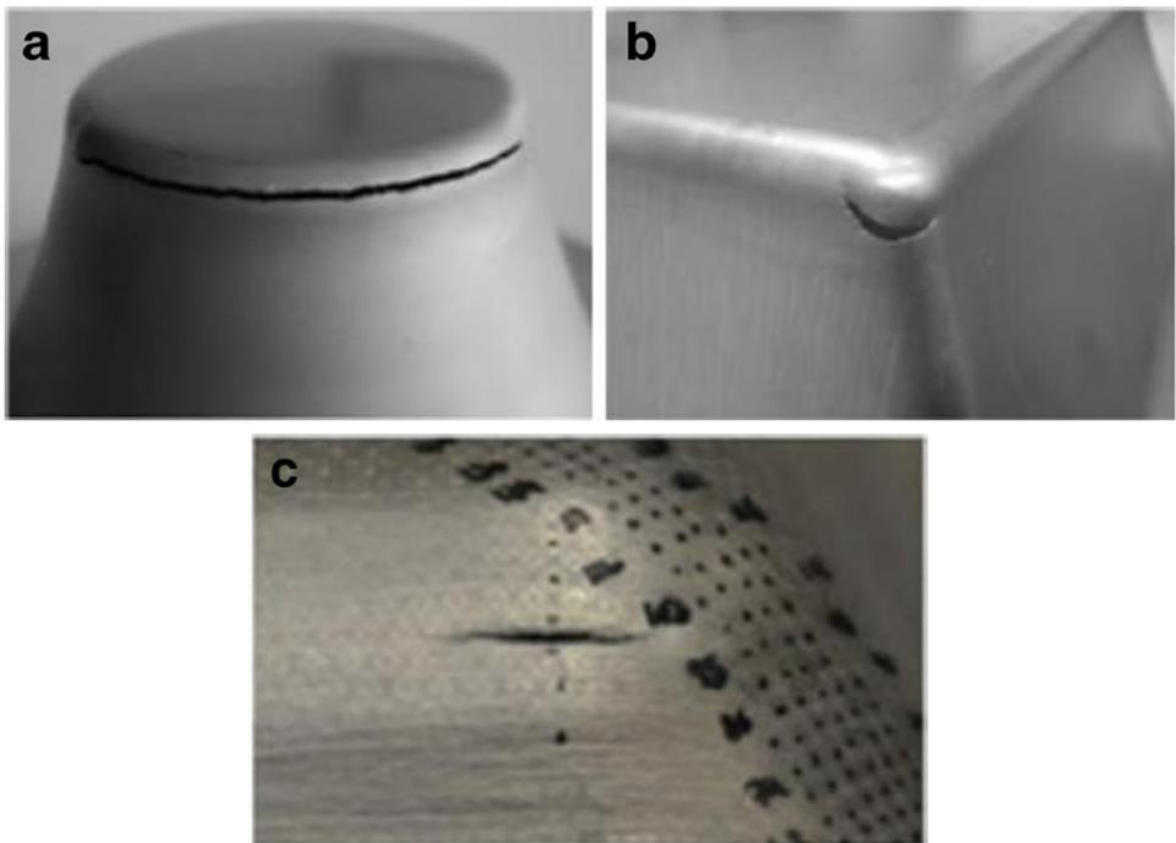
Figure 2.5 *Some failure modes in SPIF process. a) Circumferential crack in plane strain, rotationally symmetric conditions which can also propagate in a zig-zag fashion; b) Crack in biaxial stretching, rotationally symmetric conditions; c) Crack initiation after necking under biaxial stretching, rotationally symmetric conditions due to the use of a large tool (i.e., tool diameter > 20 mm) (Source:[32]).*

Considering common geometries, the most of parts shows failures along the bottom perimeter with some variation of a propagated crack in the circumferential direction. The specific modes of deformation and predicted failure are highly dependent on both the material parameters and tool configuration. Various measures and indicators of formability

have been considered in SPIF; however, most failure limits are approximated in principal strain space by a straight line with a negative slope.

To sum up, the proposed reasons for the enhanced formability in SPIF processes typically fall into one of the two following categories: (1) failure is limited by necking, which is prolonged by various stabilizing effects such as in-plane shear or hydrostatic pressure; or (2) that excessive thinning directly leads to fracture without prior localized necking. While both cases have been analytically predicted and experimentally observed, there is a strong case for failure without necking when one considers the typical experimental parameters found in SPIF. To be specific, most applications of SPIF utilize a relatively small tool due to the increased formability and precision that can be achieved, which results in the promotion of fracture rather than stabilization effects that ensure localized necking [32].

2.5. *Process window enhancement strategies*

With the aim to overcome the formability limitations affecting conventional SPIF process, new Single Point Incremental Forming variants have been proposed over the years. Indeed, the limits of traditional process can be extended, leading to part failure for higher wall angle values (α_{max}). A range of techniques have been explored, covering material formability improvement through heat supported variants of the SPIF process, the use of electric current, and toolpath strategies (which will be discussed in next chapter) that avoid excessive strains.

Warm incremental forming processes are suited for forming operations involving materials with poor overall ductility at room temperature. Among the tested materials, lightweight Mg and Ti alloys are the most adopted in aerospace, biomedical and automotive applications due to their higher strength to weight ratio. By increasing the forming temperature more slip planes are activated, leading to better ductility properties for these alloys [32]. AZ31, Ti grade 2 and Ti grade 5 are among the most widely used materials in warm incremental forming applications. In addition to Mg and Ti alloys, high strength Al alloys [60] or low carbon steels [61] have been processed by using heat assisted SPIF processes. Furthermore, the adoption of high temperatures also results in reduced springback and forming forces thanks to material softening. These effects have also been reported for heat supported SPIF [45] and can help to overcome the forming limitations in single point incremental forming, at least to some extent.

Within the warm incremental forming technology, two types of heating strategies can be mentioned: localized and global heating. While localized heating takes the advantage of limiting unwanted deformation outside the tool-sheet contact zone, the larger number of variables to be considered to determine optimum process parameters makes this option more complicated than global heating case.

Regarding the ***localized heating*** side, *Kim et al.* [62] studied the local heating of magnesium during SPIF process by moving lots of halogen lamps on 0.8 mm thick AZ31 sheets. The process setup is provided in Figure 2.6. Results revealed that increasing the temperature up to 250 °C leads to slight improvements in material formability. However, due to the design of the halogen heating source, a large part of the heated area is positioned outside the tool-sheet contact zone and the heating cannot be considered to be carefully localized.
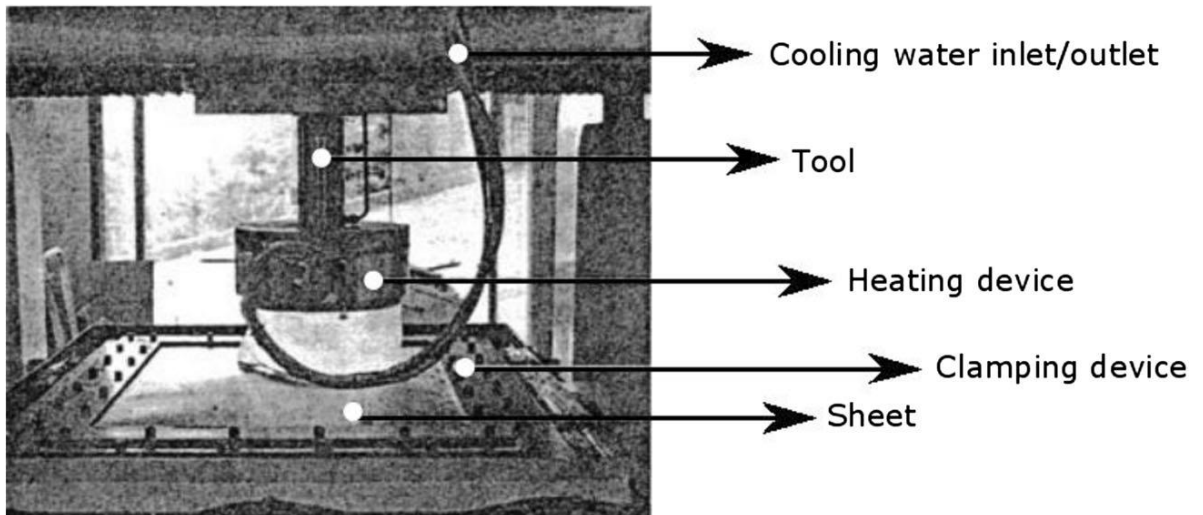
Figure 2.6 Warm Incremental Forming by using halogen lamps (Source: [62]).
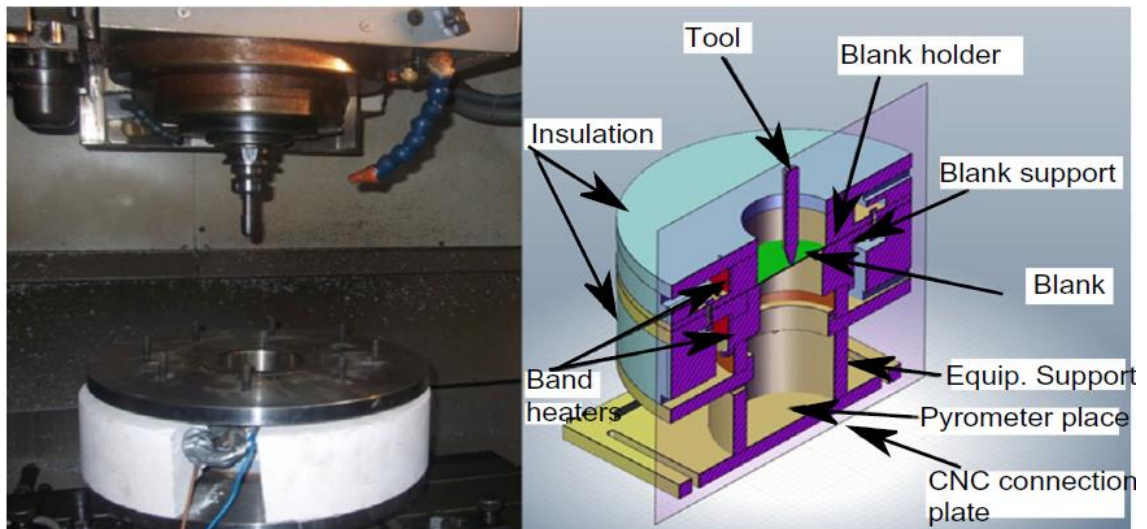

Figure 2.7 Heat-assisted SPIF with electric band heaters (Source: [63]).

Palumbo et al. [63] tried to manufacture a scaled car door shell from a 1 mm thick Titanium grade 5 which was heated by both static heating and the heat due to friction. Figure 2.7 shows the adopted setup for this experiment. Using electric band heaters, the whole sheet is heated up to a temperature of approximately 150 °C (centre zone) and the forming tool rotation in the range of 800-1600RPM results in a further temperature enhancement of about 100 °C and 180 °C respectively, creating a localised heating effect on the workpiece. Nevertheless, due to excessive friction at the tool stylus/workpiece interface, tool wear took

place leading to poor surface finishing of the final parts. Additionally, due to the position of the band heaters, a nonuniform temperature distribution is generated across the sheet.

Duflou et al. [45] presented the *Laser Assisted Single Point Incremental Forming* (LASPIF) process. This process variant allows to produce suitable dynamic temperature fields which supports SPIF process optimization. The LASPIF setup illustrated in Figure 2.8 allows to locally heat the part in a strategic area, close to the tool contact area, dynamically follow the forming tool movement, thus offering significant advantages.
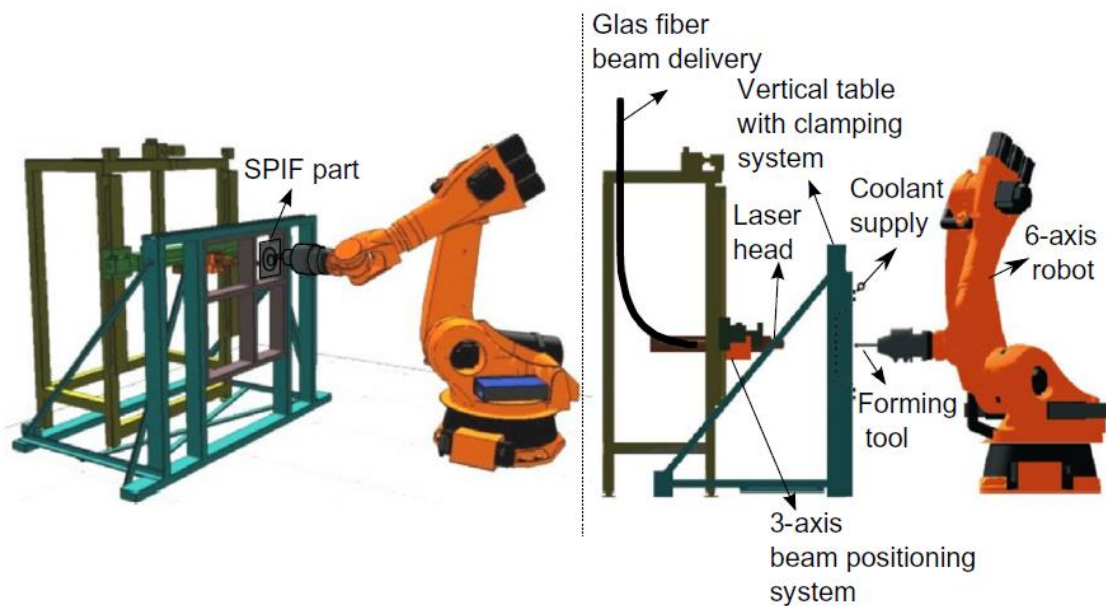

Figure 2.8 Laser Assisted Single Point Incremental Forming setup (Source: [45]).

The use of LASPIF process for forming AA5182 alloys resulted in force reductions in the forming tool direction up to 50% and the maximum forming angles of Titanium grade 5 sheets (0.6 mm thick) and 65Cr2 sheets (0.5 mm thick) were significantly improved to 56° and 64°, respectively, compared to 32° and 57° at room temperature. The improved accuracy, achieved by reducing elastic springback, was reported as an advantage of the strong dynamic temperature gradient resulting from the localised heating [50]. Since the introduction of this system, a three-dimensional transient heat transfer model has been developed to identify optimum process parameters for the heating process [64]. FE modelling results can be validated by temperature field measurements obtained from the IR camera system that was added to the platform. Furthermore, a number of recently recognized

opportunities of the LASPIF platform, such as the use of dynamic, in-process phase transformations to optimize the process have been introduced. Localized in-process phase transformation alters the material properties, the forming mechanisms and intermediate stress state of the sheet. They can be used to influence the sheet behaviour during the forming process [65].
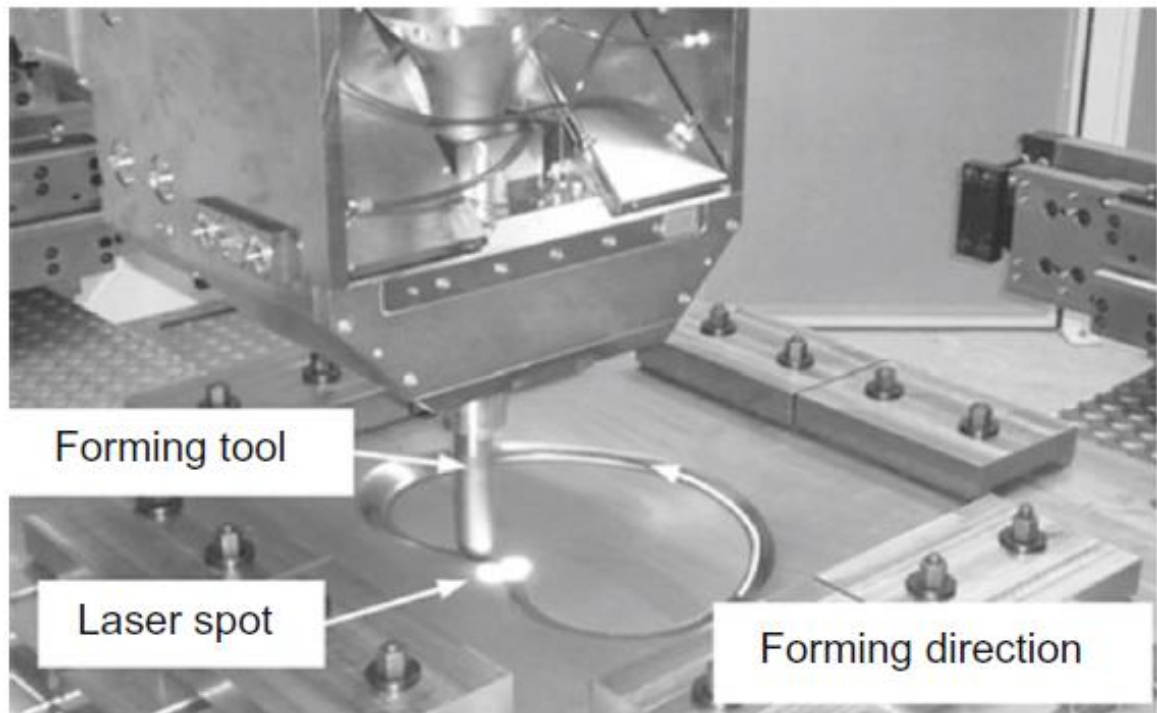

Figure 2.9 *Position of the laser spot on the workpiece during laser-assisted SPIF operation (Source:[66]).*

Another effort to create localized temperature fields by means of laser support in incremental forming was reported by *Göttmann et al.* [66]. In the proposed setup, the laser acts at the same side as the forming tool and the sheet is irradiated at a certain distance from the forming tool (Figure 2.9). The laser beam is guided around the forming tool by a dedicated laser optic which allows to rotate the laser focus point using mirrors and/or prisms. Presently, a limited knowledge is available concerning the optimal placement of the heat source. Heating the workpiece at a certain distance from the forming tool may be helpful in applications where the sheet has a high thermal inertia, but may have disadvantages for materials with high thermal conductivity in which no forward offset between the laser spot and the forming tool might be desired. In these cases, a CAM support is required to control the combined hybrid process setup. Lubricants are applied to the surface before forming.

Carbon-based lubricants reduce the reflectivity of the surface and hence increase the energy efficiency of the process. Using the laser-assisted ISF system, it has been shown that the formability of titanium grade 5 sheets (1.5 mm thick) could be increased by forming the material at temperatures of approximately 400 °C.
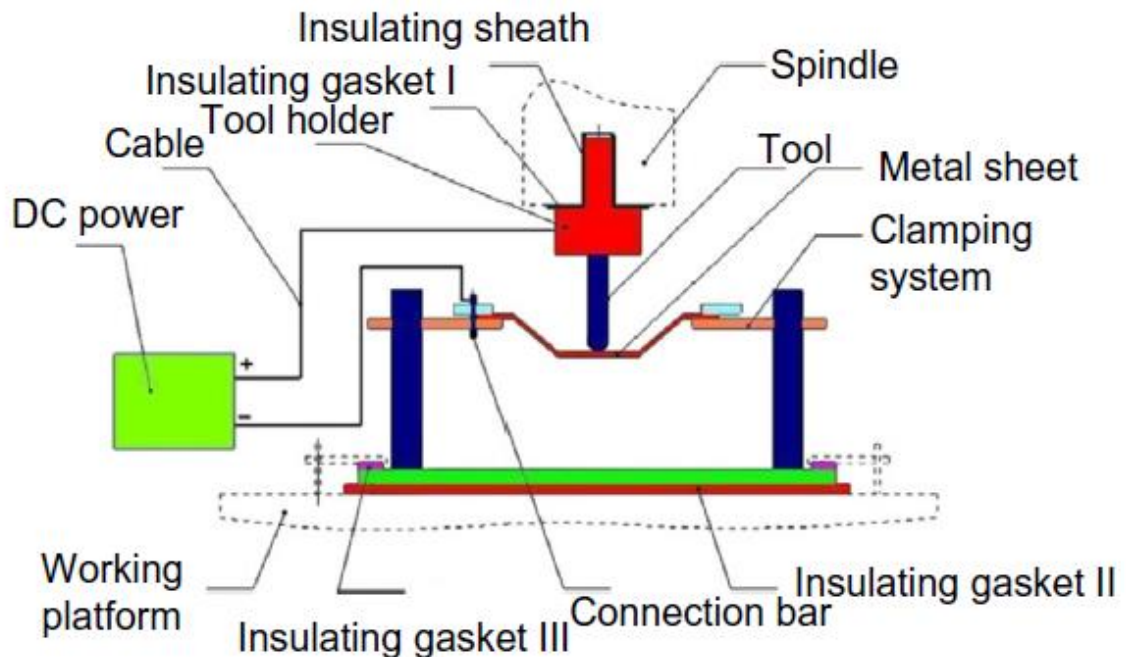

Figure 2.10 The Electric Hot Incremental Forming (EHIF) setup (Source: [67]).

Electric Hot Incremental Forming (EHIF) suggests another approach to the localized heating of the sheet. Based on the resistive heating law, when an electric current passes from the spindle through the sheet, the metal workpiece is locally heated up. The processing principle is shown in Figure 2.10. *Fan et al.* [67] studied the effect of different process parameters on the formability enhancement of AZ31 of 1 mm thickness, finding a maximum forming angle of about 64° for this material.

Although the EHIF technique seems to be economically sustainable and easy to employ, it has some limitations which should be properly taken into account. *Ambrogio et al.* [68] reported that the SPIF part wall angle and tool diameter are inversely proportional to the heat supplied to the sheet. Therefore, the adoption of a small tool radius might lead to local sheet burns because of the localized heat accumulation at the tool-sheet interface. Furthermore, heating cannot be localized completely since applying active cooling will affect the electric heating system, and without lubrication the surface finish is affected.

Speaking of **global heating**, *Ji and Park* [69], [70] studied high temperature formability in incremental forming of 0.5 thick AZ31 sheets by plane-strain stretching and axisymmetric stretching tests. The sheet is globally heated by hot air blowers and a significant increase in formability is achieved above 150 °C. Furthermore, by using a combination of multi-stage and warm incremental forming approaches, a maximum forming angle of 59° has been achieved at 150 °C. Figure 2.11 presents an egg shell surface which was formed using this process.
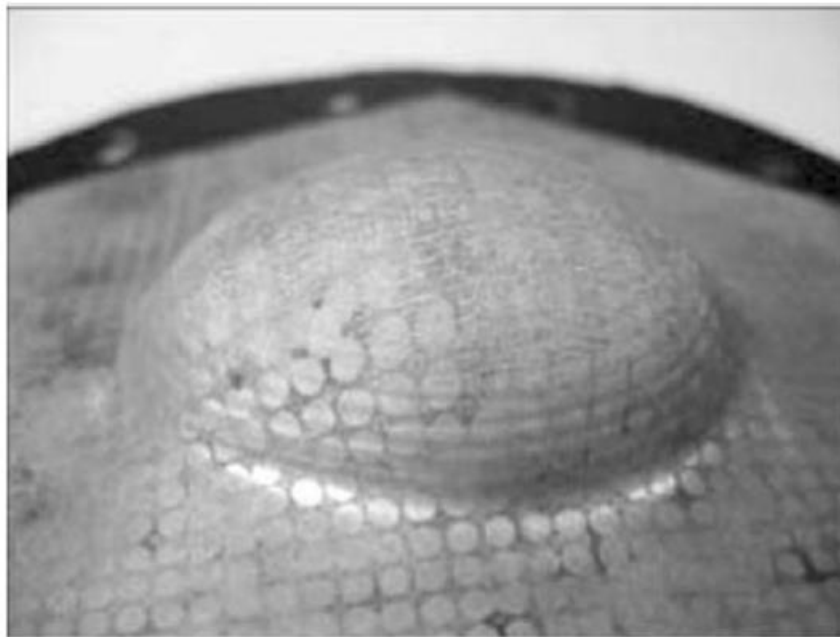
Figure 2.11 Egg shell manufactured on AZ31 sheet by Warm Incremental Forming (Source:[69], [70]).

Ambrogio et al. [71] studied the workability of AZ31-O sheets of 1 mm thickness under warm conditions. In this process the sheet metal has been heated by a heater band positioned around the circumference of the die and three thermocouples connected to the proportional-integral-derivative (PID) controller assured a constant temperature throughout the forming process. The complete set-up is schematically illustrated in Figure 2.12. The formability test results demonstrated that a maximum forming angle of 60° could be achieved at 300 °C. Furthermore, using the response surface methodology, it has been found that forming temperature and stepdown are among the most influential factors that play a role in determining forming limit diagram (FLD).
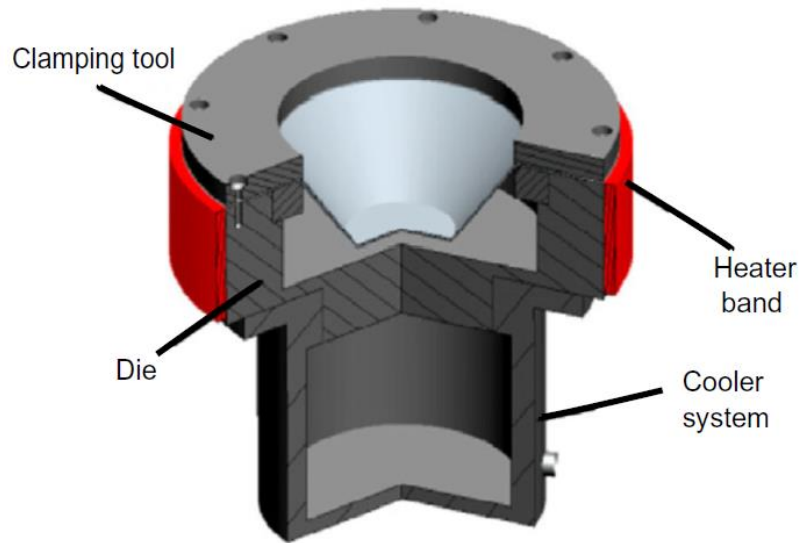
Figure 2.12 Electro-Assisted setup for SPIF operation with global heating (Source: [71]).

Galdos et al. [72] have introduced a physical configuration for warm incremental forming in which magnesium AZ31B alloy has been globally heated by using a hot fluid as a heating medium. Using a temperature control unit, the thermal oil used for this purpose can reach a temperature of up to about 300 °C and the sheet metal can be heated indirectly by convection in this medium. Figure 2.13 shows the set-up used for oil assisted SPIF. Microstructural investigations of the warm incrementally formed parts showed that full recrystallization is obtained at 250 °C. This is the temperature at which the maximum forming angle of 60° can be achieved. However, the maximum reachable temperature, by applying hot oil, is limited and this set-up can only be used for warm forming of magnesium and aluminium alloys.
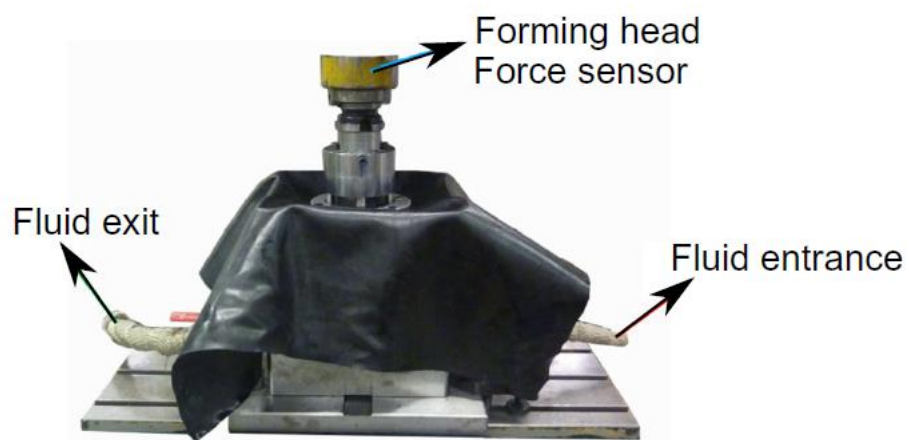

Figure 2.13 Oil-Assisted SPIF setup (Source: [72]).

As shown in Fig. 2.12, using electrical current has been demonstrated to effectively raise the formability of sheet metal [71]. One of the common phenomena that is observed is the current threshold density, a critical current density below which *Electrically Assisted Forming* (EAF) effects are very small. *Perkins et al.* measured this value for a variety of materials [73] and *Magargee et al.* [74] provided theoretical derivations and predictions of the threshold value for various engineering alloys (Figure 2.14). In order to model SPIF as an EAF process, it is necessary to model the contact area between the tool and sheet, as this is both the region where forming occurs, and the region of high current density. Further, as the shape of this contact area changes with part geometry and wall angle, better control of the process can be obtained by varying the current to apply the ideal current density at all times.

Adams and Jeswiet [75] created an analytical model of the contact region and used it to successfully verify that the current threshold density phenomenon occurs in SPIF of AA 6061-T6, resulting in a higher maximum wall angle when parts are formed just above the current threshold density. This knowledge may therefore be useful to create systems which vary the applied current during forming with changing contact conditions to prevent overheating of tools and lubricants [32].
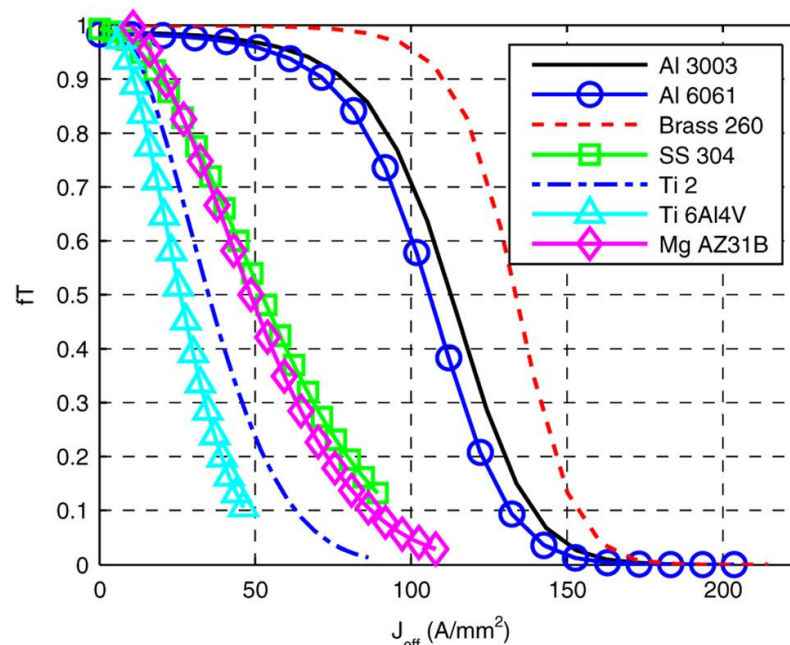
Figure 2.14 *Thermal softening parameter as a function of effective current density for different materials (Source: [74]).*

2.6. Summary and perspectives of SPIF

Although Heat-Assisted SPIF and Electrically-Assisted SPIF allow to enhance the workpiece formability performances, some drawbacks are evident. Because of the movement of the heating source and complexity of installing temperature sensors, most of the above mentioned localized warm forming processes suffer from a lack of accurate temperature measurements. In addition, the current literature excludes looking into control of the heat source to improve process outcomes, which is important from an industrial applications perspective. The correct tuning of EAF setup is still complicated, due to the current threshold density. Finally, a more complex and expensive setup reduces the typical flexibility owned by traditional SPIF process.

As depicted by *Behera et al.* [33], the exploration of optimized workpiece orientation (and its relative positioning with the tool) in improving process limitations has been minimal since the SPIF was created. This key aspect can be combined with multi-axes machine tool setups, enabling the tool to process the workpiece in order to optimize the draw angles.

In the next chapters, two innovative SPIF variants will be presented. *Multi-Directional multi-path SPIF* and *Magnetic Field-Assisted SPIF* (M-SPIF) are meant to extend formability limitation of lightweight materials in conventional SPIF. The relative simplicity of the process setup for both variants make them an appealing option for complex shape manufacturing.

The aim of this dissertation is to reduce the lack of knowledge present in literature regarding the above cited SPIF variants. *Multi-directional path SPIF* will be compared with conventional multi-path strategies to manufacture non-axisymmetric components characterized by flat edges in terms of geometrical accuracy of the final part. Through a deformation analysis it will be possible to determine critical zones of the process and how each different forming approach affects the final result. On the other hand, a new approach to the manufacture of complex geometries will be proposed in which the motion of the SPIF tool is controlled using magnetic force. The processing principle of M-SPIF, the design of the experimental setup to realize the proposed principle, and the feasibility test of this approach will be described in detail. Furthermore, The M-SPIF processing characteristics and mechanics will be discussed using an example of truncated cones formed in pure aluminium sheets. To achieve these results, extensive experimental campaigns have been carried out, developing dedicated numerical tools aimed at easing processes investigation and engineering.

3. An Innovative Strategy: Multi-Directional Path SPIF

3.1. *The Multi-path approach: historical background*

As discussed in paragraph 2.3, one of the main limitations affecting SPIF is the maximum wall angle (α): in fact, for every given sheet material and thickness, a maximum forming angle can be identified, exceeding which fracture tends to occur. In addition to material type and sheet thickness, this limit value also depends on a few other process parameters, i.e. tool diameter, stepdown (or vertical pitch, Δz) [76] and utilized toolpath. The presence of a maximum wall angle represents a limit to SPIF applications for parts characterized by vertical walls as, until now, no sound part can be obtained in a single step. For parts manufactured by single-stage SPIF researchers have adopted a simple geometric model, also known as the Sine Law [77], [78] to calculate wall thickness. According to this law, the expected thickness of a vertical wall should be equal to zero and then strains tend to infinity, representing the main drawback of single-step SPIF related to production of sheet metal parts with vertical walls. A possible solution in order to increase the maximum forming angle, as described in [79], is material redistribution by beckoning it from neighbouring zones in those immediately travelled by the tool. Other possible solutions, such as increasing the initial sheet thickness, cannot be adopted in the view of lightweight structures manufacturing and cost containment. For this reason, many authors have been focusing their attention on toolpath strategies in order to reach the desired geometry using a Multi-Step approach.
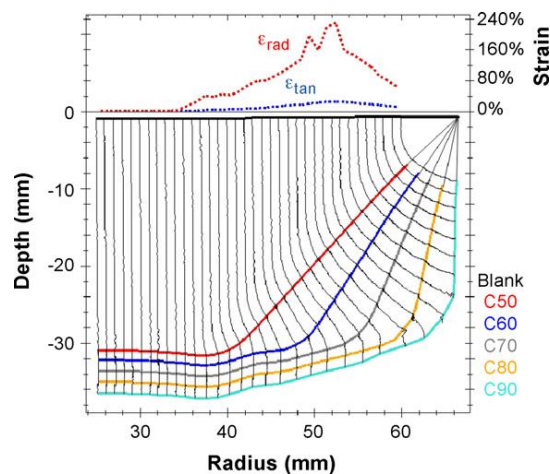

Figure 3.1 *Evolution of cylindrical cup shape obtained by multi-path SPIF (Source: 79]).*

Duflou et al. [79] utilized a five-step forming strategy with a 10° increase in the wall forming angle between an intermediate step and the following one in order to obtain a cylindrical wall on a Al3003-O sheet with a thickness of 1.2 mm , by choosing every single step configuration appropriately with the aim of avoiding any occurrence of the 'folding over' effect, thus producing a sound part (Figure 3.1).
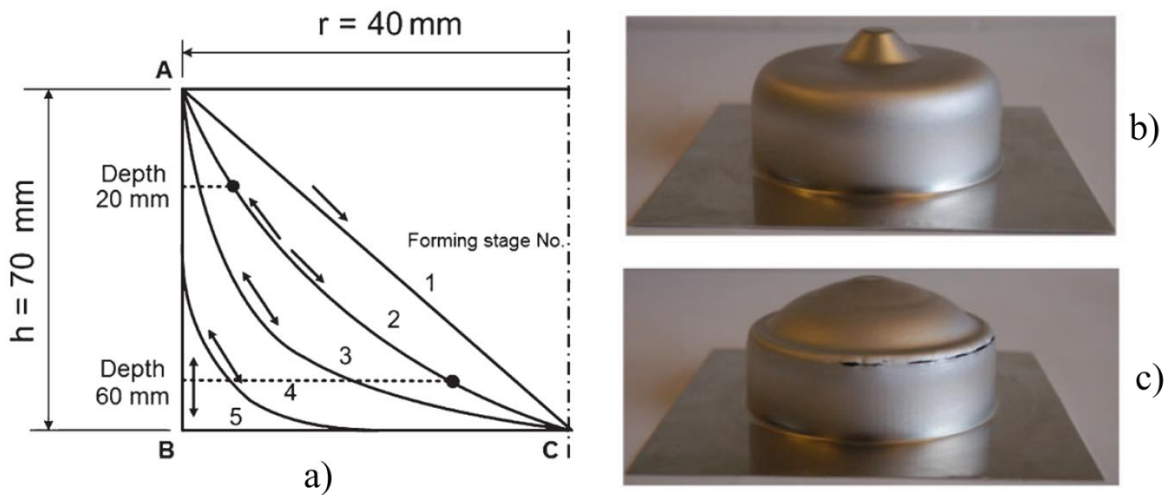

Figure 3.2 a) *Multi-stage SPIF strategy for cylindrical cup with vertical walls manufacturing; b) sound part obtained from a multi-stage DDDU strategy, c) failed part obtained from a multi-stage DUD(D) strategy (Source: [80],[81]).*

A different approach was proposed by *Skjoedt et al.* [80], [81]. Starting from a cone with 45° wall angle, a series of forming steps on AA1050-O sheet blanks of 1mm thickness were designed with the aim of progressively moving the middle of the wall region towards the corner of the final shape (cylinder). Several sequences have been tested in order to evaluate the best combination between upwards (U) and downwards (D) tool movement. The results showed that the DDDU strategy (Figure 3.2b) was the only successful one, allowing the production of the desired shape and showing that strain distribution depends on both the geometry and the direction (upwards or downwards) of the toolpath.

A comparison between different toolpath strategies for axisymmetric part manufacturing with vertical walls was carried out by *Liu et al.* [82]: incremental part diameter (A Strategy), incremental draw angle with a an increasing part diameter (B Strategy) and incremental draw angle with a simultaneous height increasing (C Strategy) were tested. The results of this work, provided in Figure 3.3, show how the combined strategy (A+B) allows to obtain a sound cylindrical cup as strategy A brings in a small quantity of bending, essential for controlling the material flow and thickness distribution, thus, delaying the occurrence of thinning band as well as potential fractures.
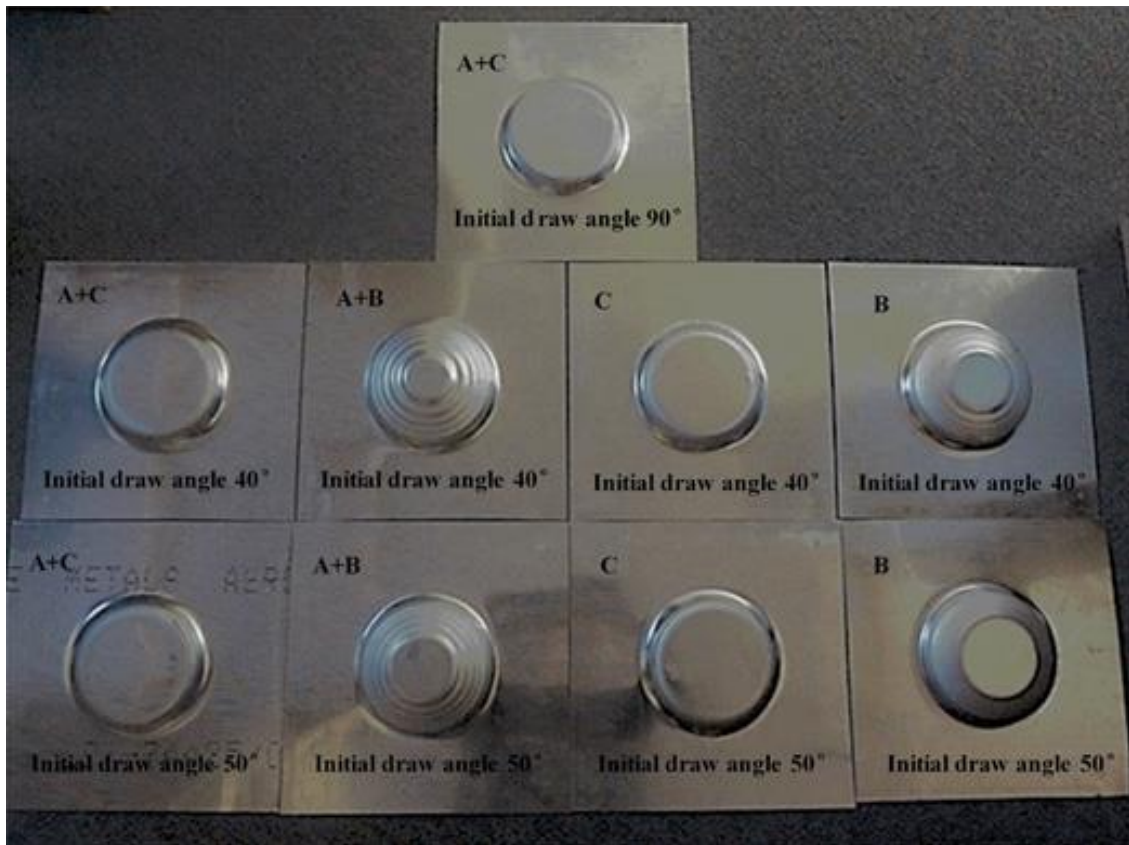
45

Figure 3.3 Obtained experimental shapes for different multi-path strategies combinations (Source: [82]).

It is worth noticing that a common feature of the previously mentioned studies [79], [81], [82] is represented by poor geometric accuracy. Along its path, the tool pushes the material downwards: a 'stepped' shape is thus obtained, higher than the desired one. In order to better understand this phenomenon, *Xu et al.* [83] developed an analytical prediction tool for stepped shape formation in Multi-Step SPIF in which material constants required a calibration by means of numerical simulations.

Although in recent years the concept of overcoming limits affecting SPIF thanks to the design of different intermediate steps (and then different toolpaths) able to guarantee a better in-process material flow control has been analysed by a few authors, the attention has been largely focused on axisymmetric components [84]. Non-axisymmetric parts, such as pyramid frustums, are characterized by sharp edged zones in which a unequal biaxial stretching is the main deformation mode, rather than plane strain stretching of the wall region [54], and the zones between vertical walls are the critical ones due to the small fillet radii to be shaped. As incremental forming based processes are regarded, very recently *Russo et al.*

[85] focused their attention on new methods for Multi-Step toolpath design for non-axisymmetric components produced by Spinning process.

Finally, an innovative approach in Multi-Step SPIF was introduced by *Tanaka* [86], which carried out a preliminary study regarding a square cup with 90° wall angle manufactured diversifying forming directions between each forming step. This strategy, consisting of 9 subsequent operations, allows proper material redistribution from the thicker zones to the thinner ones, showing that a right choice of deformation path may be the key point in complex geometry manufacturing.

3.2. Experimental and Numerical Campaigns

3.2.1 Forming Strategies

On the basis of the literature analysis presented in the previous paragraph, three different strategies have been selected and evaluated in order to determine the best solution for the manufacturing of a 54x54x25 mm square cup: incremental increase of wall forming angle (A Strategy), incremental increase of wall forming angle with an increasing part side (B Strategy) and finally the adoption of non-horizontal path planes (C Strategy). The A strategy (Figure 3.4a) represents one of the first attempts to increase the material flow from undeformed zones of the workpiece, especially from the bottom part, to the highly deformed ones. The adoption of this strategy led to successful results in vertical wall manufacturing for axisymmetric components [79]. For this reason, A Strategy feasibility, starting from a 50° wall angle, was considered for a square cup characterized by small fillet radii between vertical walls.
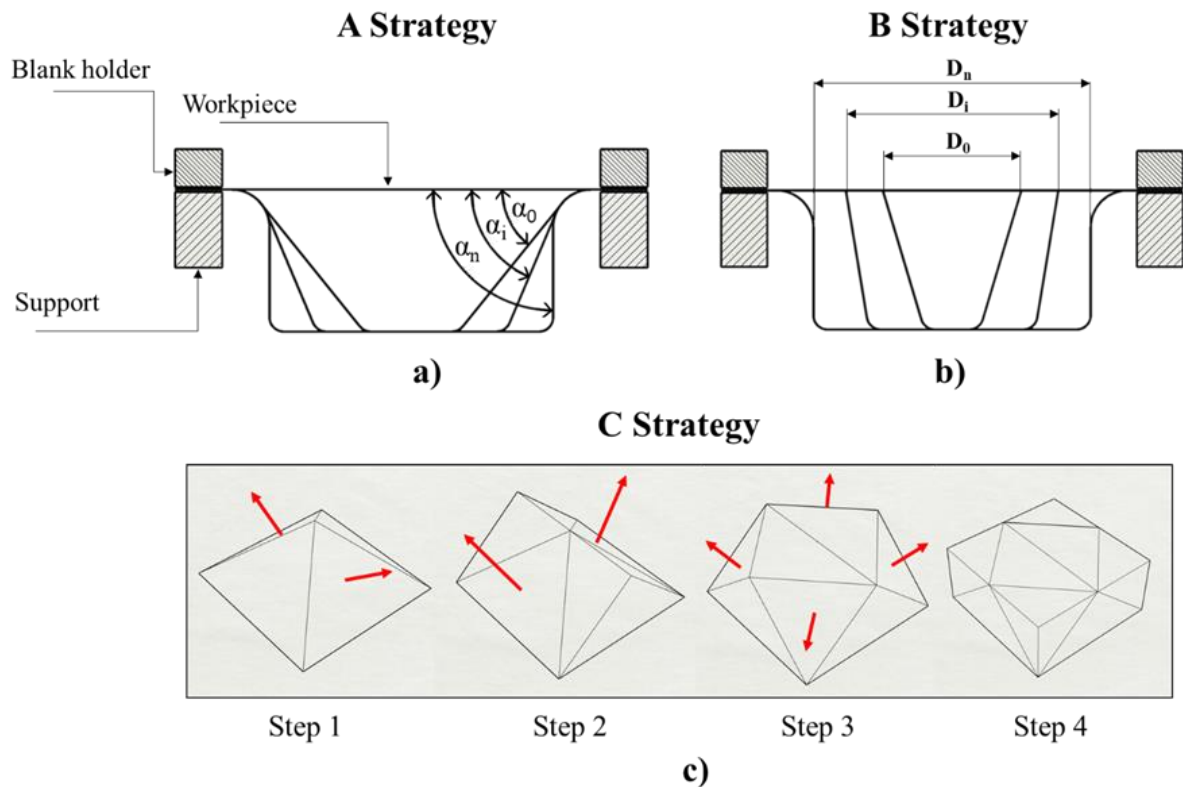

Figure 3.4 *Schematic of the adopted strategies: (a) A strategy, (b) B strategy and (c) C strategy.*

The B Strategy (Figure 3.4b) has been used to produce a sound cylindrical cup [82] as it takes advantage from both the increasing wall forming angle approach and the progressive addition of material involved in the plastic flow by means of base diameter increasing. This results in a better control of severe thinning affecting both the walls and the corners during each step of the manufacturing process. Strategies A and B share a "traditional" deformation approach based on a tool forming action along vertical direction, which is why in this study they were compared at the same wall forming angle for every single step.

The C Strategy (Figure 1c), unlike the previous two, introduces the concept of the forming direction differentiation with the aim of increasing the number of workpiece areas from which material can be beckoned, so as to further extend formability limits of Multi-Step process. The C strategy consists of four steps, for a total of nine SPIF operations: Pyramid (1° Step, one operation), Roof (2° Step, two operations), Poly-Surface (3° Step, two operations) and Square Cup (4° Step, four operations). In every single operation (except the first), workpiece tilt angle is changed appropriately so that the tool travels perpendicularly to the facet to be worked. It is worth noticing that other forming strategies introducing an incremental part height increase have not been considered because they did not show any advantage in previous forming tests on material flow control in order to reduce thinning [82]. The process parameters characterizing every step of the three strategies are reported in Table 3.1.

Table 3.1 Geometrical Parameters for Every Single Step

Strategy	Step 1	Step 2	Step 3	Step 4	Step 5
A	Side = 54 mm $\alpha = 50°$	Side = 54 mm $\alpha = 60°$	Side = 54 mm $\alpha = 70°$	Side = 54 mm $\alpha = 80°$	Side = 54 mm $\alpha = 90°$
B	Side = 48 mm $\alpha = 50°$	Side = 49.5 mm $\alpha = 60°$	Side = 51 mm $\alpha = 70°$	Side = 52.5 mm $\alpha = 80°$	Side = 54 mm $\alpha = 90°$
C	**Pyramid** 1 SPIF Operation Base: 54x54 mm Height: 25 mm	**Roof** 2 SPIF Operations Sheet Tilt Angle: 42.8°	**Poly-Surface** 2 SPIF Operations Sheet Tilt Angle: 42.8°	**Square Cup** 4 SPIF Operations Sheet Tilt Angle: 52.6°	/

3.2.2 Experimental Setup

All the experimental tests were carried out on a 4-axis CNC milling machine (EMCO PC MILL 300). For the three different strategies, each operation was carried out using a tool with a 4 mm hemispherical tip, a tool feed-rate of 600 mm/min, a stepdown of 0.1 mm/rev and a spindle speed of 50 rpm. Each specimen was lubricated with oil during the forming process. With the aim to adopt a single experimental setup suitable for all strategies, and in particular for Strategy C, a clamping fixture (Figure 3.5) was specifically designed and manufactured to allow both the rotation along the X axis (using the fourth axis of the used CNC milling machine) and the rotation along the Z axis of workpiece between a forming step and the following one. This allowed the correct positioning of the working area in relation to the tool forming direction, and ensured that in every single step the facet to be worked was positioned perpendicularly to vertical axis. For the experiments, aluminium AA1050 sheets with dimensions 200x200x1 mm have been fixed to a circular crown with an external diameter of 180 mm. Deformation analysis was carried out by means of CGA (Circular Grid Analysis) method. A 100x100 mm grid of circles was applied on each sheet by laser engraving (engraving depth ≤ 0.05 mm). By an optical microscope, major and minor axes of the ellipses resulting from engraved circles deformation were measured.

This allowed a direct comparison of the strategies object of study, highlighting the different deformation modes characterizing each zone of the workpiece.
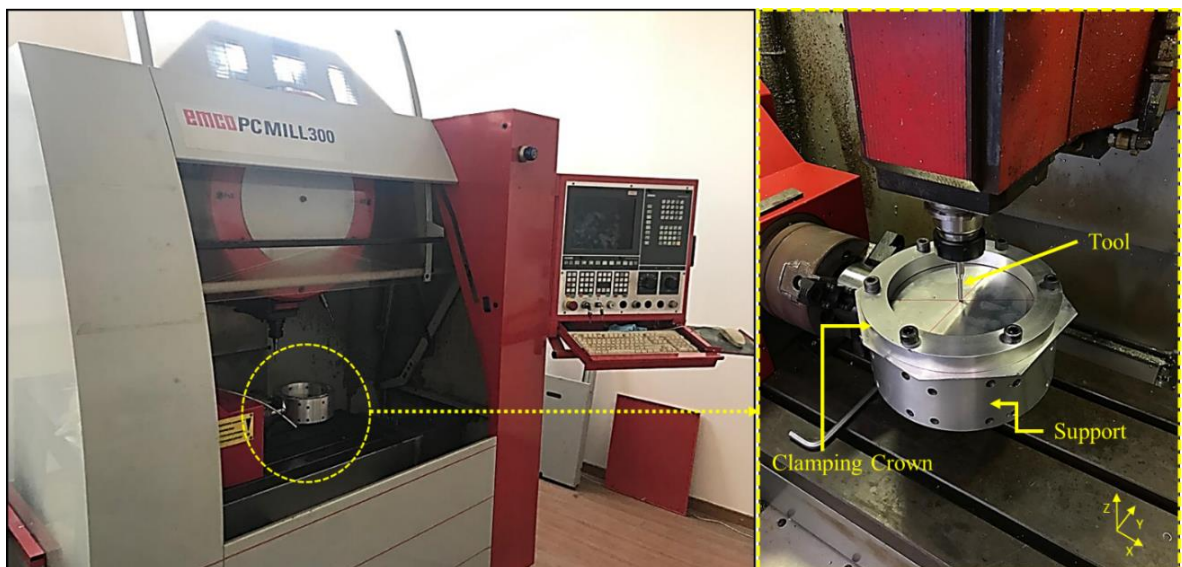

Figure 3.5 Experimental Setup and clamping fixture.

3.2.3   FEM Model

In order to better understand how different subsequent forming steps may affect strain distribution and material flow all over the workpiece, a numerical model was set up. The finite element simulation was performed using Abaqus/Explicit® commercial software: 1mm-thick S4R shell elements (5 integration points through the thickness) were adopted for the workpiece. The tool was considered as a rigid body. Surface-to-surface contact with a friction coefficient assumed to be 0.05 was set. Material elastic behaviour was modelled by Young's modulus E=69000MPa and Poisson's coefficient ν=0.33, while the plastic behaviour was defined according to the Hollomon's law $\sigma = 146.9\ \varepsilon^{0.3}$ MPa.

As strategy C is considered, the 9 consecutive SPIF operations representing the 4-Step approach were simulated separately by importing the results of the previous forming step from time to time by means of a Predefined Field in order to take into account the effect of deformation in the different areas of the workpiece (Figure 3.6). Intermediate simulation steps were also carried out to take into account the sheet metal part rotation.
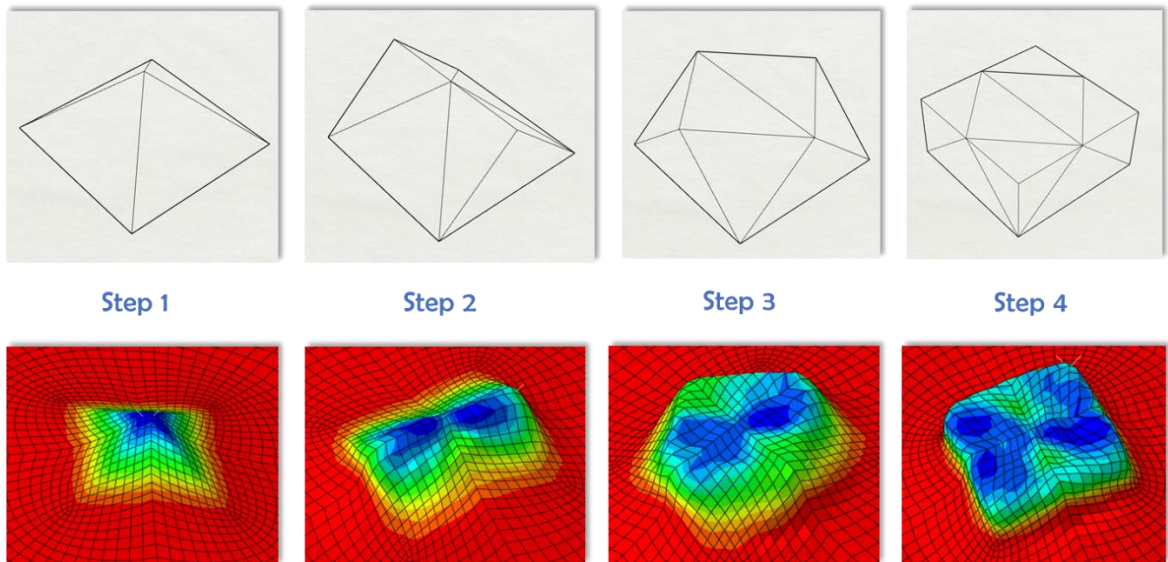

Step 1   Step 2   Step 3   Step 4

Figure 3.6 Overview of C Strategy numerical simulation.

3.3. Obtained Results

3.3.1. Defects Analysis

A, B and C Strategy were performed in order to obtain a square cup with vertical walls. The experimental results are reported in Table 3.2 and Figure 3.7, from which it is possible to deduce the influence of different approaches in forming direction on the final outcome. In particular, both A Strategy and B strategy led to failure after passing a 70° wall forming angle, while C Strategy was the only one allowing to manufacture a sound part.
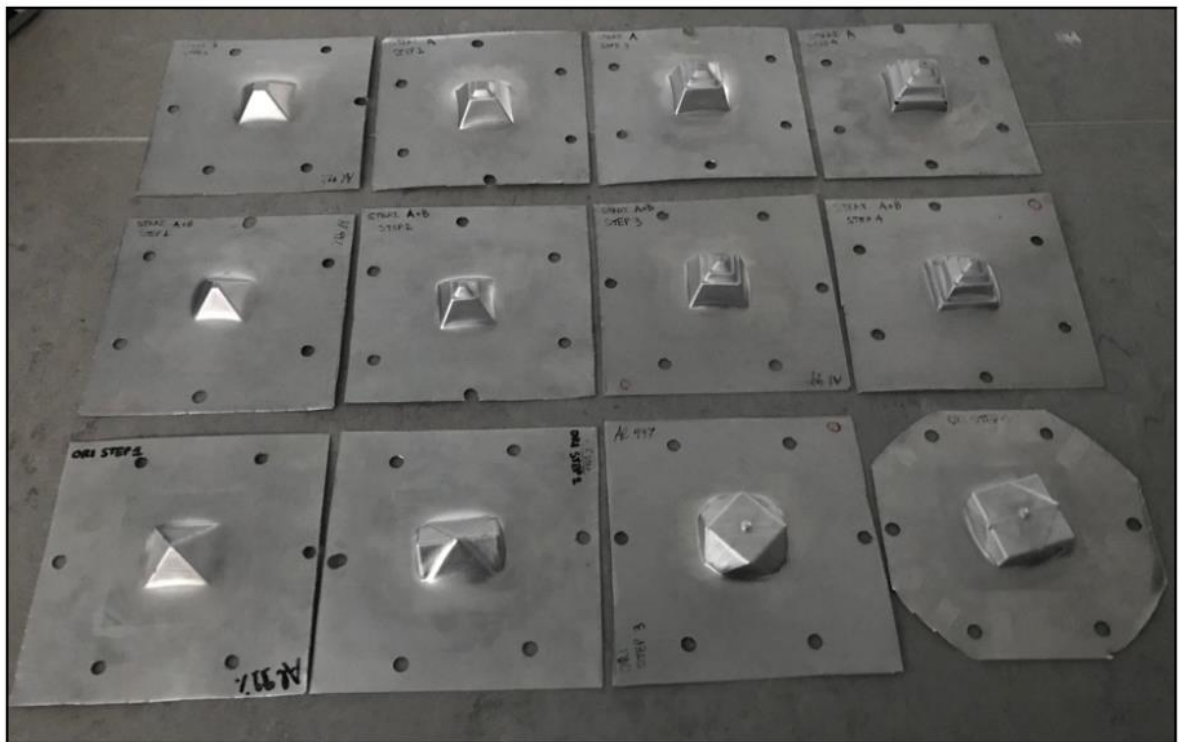
Figure 3.7 *Obtained results for A (first row), B (second) and C (third) Strategy.*

As expected, for strategies A and B the fractures are located at corners, as these are the most critical areas of the forming process due to the small fillet radii. The part manufactured with A Strategy showed fracture at corners after a vertical tool descent of 8 mm during Step 4 (α=80°). Likewise, the adoption of B Strategy led to failure at Step 4 (α=80°) at about 6.5 mm of depth. Although these two strategies showed successful results in literature for axisymmetric part manufacturing [79], [82], [87], they turned out to be inefficient in presence of fillet zones between the walls characterized by high slope values (close to 90°).
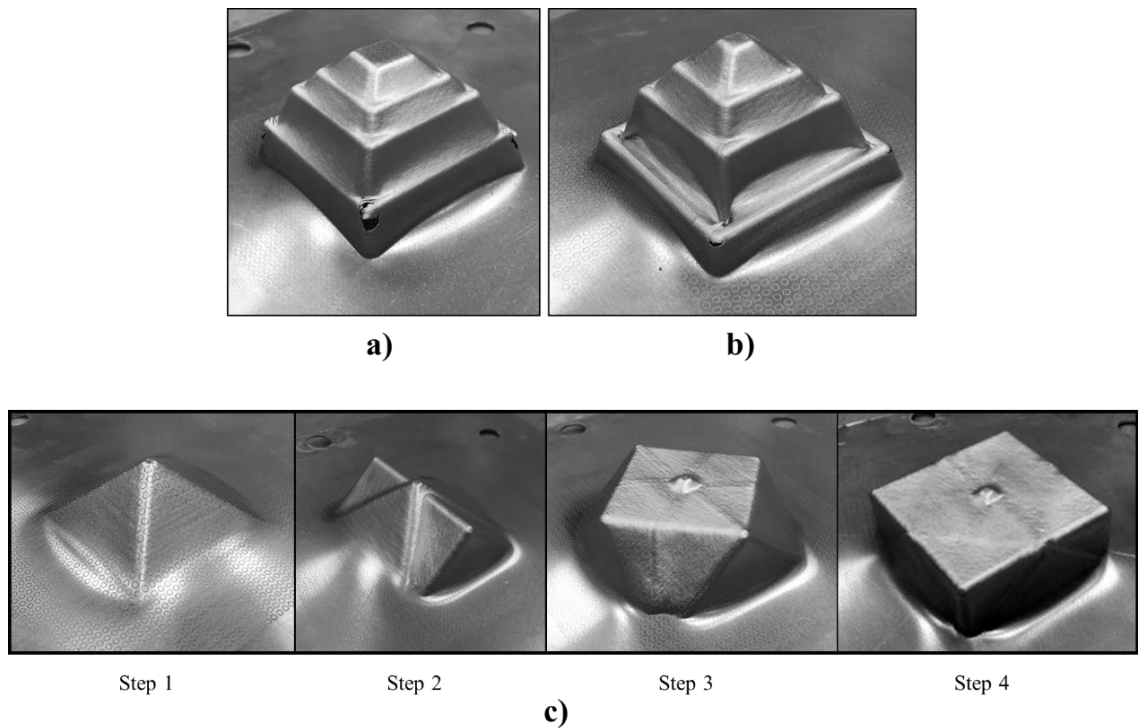
Figure 3.8 *Fracture details at corners for a) A Strategy and b) B Strategy; c) square cup multi-step manufacturing by means of C Strategy.*

It has to be also highlighted that both A and B Strategy show a poor geometrical accuracy starting from Step 2, due to rigid motion of the bottom part downwards, as can be seen in Figure 3.8: this phenomenon entails an undesired increase in the final height, as well as an irregularity of the bottom in the final component. As confirmed by previous experiments [81], [82], [88], during the steps following the first the downwards action of the tool involves the formation of a "stepped" shape underneath, although the toolpath depth remains the same for all Steps (25 mm). This phenomenon has not been observed for C Strategy, which allowed to obtain the desired part height and a flat bottom (Figure 3.8c). It should be observed that, for this approach, other possible geometric defects, *i.e.*, at the bottom centre or connection areas between several working facets, may be avoided by adopting an accurate centring system.

Table 3.2 *Square Cup Manufacturing by means of A, B and C Strategy: Experimental Results.*

Strategy	Step 1	Step 2	Step 3	Step 4
A	Success α=50°	Success α=60°	Success α=70°	Failure α=80°
B	Success α=50°	Success α=60°	Success α=70°	Failure α=80°
C	Success	Success	Success	Success

The developed numerical model was validated by comparing, for the C Strategy, the experimentally measured and numerically calculated thickness distributions in a cross section at an offset of δ=10 mm from centre of the square (Figure 3.8). From the figure it can be seen a good agreement between experimental and numerical results. Additionally, a non-uniform thickness of the part base is observed, with thinning values ranging between 0 and 65%.
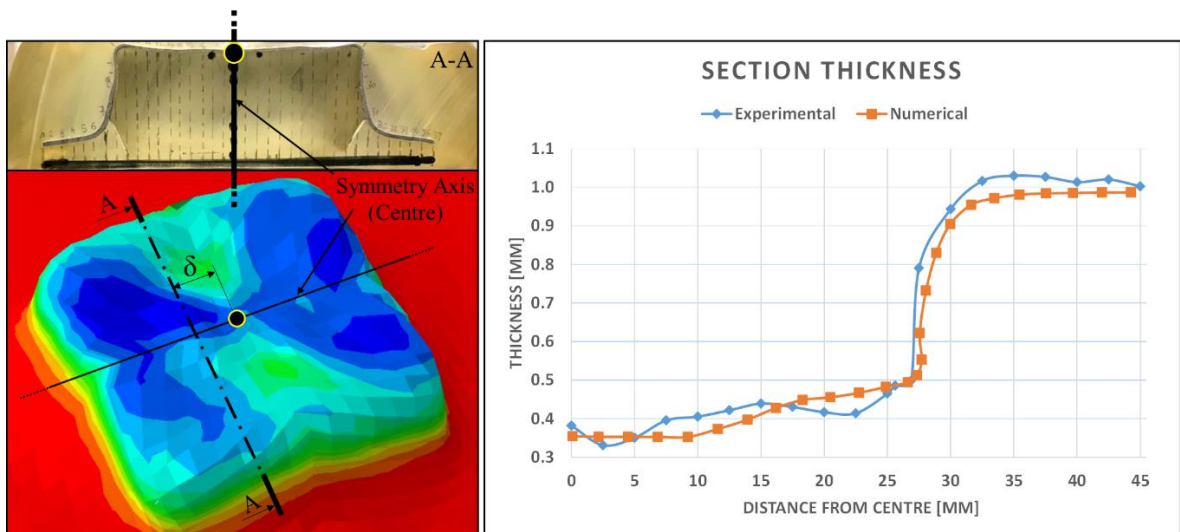
Figure 3.8 *Square Cup section thickness: experimental and numerical results.*

3.3.2. Strain evaluation

In Figure 3.9 a detail of fracture locations and inner defects at Step 4 for A and B Strategy is illustrated. For both Strategies a horizontal discontinuity at fracture depth between the wall part already processed (α=80°) and the one to be processed (α=70°) can be observed. In fact, a horizontal offset of tool position between two consecutive forming steps occurs. As the tool goes downwards, this offset value tends to increase involving the formation of a plateau on which the tool pin proceeds during the process. If the horizontal offset value exceeds the tool diameter, the occurrence of the "folding over" defect is possible and therefore failure is more likely to occur. A sketch of the process showing the causes of the folding over defect formation and the differences between the two approaches is shown in Figure 3.10. It is seen that, using Strategy A, according to which the different steps differ only for the increase of the wall angle while the dimension of the spire at the base remains the same, a certain step (Δx_A) can be formed. On the other hand, when Strategy B is used, from step *n* to the following step *n+1* both an increase of the wall angle and of the dimension of the spire at the base of the cup occur. In this way, the horizontal step (Δx_B) is larger. It is noted that the occurrence of this defects also results in a downward rigid body motion of the bottom of the cup (RBM_Z) further decreasing geometric accuracy. This phenomenon depends on a few parameters, *i.e.,* tool diameter, final part height and angular offset, increase of the dimension of the spire at the base of the cup ("base increment", Figure 7). Although it can be decreased using small increments of wall forming angle between each step for both A and B Strategy, for the geometry considered in this study, *i.e.,* square cup, it was found that the folding over occurred also for angle increments as low as 5°.

a)   b)
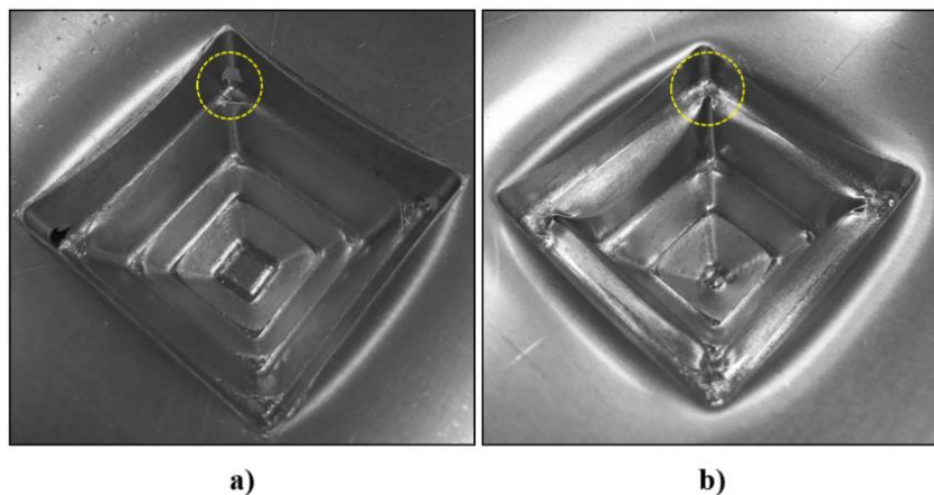
Figure 3.9 *Inner fracture and "folding over": a) A Strategy, b) B Strategy.*
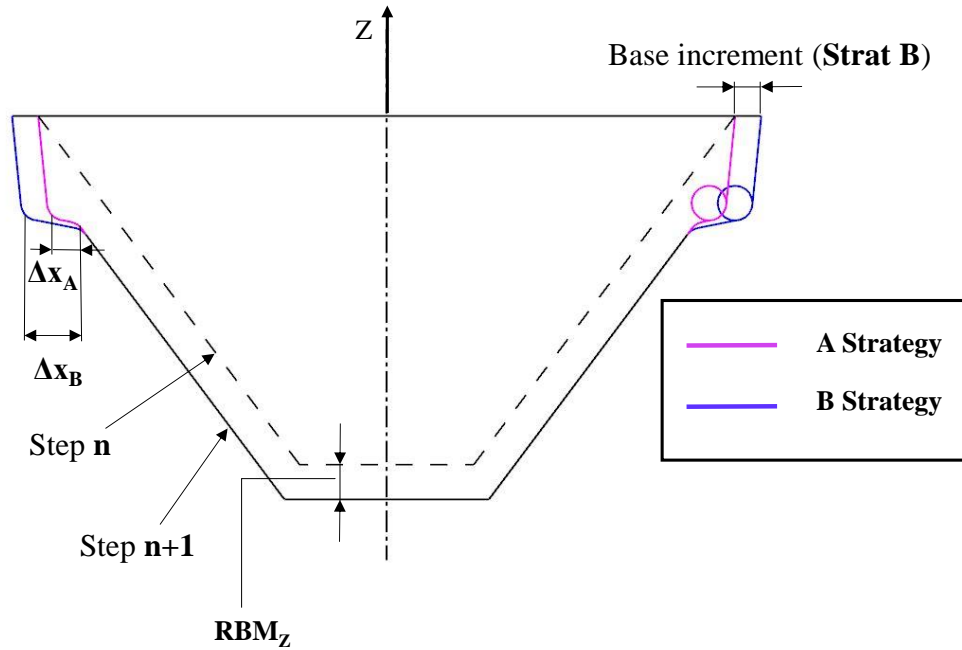
Figure 3.10 Horizontal discontinuity formation for A and B Strategies.

As the "base increment" is considered, its increase results in both an initial bending at the beginning of each step, helping formability, and into an increase of the horizontal discontinuity width, which can lead to the undesired "folding over" defect. These concurrent effects require a careful choice of this parameter in order to find a compromise solution. In this study, although a small base side increment of 1.5 mm for each step has been set for B Strategy, the formation of a horizontal discontinuity was observed, leading to the folding over onset, then to failure in those zones. As already mentioned, the same defect was found for the A Strategy, although with a smaller horizontal discontinuity width because of constant dimension of the base spire, as, in comparison with axisymmetric part manufacturing, the folding over defect is even more emphasized for complex shapes with elements characterized by small fillet radii.

Figure 3.11 *Major and minor strain values for the A and B Strategies.*

The distribution of major and minor strain values for the A and B Strategy is plotted in Figure 3.11. For both strategies it is possible to distinguish two working areas, characterized by differen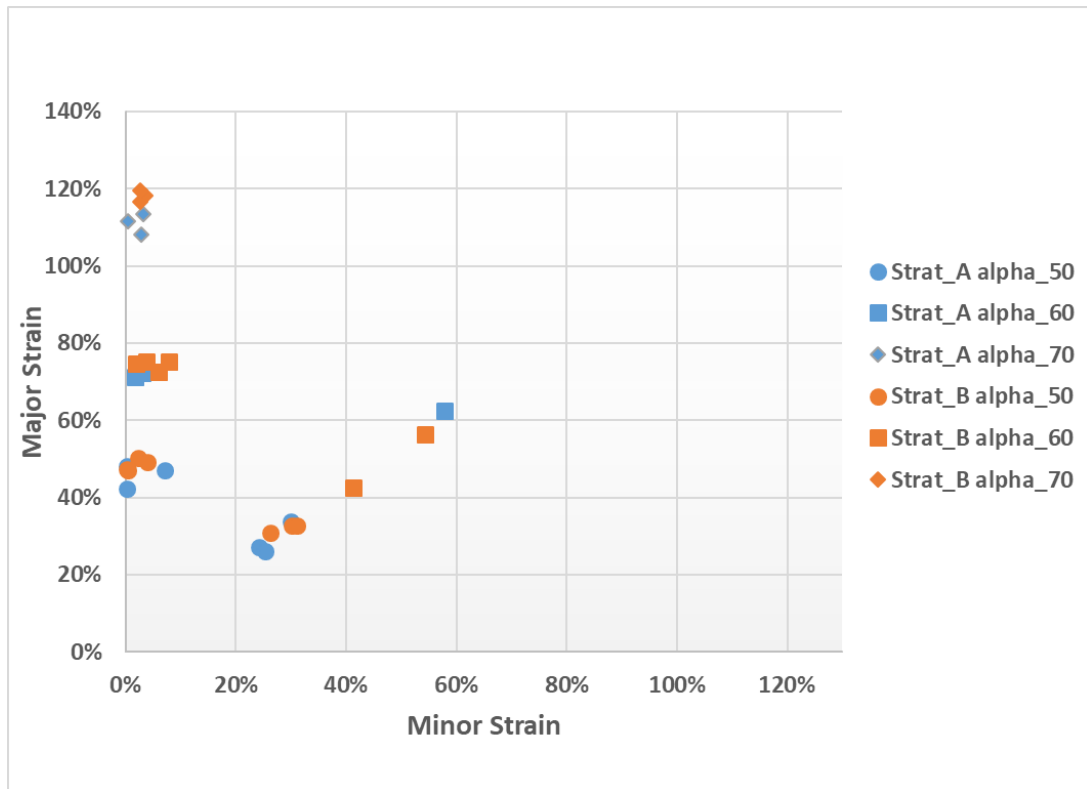t deformation modes during the process: the wall zone, in which deformation is consistent with stretching (minor strain close to zero), and the corners, where a biaxial deformation is predominant. The obtained results at corners are in according to what has been found in [54] for pyramid frustum manufacturing: biaxial deformation turns out to be unbalanced, with major strain values slightly greater than minor strain ones. This may be justified by a different average thickness of the material already processed above the tool and the one surrounding it at a certain depth as well as by a different stiffness between circumferential direction and meridional direction during the forming process. It is noticing that major and minor strain values at corners have been acquired until Step 2 (α=60°) for both strategies: starting from Step 3 (α=70°), it can be seen how in these zones, characterized by quite small fillet radii, a state of incipient necking has been reached due to severe deformation, leading to failure at Step 4. Along the walls, stretching increases with the forming steps, reaching major strain values up to about 120% at Step 3. It is worth mentioning that a similar behaviour, and then similar deformation values, have been

observed, for A and B Strategy, for all the analysed steps. In fact, as the two strategies share both the same tool direction and the same process parameters, it is expectable the similarity of the obtained results.
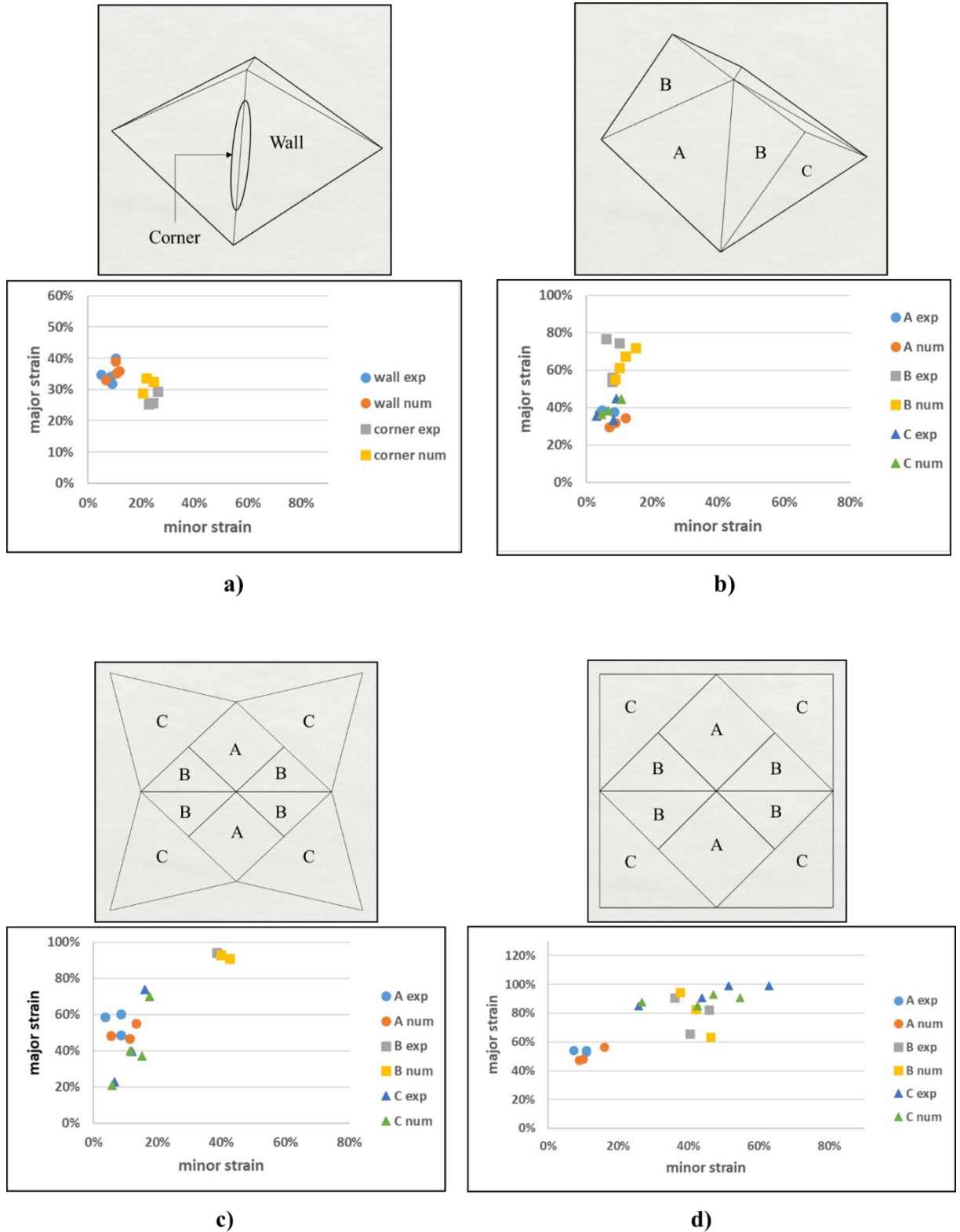

a)

b)

c)

d)

Figure 3.12 *Major and minor strain distribution, C Strategy: (a) Step 1, (b) step 2, (c) base partition step 3, (d) base partition step 4.*

As strategy C is regarded, experimental and numerical distributions of major and minor strain values for every forming Step are plotted in Figure 3.12. As it can be seen, a simple partition of the workpiece in wall and corner zones, characterized by stretching and unequal biaxial deformation conditions respectively, is no longer valid. The adoption of a multi-directional forming process approach involves the onset of different deformation zones in which the strain path undergoes a continuous evolution across the different steps. Several zones of the workpiece are processed by the tool more than once and with different directions, thus making possible different strain conditions within the same facet. It should be observed that no necking defect at corners of the final component was observed, indicating that deformation modes of Strategy C results in a better material redistribution from the thicker zones to the thinner ones, preventing any risk of failure in spite of the small fillet radii required at corners. The key of Strategy C success is a better sheet material usage, especially regarding the bottom part. Due to the adopted toolpath and to the mentioned undesired geometrical defects, mono-directional multi-path strategies allow to use just a small amount of material coming from the bottom part, *i.e.*, where smaller deformations are observed, for the formation of walls and corners, *i.e.,* where larger deformation occur, resulting in excessive thinning and leaving most of the sheet bottom unprocessed.
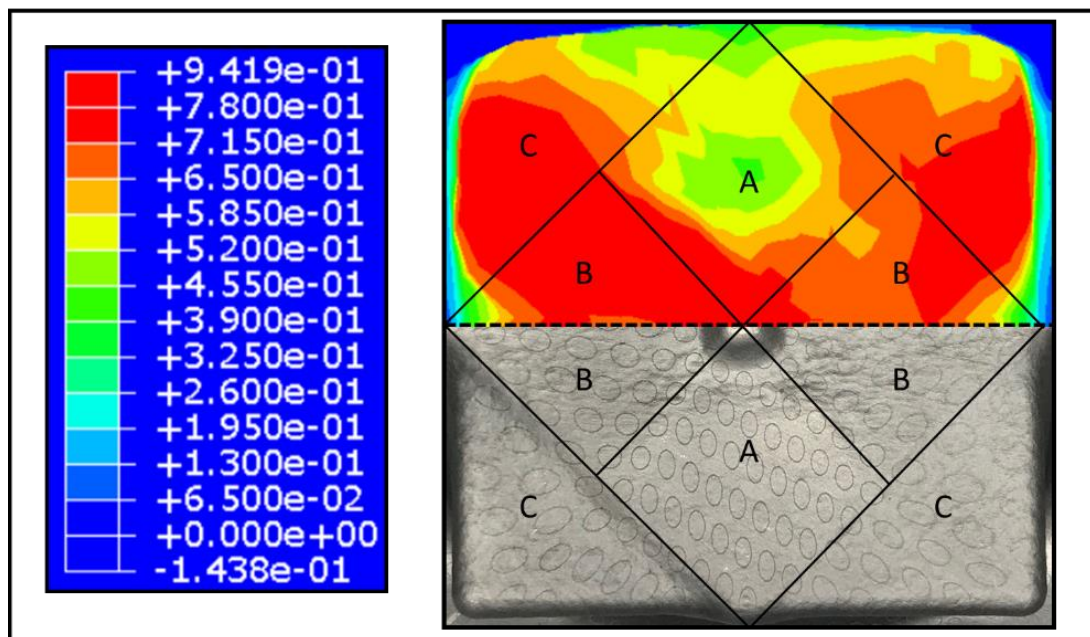

Figure 3.13 *Material flow at bottom part: a comparison between major strain distribution and the obtained grid deformation.*

Figure 3.13 shows the major strain distribution at the bottom of the formed square cup as calculated by the developed numerical model for Strategy C. The grid deformation experimentally obtained at the end of process and the schematic of the base areas are shown as well. It is observed that besides the corner areas "C", where large deformations are expected, significant values are found also at the centre of the base, *i.e.,* areas "B". In this way, it can be highlighted how material flow differentiation at bottom, as well as a more complete use of this workpiece area, allowed to increase formability limits of the process, paving the way to more complex shapes manufacturing.

3.3.3. Final Considerations

Three different Multi-Step strategies for the production of a square cup by single point incremental forming were considered. In particular, a multi-direction approach was compared with two mono-directional approaches with the aim to highlight the differences in part integrity, deformation distribution and material flow. From the obtained results the following main conclusions can be drawn:

• Although the mono-directional strategies A and B have been applied successfully in literature for axisymmetric part manufacturing, their adoption for the production of flat walls components characterized by small fillet radii resulted in failure at corners.

• The formation of a horizontal discontinuity characterized by a greater width value at the corners was observed for both A and B strategies, leading to the "folding over" onset and then failure in those zones. The extent of horizontal discontinuity at fracture depth is more relevant in Strategy B because of the base side increase at each step: this involves also a lower depth at which fracture occurs, showing that B Strategy cannot represent a possible improvement of A Strategy for non-axisymmetric part manufacturing.

• From the deformation analysis arises that no significant difference in strain path emerged between A and B strategies, whereas C Strategy introduction leads to material flow diversification and different strain conditions within the same facet.

• The material usage from multiple workpiece areas and the optimized bottom part exploitation are the key aspects of the C Strategy success: the section thickness as well as the experimental and numerical strain analysis demonstrate how this area, from which A and B strategies allowed to channel just a small amount of material, is the key to redistribute it where needed avoiding the onset of fractures.

4. The Magnetic Field-Assisted SPIF

4.1. Introduction to M-SPIF

It has been pinpointed many times in this dissertation how Incremental Forming processes have drawn attention in many industrial sectors (such as the automotive, aerospace, and medical industries) because of their ability to produce lightweight structures of various geometries without tooling modifications, as well as their enhanced formability limitations compared to traditional forming processes [34], [89]. However, several limitations, such as relatively long production time and low geometrical accuracy, need to be overcome to increase practical Incremental forming application [84].

As discussed in Paragraph 2.5, a few variants of Incremental Forming have been developed to address some of the drawbacks. For example, High-speed SPIF enables forming of titanium sheets [41]; Die-less robot-based Incremental Forming improves geometrical accuracy of formed parts [90]; Multi-Path SPIF [79], [80] and Heat-Assisted SPIF [91]–[93] have shown enhanced sheet-metal formability with wall angles equal to 90°. Another concept, using a magnetic field to boost the performance of a sheet-forming process [94] has been applied for the first time to Incremental Forming processes in *Electromagnetic Incremental Forming* (EMIF).
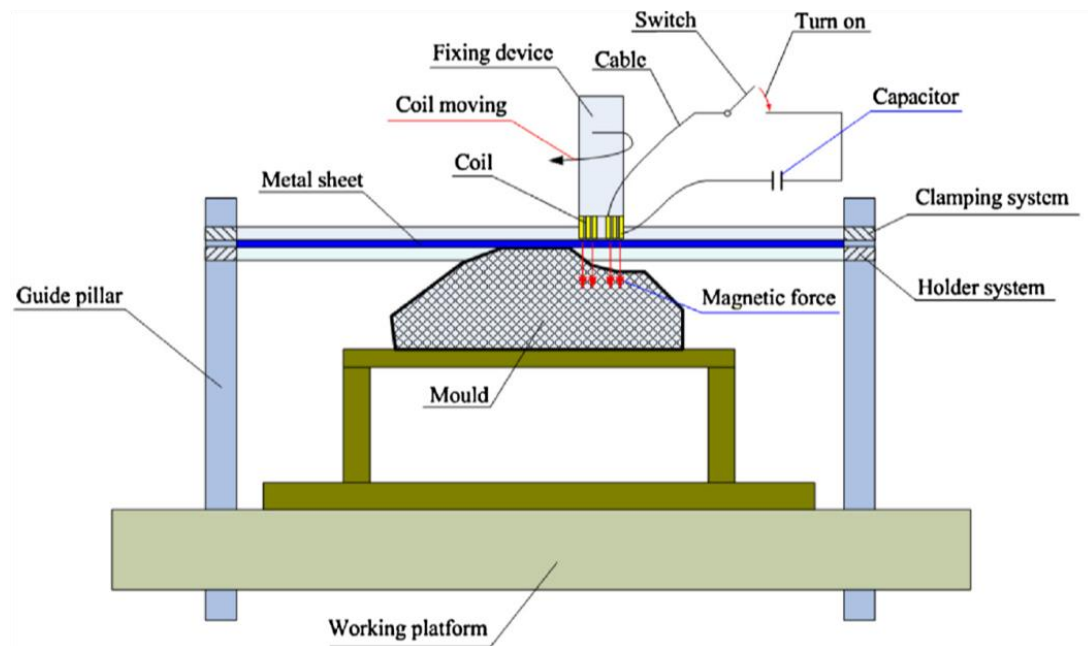

Figure 4.1 *The Principle of EMIF Process (Source: [95]).*

The proposed EMIF principle by *Cui et al.* [95], [96] is shown in Figure 4.1. In this process, the electrical energy is stored in a bank of capacitors: by discharging all the stored energy, a time-dependent discharge current runs through a coil, producing a transient magnetic field around it. According to Faraday's law, an eddy current is induced on the sheet surface placed within coil's magnetic field and repulsive forces are generated between the coil and the sheet. The Lorentz force is able to quickly deform the workpiece, sticking it to the die placed below. The working coil moves to predefined positions and the sheet deforms in many cycles of charging and discharging (Figure 4.2).
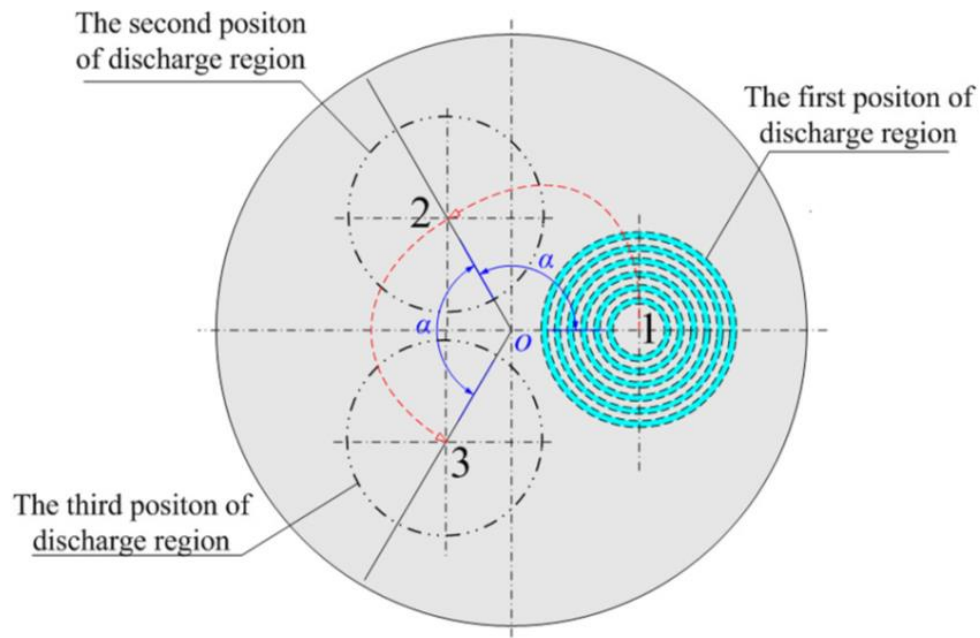
Figure 4.2 *Coil discharge position on the workpiece in EMIF process (Source [95]).*

Once the EMIF process was introduced a as new sheet metal forming process, a few researchers started to investigate about the potential of this Incremental Forming process.

Tan et al. [97] studied the effects of forming parameters, including discharge voltage, capacitance, ratio of rib-height to web-thickness, discharge path, and overlap rate of the coil, on the die-fittingness. The obtained results proved that an incremental voltage with a lower initial one is helpful to improve the die-fittingness, then avoiding the collision rebound of the workpiece against the die.

Li et al. [98] investigated on the mechanism of defect formation, then predicting whether wrinkling occurs or not. Moreover, a relation between parameters and the forming defects was defined. The carried-out analysis showed how defect formation, e.g., wrinkling, is attributed to the circumferential compressive stress induced by the propagation of stress wave driven by discharging. Other defects, similar to humps and depressions, are due to the propagation of stress wave and the interruption of the previously formed structures.

The experimental results provided by *Guo et al.* [99] proved the feasibility of EMIF for 2A12-T4 aluminium alloy panel manufacturing. However, this technique needs to be coupled with a suitable loading path, capacitance, discharge voltage and a correct position distance.
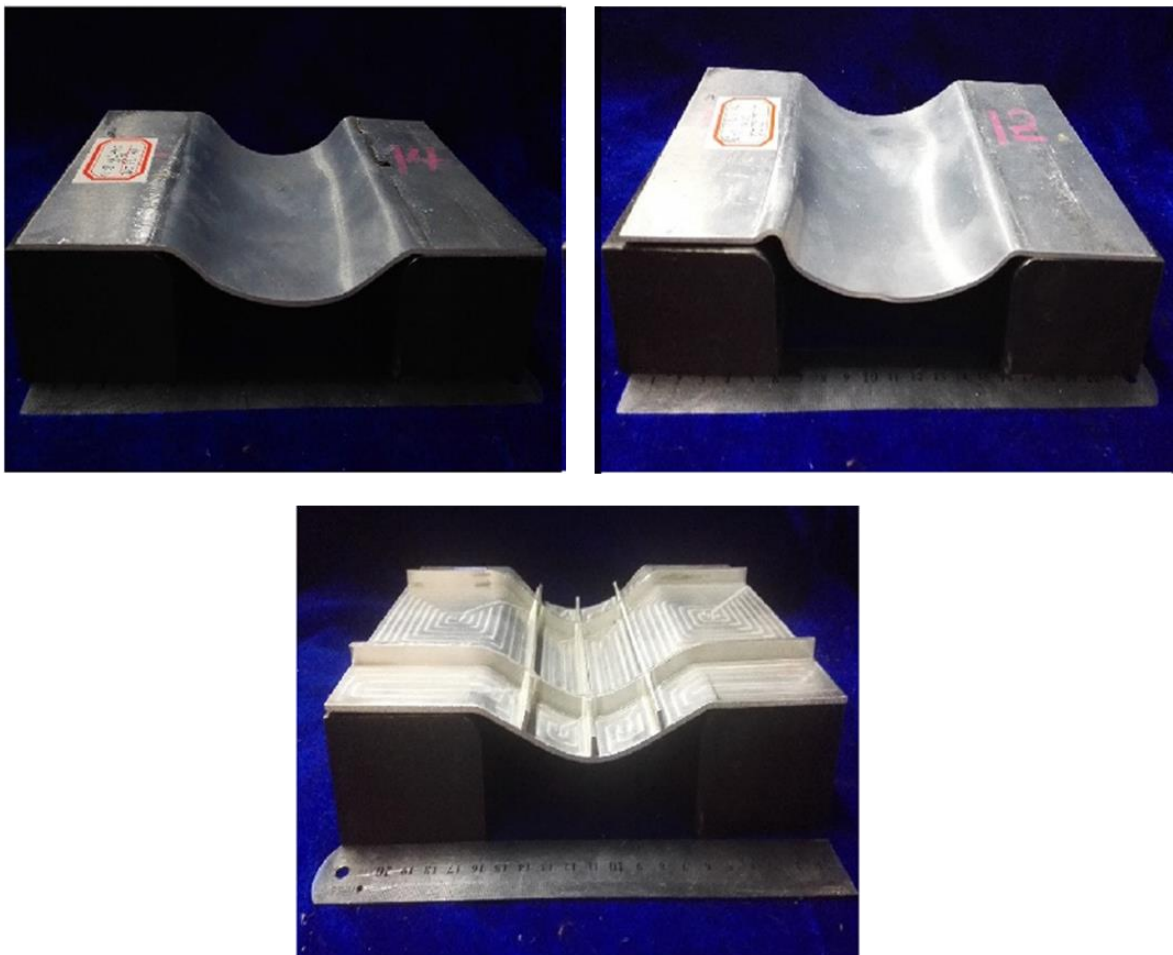
Figure 4.3 Examples of aluminium panels manufactured by EMIF (Source [99]).

Although EMIF allows to improve the sheet formability thanks to high-rate deformations steps, this kind of process shows some drawbacks limiting its application fields:

- It is difficult to manage the magnitude of deformation imposed to the workpiece an its direction using conventional techniques of electromagnetic forming, which requires the presence of a die in order to obtain the required shape.

- Process flexibility is limited by the design of the corresponding coil system according to the specific forming requirements. Additionally, high temperatures in the coil system caused by the large current represent an issue to be considered [100]. Moreover, the final shape complexity is limited by the die adoption.

- Because of substantial rate of deformation, the 'Rebound effect' takes place, *i.e.*, when a high air pressure is created between the workpiece and the die during the forming process causing the appearance of concave surfaces on the sheet. This phenomenon is promoted by the discharge voltage value when exceeds a critical value.

- Just a small part of discharge energy is converted in deformation energy: the losses in heating of the coil and metal sheet are relevant in this low-efficiency process.

Up until today, electromagnetic forming has been used to avoid any type of contact between tool and workpiece, in order to enhance the deformation rate, hence the material formability as stated by *Psyk et al.* [101]. A different approach could be adopted considering the forming action of a small-size tool, controlled using magnetic force. In this way, the process can be traced back as variant of traditional SPIF, in which the tool, suspended by a magnetic field, can locally deform the sheet-metal workpiece. The name attributed to this SPIF variant is *Magnetic Field-Assisted* SPIF (M-SPIF).

As a direct consequence, the proposed solution leads to a series of advantages:

- It guarantees a better deformation control in terms of direction and intensity.

- The tool forming action is instantly localized in small areas: this incremental forming approach allows to overcome traditional forming limits [102].

- An incremental forming method is useful in order to obtain complex shapes and small corner radii.

- In conventional SPIF processes, a tool support is strictly required to define the pin motion. In this proposed forming process, the tool support is represented by a primary magnet placed below the sheet: that means the tool encumbrance is dramatically reduced, thus the deformation of the workpiece along several directions whilst avoiding undercut problems can be achieved [103].

4.2. M-SPIF processing principle

Figure 4.4 shows the processing principle of *Magnetic Field-Assisted* SPIF (M-SPIF). The workpiece is firmly clamped in a blank holder, and a tool is placed over the workpiece. The tool ball can be either a ferromagnetic object or a magnet itself. The magnetic force acting on the tool is defined by the following equation:

$$F = V\chi H \cdot \nabla H \tag{1}$$

where V represents the tool volume, χ is the magnetic susceptibility, and H is the magnetic field intensity.
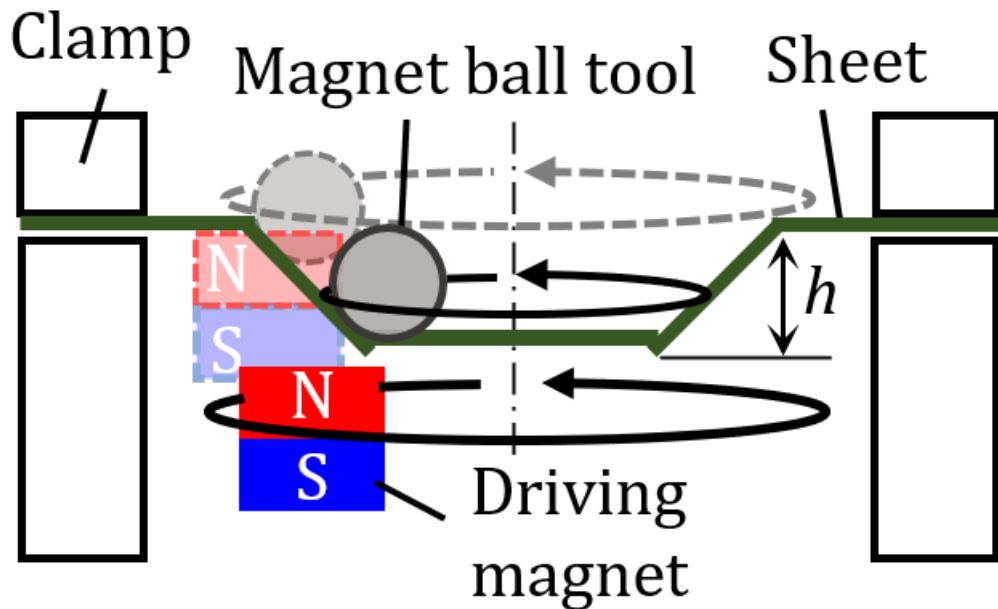
Figure 4.4 M-SPIF processing principle.

Initially, the tool ball tool is attracted toward the centre of the driving magnet ($\theta=0°$, $x=0$) and is suspended by magnetic force F to press the sheet (Figure 4.5). When the driving magnet sufficiently nears the magnet tool, the magnet tool is attracted to the driving magnet. Once the driving magnet moves, the magnet tool follows the driving magnet and deforms the sheet by creating a step. The magnetic force, gravitational force, and centrifugal force acting on the magnet tool combine to create the forming force. The magnetic force is the dominant component because it is three orders of magnitude greater than the others. This

enables flexible tool motion in M-SPIF, which facilitates the creation of complex geometries and forming of areas hard to reach by traditional SPIF (e.g., undercuts).
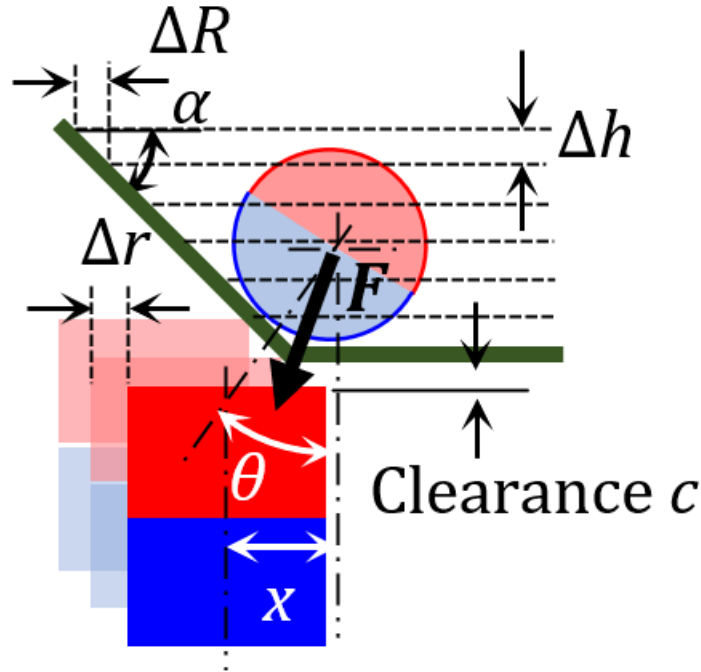
Figure 4.5 *Tool ball and primary magnet relative position.*

Once a wall with angle α is formed (Figure 4.5), the wall prevents the magnet tool from achieving a position corresponding to the magnet centre (the original position). Instead, the magnet tool remains suspended in the magnetic field and continually deforms the sheet. This increases both θ and x with progressive steps.

Replacing the steel ball tool with a magnet ball tool increases the magnetic force by changing $\chi H \cdot \nabla H$ in Eq. [1]. Moreover, because of the polarity of the magnet tool, the dominant component of the magnetic force is directed toward the driving magnet. When forming a truncated cone, the driving magnet follows a circular path, and the direction of the dominant forming force therefore constantly changes. The parameters determining the driving magnet motion (Δ_z, Δr, and feed rate) and the magnetic force on the tool are the primary independent parameters in M-SPIF. The tool motion is a dependent parameter. In contrast, the tool motion in traditional SPIF is an independent parameter, and the forming force is a dependent parameter.

4.3. M-SPIF process feasibility

4.3.1. Development of M-SPIF setup

A preliminary experimental campaign was carried out to determine an M-SPIF process setup allowing to deform a sheet metal workpiece. To do so, a 0.5 mm thick AA1100 aluminium sheet was used as the workpiece. A combination of a 52100-steel ball as a tool and Nd-Fe-B permanent magnet as a field generator was chosen to generate sufficient magnetic force to deform the aluminium sheet. The appropriate combination of tool and magnet was selected based on a series of finite-element magnetic-field analyses performed using the commercial software FEMM® with various conditions, including magnet material and size, tool material and size, clearance between the magnet and tool, etc.
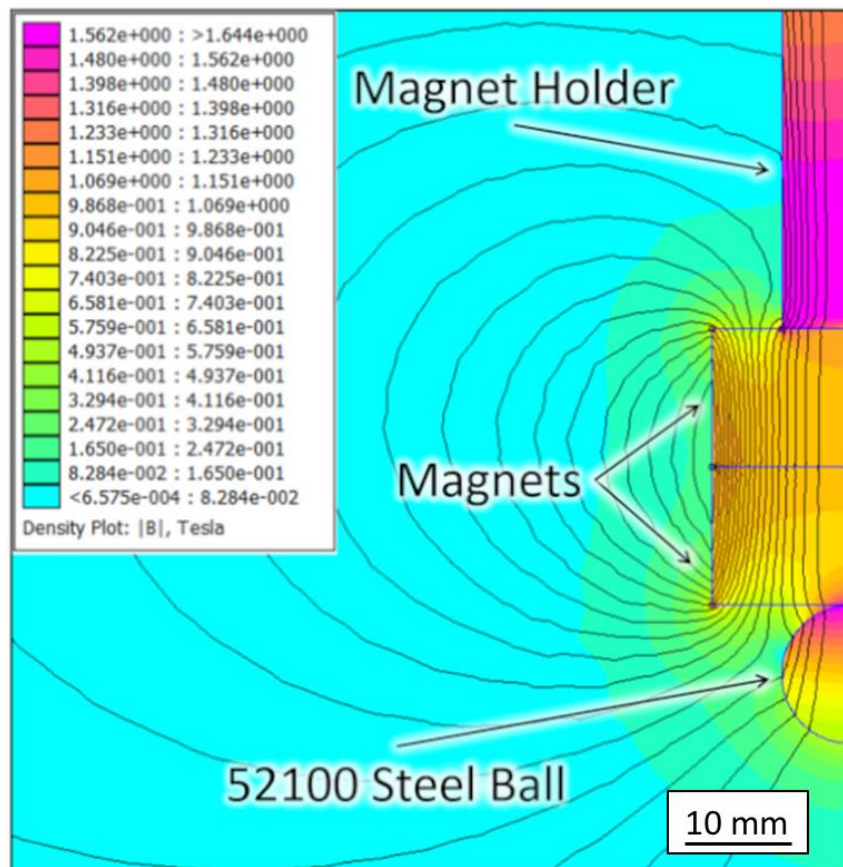
Figure 4.6 *Finite-element magnetic-field analysis of the adopted magnet configuration (⌀25.4×12.7 mm Nd-Fe-B magnet; ⌀12.7 mm 52100 steel ball; ⌀12.7×66 mm magnet holder).*

Figure 4.6 shows a representative result of the magnetic field analysis. A 12.7 mm diameter 52100 steel-ball tool is placed below the 0.5 mm thick AA1100 workpiece. A magnetic-field generator consisting of two Nd-Fe-B magnets ($\varnothing 25.4 \times 12.7$ mm) was attached to a magnet holder ($\varnothing 12.7 \times 66$ mm) and placed above the workpiece with a 0.5 mm clearance. About 1 T is obtained at the tool–workpiece contact point.
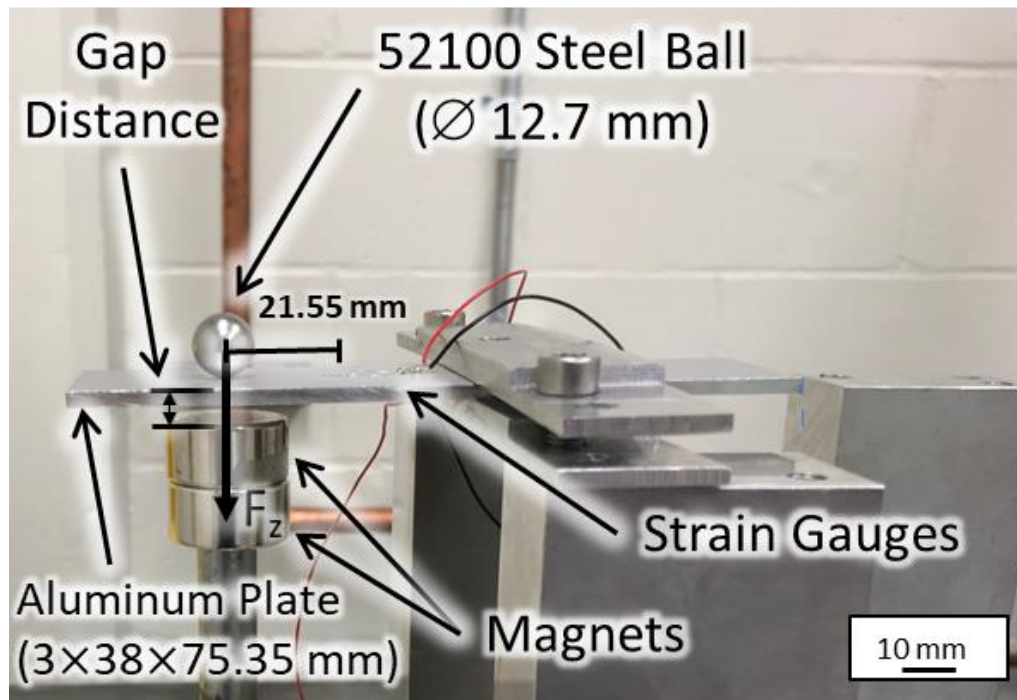
Figure 4.7 *Magnetic force measurement setup.*

Figure 4.8 shows changes in magnetic force acting on the tool (the vertical load pressing the workpiece) with the gap distance between the magnet and the ball tool. The sum of the workpiece thickness (0.5 mm) and the clearance between the magnet and workpiece (0.5 mm) result in a gap distance of 1.0 mm, and the estimated magnetic force at that gap distance is 25.8 N. When the tool was dragged by the magnet under these conditions, the tool left a 580 µm wide groove on the workpiece. By estimating the contact area between the tool and workpiece (a 580 µm diameter circle) the contact pressure is calculated to be 97.7 MPa, which is greater than the yield strength of AA1100 (25 MPa). Accordingly, this condition can be potentially used to achieve a successful M-SPIF process.
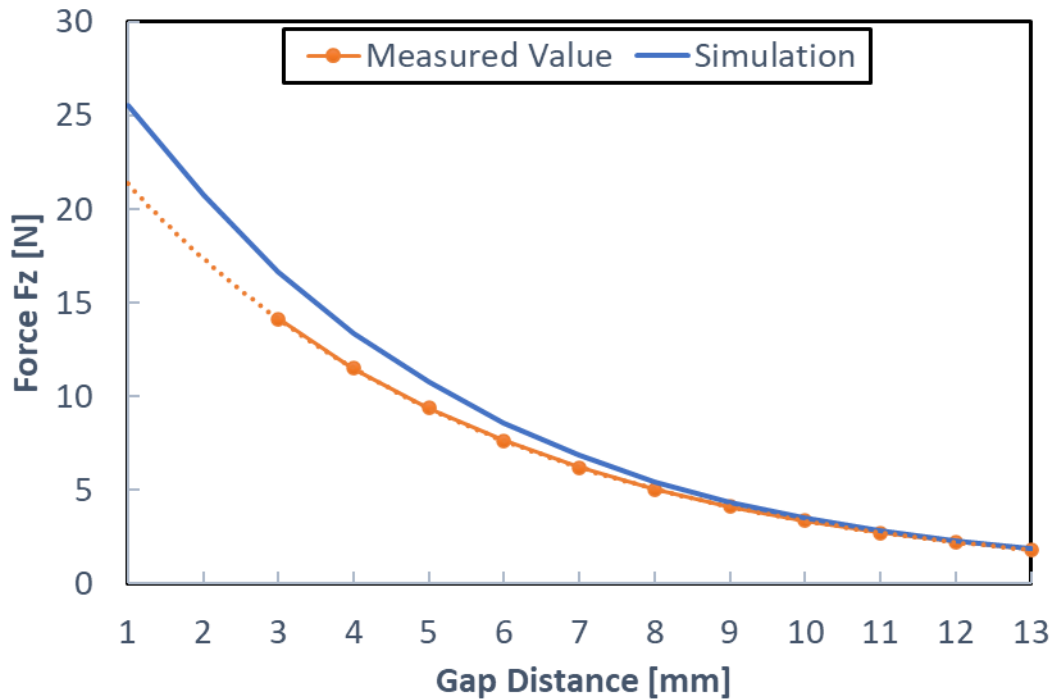
Figure 4.8 Changes in magnetic force with gap distance.

To validate the simulation, the magnetic force acting on the tool was actually measured using the setup shown in Figure 4.7. The tool and magnet properties match those defined in the simulation of Figure 4.6. Due to the beam thickness, the magnetic force was measured at a gap distance down to 3 mm, while values at lower gap distances were estimated based on the recorded exponential trend for higher distances (dotted line in Figure 4.8). Figure 4.8 shows both measured and simulated values. A slight difference in force values between measurements and simulation at lower gap distances is observed, which can be attributed to the different acquisition method. The numerical simulation produced values at a node at the very bottom of tool ball (the closest point to the top surface of the workpiece) which represents only the hypothetical centre point of the tool/workpiece contact area with the highest magnetic force. In contrast, the measured force values are the result of a distributed pressure applied by the ball within the contact area. Accordingly, the difference between these two sets of values was considered to be acceptable, and the simulation values can be used as an estimate of the magnetic force acting on the tool when the further modification in the experimental setup is needed. At a gap distance of 1 mm, the actual magnetic force acting on the tool was estimated to be 21 N, which led to a pressure of 79.5 MPa. The adopted magnet configuration was used to perform a forming test in order to verify the feasibility of Magnetic Field-Assisted SPIF.

4.3.2. Experimental setup

Figure 4.9 shows the experimental setup prepared for the forming experiments at NTML laboratory of University of Florida (United States of America). As stated above, Magnetic Field-Assisted SPIF was proposed to create complex geometry in any direction using a magnetic ball, as a tool, suspended in a magnetic field. A first step to proving this concept was the set of experiments designed to create convex geometry on an aluminium workpiece using a ball magnetically manipulated using a permanent magnet attached to a six-axis robot (shown in Figure 4.9). Magnets were placed above the workpiece, and the 52100 steel ball tool was suspended by magnetic force. The magnetic force causes the ball to follow the magnet movement while simultaneously pressing the sheet. If the magnetic field were not applied to the tool, the tool would simply fall due to the gravitational force, and the process would fail.

The Nd-Fe-B permanent magnets were attached to the steel magnet holder, which was mounted to an end effector of a FANUC LR Mate 200iC 6-Axis robot arm. A 0.5 mm thick AA1100 aluminum alloy sheet was mounted on the blank support, and a working area of 100×100 mm2 was established. A $\varnothing 22.2$ mm 52100 steel ball was used as a forming tool. To form a 10 mm deep truncated cone, a spiral toolpath was made, and the detailed experimental conditions are shown in Table 4.1.

Table 4.1 *Magnetic Field-Assisted SPIF experimental conditions.*

Parameter	Value
Magnet (M)	Nd-Fe-B magnet: $\varnothing 25.4 \times 12.7$ mm
Magnet holder (M_h)	$\varnothing 12.7 \times 66$ mm
Workpiece	AA1100 sheet: $100 \times 100 \times 0.5$ mm
Frustum height (h_f)	10 mm
In-plane step size (Δ_{xy})	0.5 mm/rev
Stepdown (Δ_z)	0.5 mm/rev
Magnetic tool diameter (d_t)	52100 steel ball tool: $\varnothing 22.2$ mm
Cone outer diameter (D)	50 mm
Gap distance	1 mm
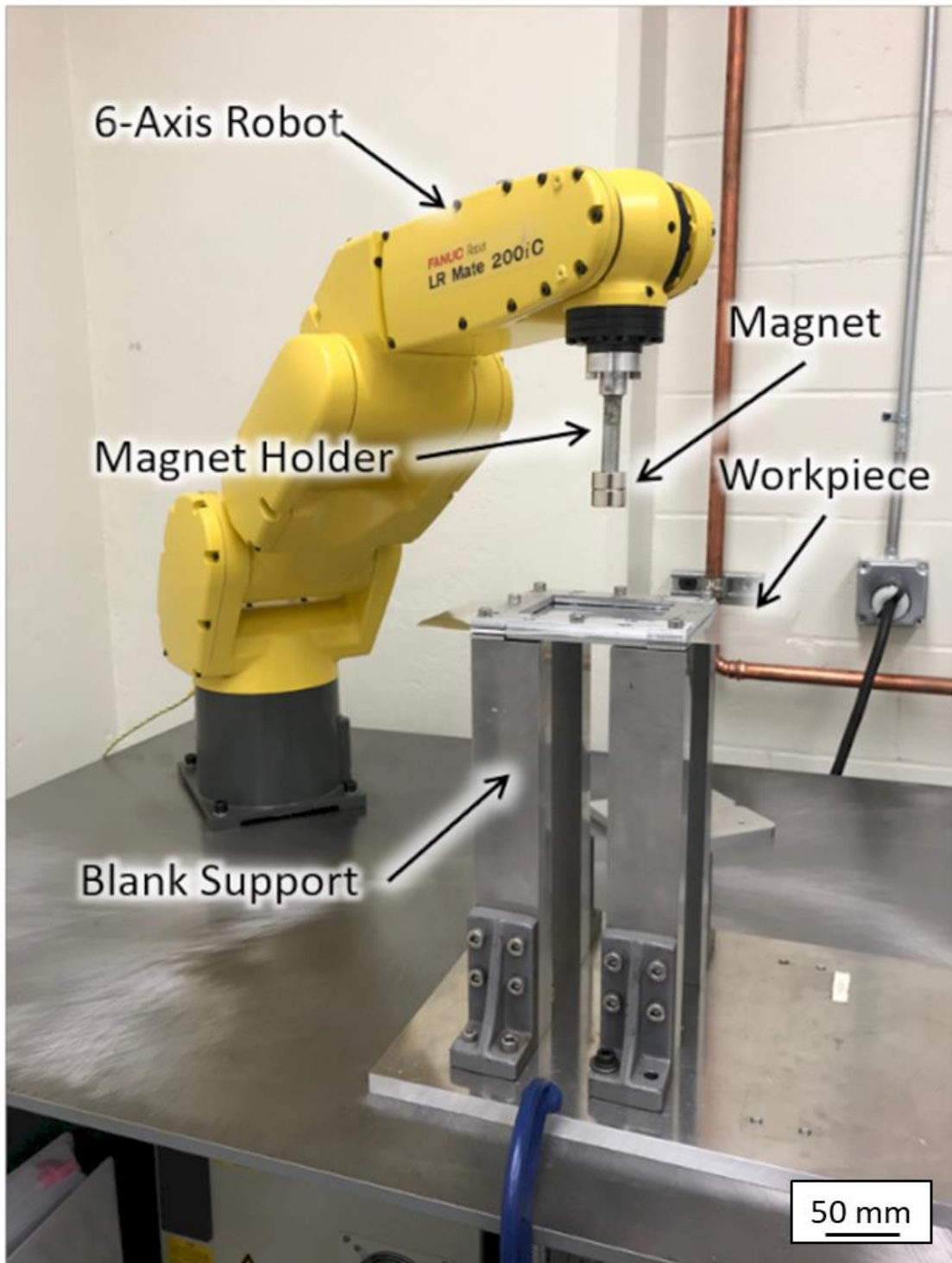
Figure 4.9 Magnetic Field-Assisted SPIF forming machine assembly.

4.3.3. Obtained results discussion

Figure 4.10 shows the deformation results. Although the target truncated cone height was set at 10 mm, a 5 mm high truncated cone was manufactured. This result can be explained by taking into account the relationship between the applied vertical load on workpiece and the material behaviour during the process. A magnetic force of 20-25 N was enough to initiate deformation. The tool plastically deformed the workpiece, thus ensuring the forming process continuity. The aluminium work-hardening phenomenon intensified as the process progressed, so that the load required to further deform the workpiece increased. When the applied vertical load on the sheet was not great enough to counteract the workpiece material work-hardening, the tool followed the magnet movement and moved relative to the workpiece but stopped plastically deforming the workpiece.
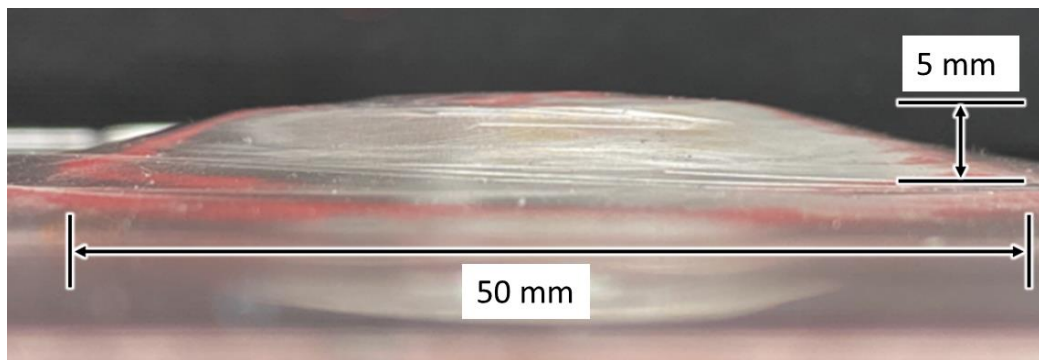
Figure 4.10 Deformation results for M-SPIF testing on Al 1100 sheet.

Figure 4.11 Changes in magnetic force with gap distance under conditions shown in Table 4.1.

Figure 4.11 shows the simulated load trend for the adopted magnet configuration. As discussed previously, the actual force value acting on the tool can be slightly lower than that value. Therefore, the gap distance threshold value of 4-5 mm was considered to correspond

to the vertical load necessary to plastically deform the workpiece (20-25 N). Once the work-hardening phenomenon intensified, the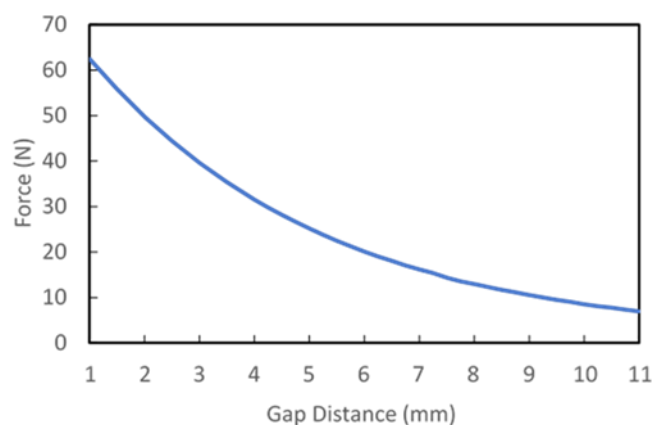 gap distance had to be reduced to ensure the higher magnetic force needed for continual deformation of the workpiece. However, regardless of the tool motion, the magnet kept moving according to the program for the 10 mm high truncated cone under the conditions used in the experiments. As a result, the gap distance between magnetic tool and permanent magnet increased, leading to the drop in magnetic force followed by plastic-deformation failure. At the end of the process, the actual gap distance was estimated to be 7 mm. According to Figure 6, the tool at a gap distance of 7 mm cannot generate magnetic force needed to deform the workpiece, which had been work-hardened during the process.

In addition to the obtained height being lower than the target height, the truncated cone manufactured by Magnetic Field-Assisted SPIF had a lower wall angle than desired. This can be attributed again to an insufficient vertical load compared to the workpiece work-hardening in the wall zone.

4.3.4. Final considerations

To summarize, an innovative Magnetic Field-Assisted SPIF principle was proposed to overcome limitations of traditional SPIF, such as a limited wall angle and the inability to produce undercut geometry. The performed experiments demonstrated the feasibility of the proposed concept by manufacturing a 5 mm deep truncated cone with the wall angle of 15° on an AA1100 aluminium sheet.

The obtained wall angle and cone height were different from the designed values. These results were due to the limitations of the adopted setup, such as the magnetic force acting on the tool, but the conditions can be adjusted by modifying the magnet configuration and gap between the tool and magnet. Unlike traditional SPIF, in which the workpiece is deformed by copying the tool motion, Magnetic Field-Assisted SPIF results in a deformation by copying instead the tool pressure.

For a better process understanding, as well as to obtain more considerable results in terms of material deformation, the controllability of tool motion and the relationship between the tool motion and the resulting sheet deformability have been further studied in detail by performing a new experimental campaign.

4.4. M-SPIF process analysis

4.4.1. Experimental Protocol

A ∅12.7 mm Nd-Fe-B magnet ball tool was placed with lubricant on a 0.175 mm-thick AA1060 sheet. A ∅12.7×12.7 mm Nd-Fe-B (N42) magnet was placed on two ∅25.4×12.7 mm Nd-Fe-B (N42) magnets, and the combination was attached to a 6-axis robot arm. The set of magnets was positioned under the sheet with a clearance c (see Figure 4.5). The magnetic force acting on the tool ranged between 24.0 N (c=3 mm) and 38.7 N (c=0 mm). The initial circular path radius of the driving magnet was 20 mm. The magnets were fed along that path to drag the tool until deformation of the sheet eliminated the clearance c. When the clearance was eliminated in each step, the magnet was removed from the processing area to allow the deformed sheet to spring back. After each step, the magnet was moved—inward horizontally by Δr and vertically such that the designated clearance was restored—and the process was repeated until the magnet path radius reached 12 mm. Other conditions are shown in Table 4.2.

Table 4.2 Experimental conditions.

Driving magnet	Nd-Fe-B magnet (N42), ∅25.4×12.7 mm (×2), ∅12.7×12.7 mm (×1)
Tool	∅12.7 mm Nd-Fe-B magnet ball
Workpiece	0.175 mm-thick AA1060 aluminum sheet
Working area	100×100 mm²
Magnet feed rate	100 mm/s
Decrement Δr	0.25, 0.5 mm
Clearance c	2, 3 mm
Lubricant	Oil (WD-40)

The changes in height of the truncated cone Δh were tracked at each step. The total height h of the truncated cone was determined by adding the individual height changes. In addition, the inner diameter (*ID*) of the truncated cone was measured at each step using images taken from above. The radius decrement of the truncated cone ΔR was calculated as half the change in *ID*. After all measurements were completed, the next step was begun.

4.4.2. Forming characteristics in M-SPIF

Figure 4.12a shows the numbers of tool (driving magnet) revolutions required to eliminate the clearance for three cases: (i) $c = 2$ mm and $\Delta r = 0.25$ mm, (ii) $c = 2$ mm and $\Delta r = 0.5$ mm, and (iii) $c = 3$ mm and $\Delta r = 0.5$ mm. The figure also shows the changes in the truncated-cone height per step Δh (4.11b), the calculated Δh per tool revolution (4.11c), and total height h with driving magnet movement (4.11d). In all cases, the change in height Δh per tool revolution decayed exponentially as the driving magnet moved inward; therefore, the vertical movement step decreased due to the work hardening of the sheet.
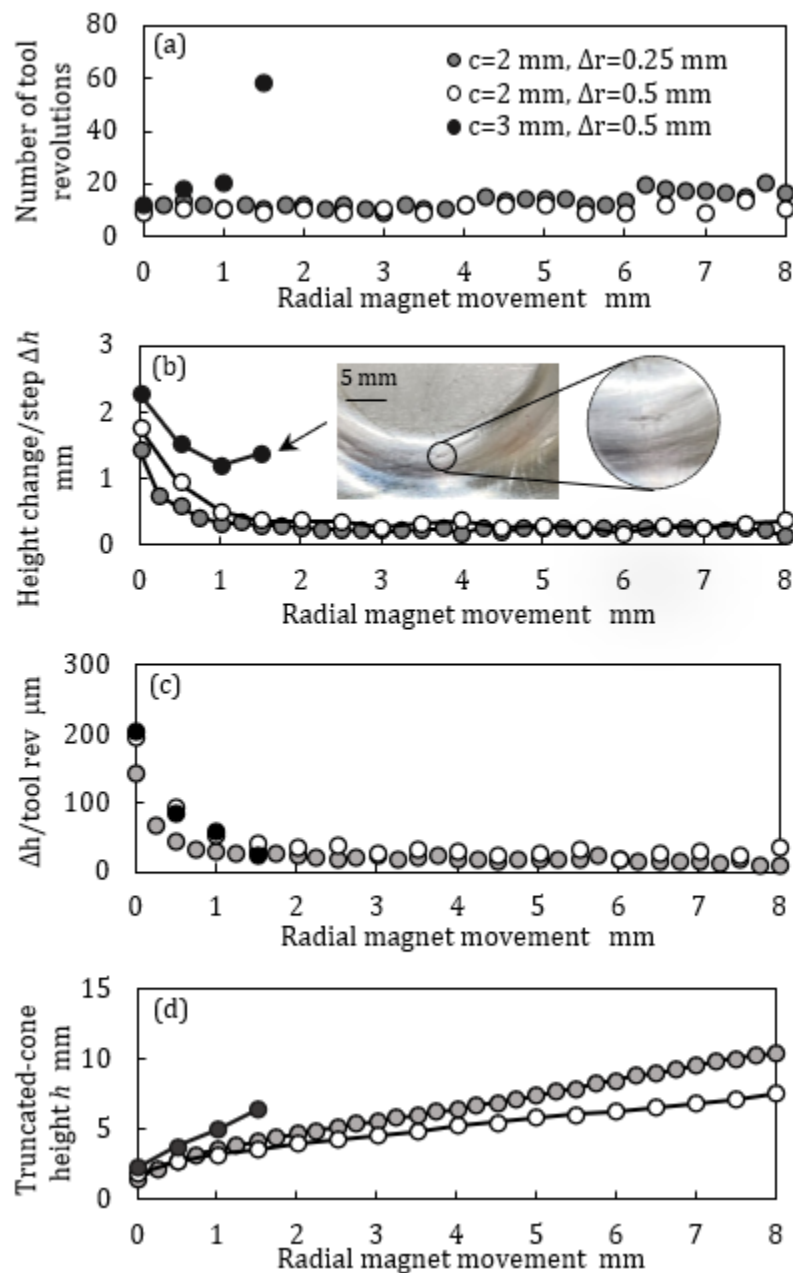

Figure 4.12 *Changes in (a) number of tool revolutions, (b) truncated-cone height change/step Δh, (c) truncated-cone height Δh/tool rev, and (d) total truncated-cone height h with radial magnet movement.*

The thin sheet was easily deformed. Therefore, despite the additional 1 mm clearance in Case (iii), the tool was instantaneously attracted by the driving magnet and able to deform the sheet. After the deformation, the clearance decreased as the number of tool revolutions increased. The resultant height change Δh in the first step (11 revolutions) in Case (iii) was 2.76 mm. This large Δh accelerated local stress concentrations. The sheet, which had experienced severe work-hardening in the first step, was not as deformable in subsequent steps as it was initially. Accordingly, Case (iii), which had a clearance of 3 mm, required more revolutions to complete each step than the other cases. Large height changes of the truncated cone in every step resulted in the circumferential cracks (shown in Figure 4.12b)) encountered during the fourth step in Case (iii).

In Cases (i) and (ii), after the large initial deformation, changes in the truncated-cone height Δh per tool revolution gradually decreased, and resultant truncated-cone heights gradually increased. When the total driving magnet movement (the accumulation of the individual Δr from each step) reached 8 mm, the final truncated-cone heights, before removing the sheets from the holder, were 10.4 mm (after 33 steps, 427 revolutions) in Case (i) and 7.53 mm (after 17 steps, 169 revolutions) in Case (ii), as shown in Figure 4.13 Case (i) had a wall angle greater than Case (ii): 38.3˚ and 27.4˚, respectively.
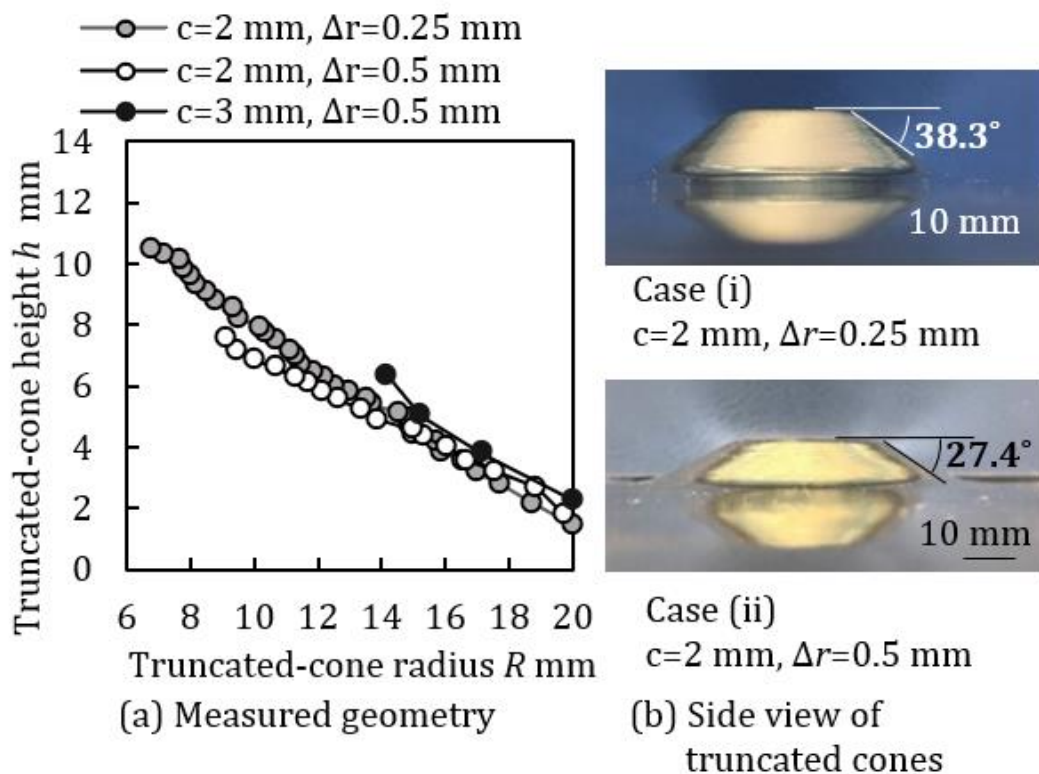
Figure 4.13 Truncated cones manufactured by M-SPIF.

Figure 4.14 shows the relationships between the decrement of the truncated-cone radius, the calculated angle θ and distance x, and the magnet movement in Figure 4.5. Since the steps were shorter in Case (i) (Δr of 0.25 mm) compared to Case (ii), which had a Δr of 0.5 mm, more overlap between new and previous tool paths was encountered in Case (i) than in Case (ii). Unless the magnetic force on the tool exceeded the force needed to deform the work-hardened section, the tool tended to deform only the undeformed area, increasing the truncated-cone height. This also increased the distance x and angle θ with the radial magnet movement with each step (see Figure 4.15). The direction of the magnetic force gradually points more outward as the M-SPIF process progresses. In contrast, the resultant forming force in traditional SPIF is consistently directed downwards (perpendicular to the sheet surface).
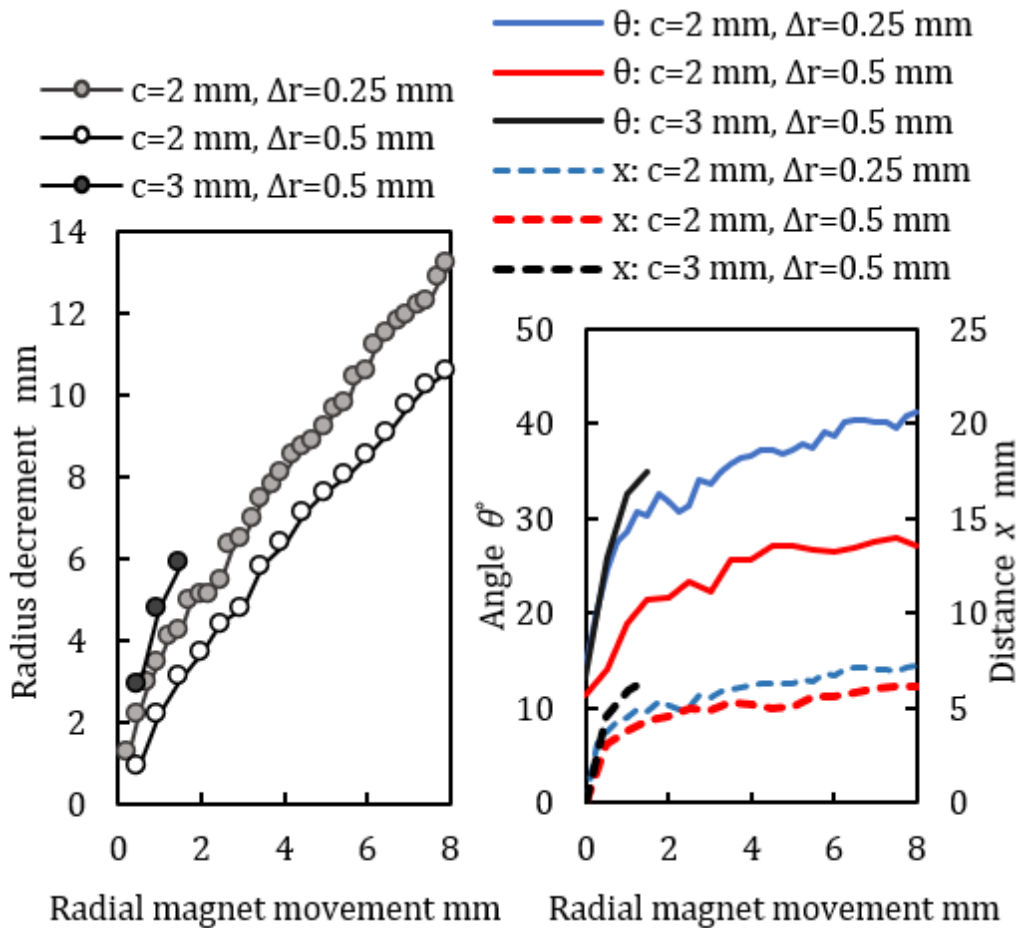
Figure 4.14 *Changes in radius decrement of truncated cone and angle ϑ and distance x (Fig. 4.5) with radial magnet movement.*

The distance x in Case (i) was greater than that in Case (ii). Increasing the distance x decreases the magnetic force on the tool. Compared to Case (ii), the work-hardening effects and lower magnetic force required the increased number of tool revolutions per step in Case (i). However, the greater number of steps in this case resulted in greater changes in total height and total radius decrement of the truncated cone.
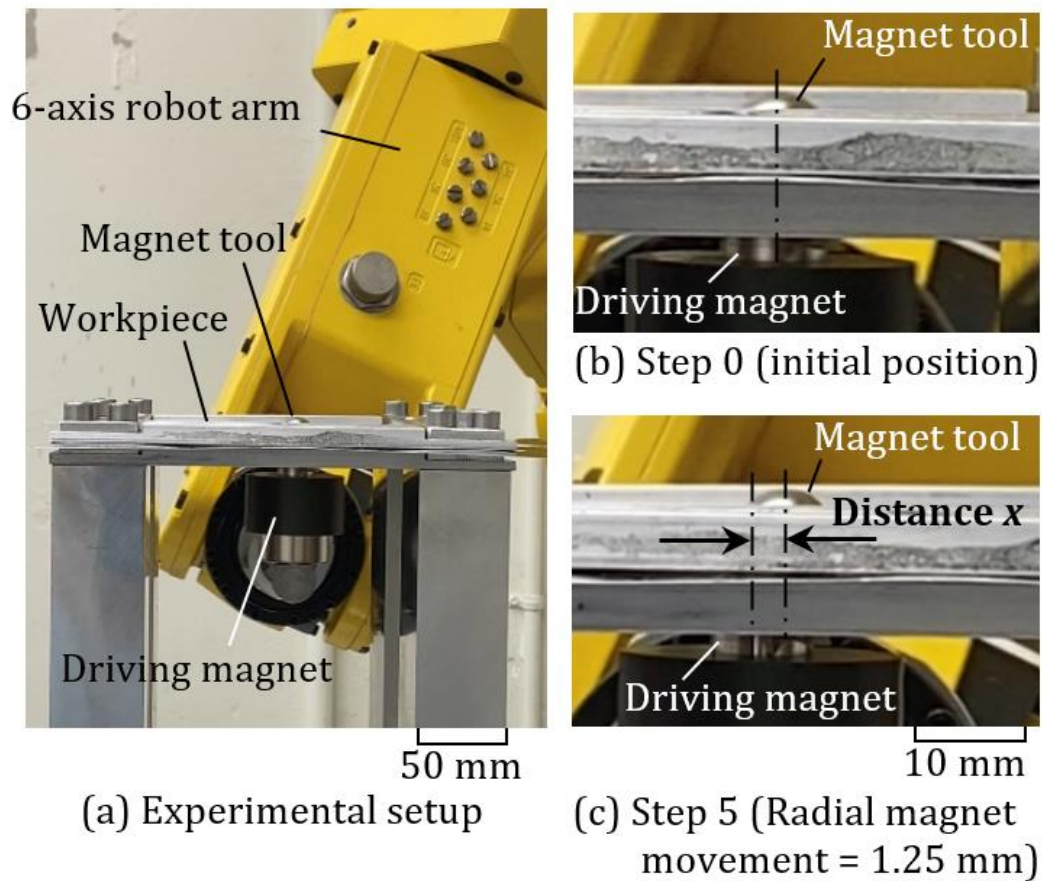
Figure 4.15 Representative tool and driving magnet positions in Case (i).

4.5. Comparison between traditional SPIF and M-SPIF

Numerical simulations were performed using commercial finite-element-analysis software (ABAQUS/Explicit®) to determine the processing parameters for traditional SPIF that replicates the truncated cone made using M-SPIF. S4R shell elements 0.175 mm-thick (5 integration points through the thickness, mesh size=1.25 mm) were used for the workpiece. The tool was considered to be a rigid body, and the friction coefficient between the tool and workpiece was set to 0.05. The material elastic behaviour was modelled with a Young's modulus E=68.9GPa and a Poisson's ratio v=0.33. The plastic behaviour was defined according to Hollomon's law with appropriate coefficients: $\sigma = 164.2\varepsilon^{0.23}$ MPa.

The simulations also allowed the mechanics of both M-SPIF and traditional SPIF to be analysed. The numerical model of M-SPIF was developed based on the magnet-tool movement as a function of time recorded during the experiments, which were set as boundary conditions for the tool in the simulation.

The processing parameters of traditional SPIF, obtained by numerical simulations, were used to manufacture a truncated cone replicating the one obtained in Case (i) with M-SPIF. In the experiments, a $\varnothing$12.7 mm 52100 steel ball tool was attached to the robot arm. The initial tool path radius was set at 20 mm. The tool step-down (change in the vertical direction) and step-in (change in the horizontal direction) in traditional SPIF were set to 0.25 mm and 0.30 mm, respectively. The tool was fed in a spiral motion at 100 mm/s. When the total tool step-down and step-in reached 10.25 mm and 12.30 mm, the experiment was stopped.
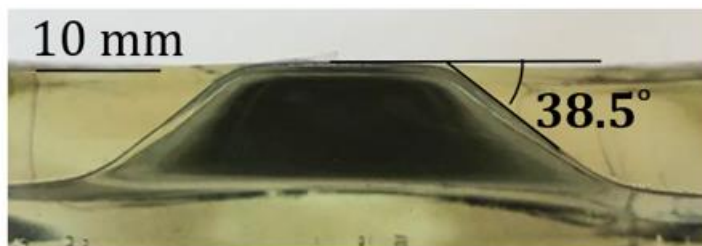
Figure 4.16 Cross-section view of truncated cones.

Figure 4.16 shows the cross-section view of truncated cone replicating M-SPIF Case (i) with traditional SPIF. Measurements of the truncated-cone wall angle was 38.3˚, which was similar to those in M-SPIF Case (i).

Figure 4.17 shows the thickness of simulated and experimentally obtained truncated cones of both traditional SPIF and M-SPIF. The experimentally obtained values are the averages of five thickness measurements at each point. As shown in Fig. 4.17, a slight thinning of the thickness at the bottom of the truncated cone was observed in the M-SPIF workpiece. In contrast, the wall was slightly thicker around the corner of the truncated cone in M-SPIF. These trends are consistent in both simulations and experiments.
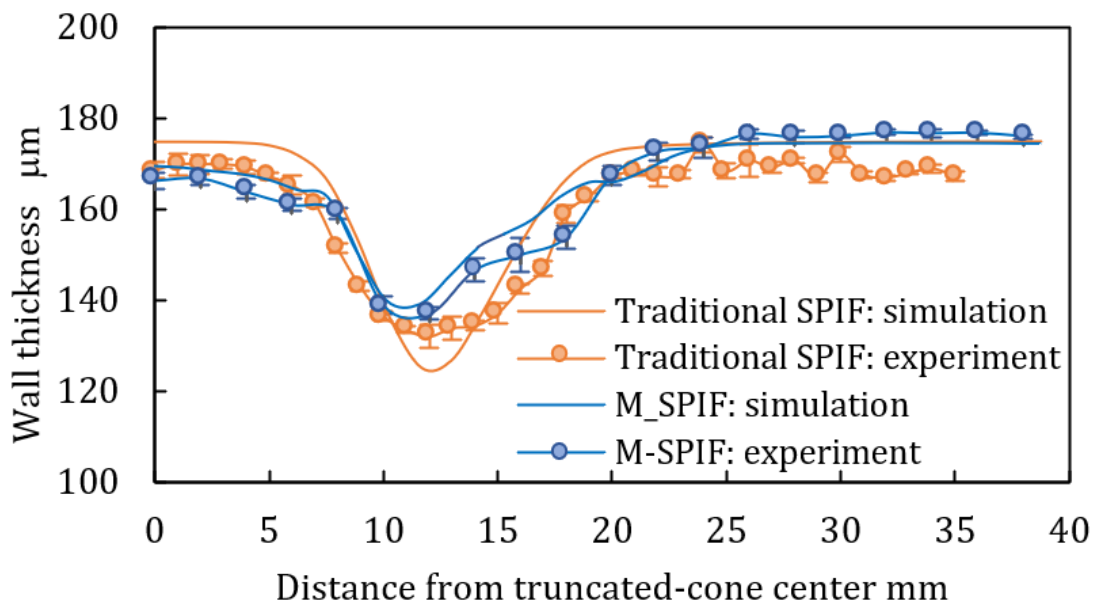
Figure 4.17 *Truncated cones made with traditional SPIF and M-SPIF.*

The major plastic strains (Figure 4.18) of both processes were also analysed to further compare the process mechanics of M-SPIF and traditional SPIF. While the maximum and minimum values are 0.308 and 0.0004 (centre of the truncated cone) in traditional SPIF, they are 0.202 and 0.008 in M-SPIF. The maximum major plastic strain in M-SPIF was lower than that in traditional SPIF. Additionally, a small deformation was found at the bottom (centre) of the truncated-cone in M-SPIF. This is consistent with the results shown in Fig. 4.16. As the M-SPIF process progresses, the magnetic force is gradually directed more outward. As a result, material from the centre of the cone is forced outwards. This stretching causes the increased thinning at the centre of the truncated cone in M-SPIF while the cone centre remains largely undeformed in traditional SPIF. These simulation results suggest

enhanced deformability in M-SPIF compared to traditional SPIF. This can be also attributed to the small tool increments as the tool is driven by magnetic force.

(i) Traditional SPIF   (ii) M-SPIF

(a) Contour plot of major plastic strain

(b) Major plastic strain distribution
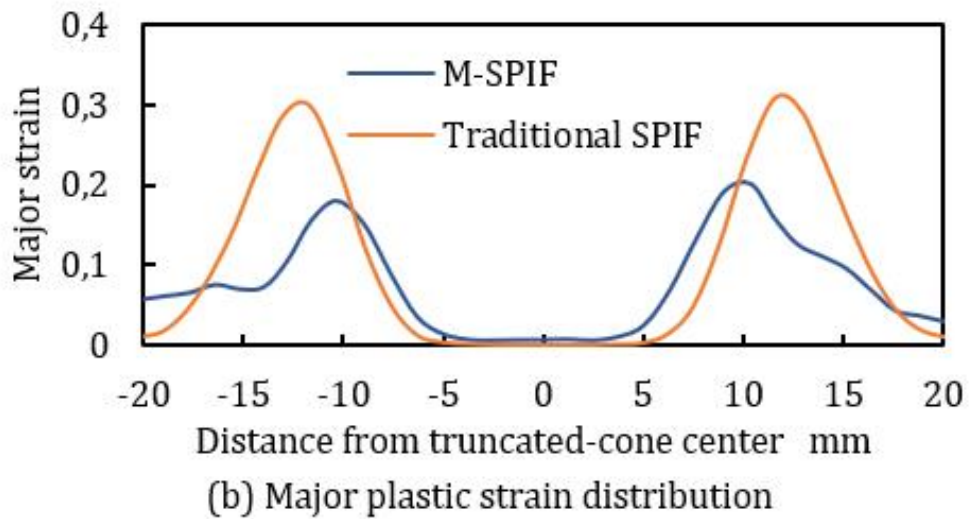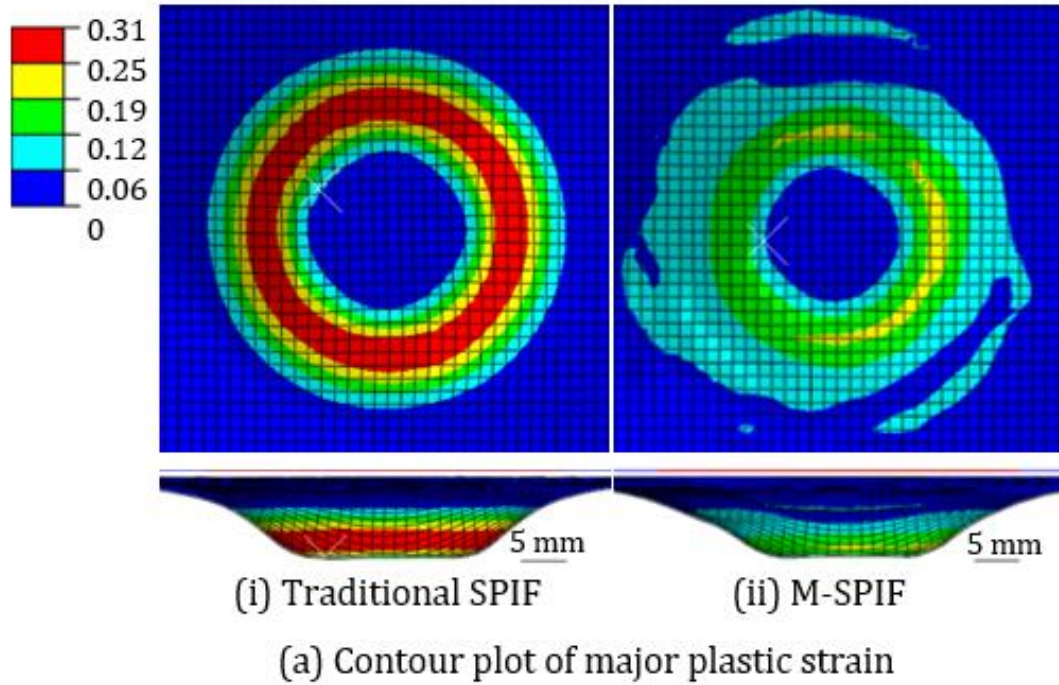
Figure 4.18 *Simulated major plastic strain distribution.*

From the performed comparison, it can be stated that while the dominant component of the forming force in traditional SPIF is constantly directed perpendicular to the workpiece surface, the dominant component of the forming force in M-SPIF is directed toward the driving magnet (on the opposite side of the sheet), and the direction continually changes during forming. In this way, the force direction can be controlled to improve strain distribution and formability.

Although the major plastic strain is slightly higher at the centre of the truncated cone in M-SPIF, numerical simulations showed that overall M-SPIF enables forming of a sheet while generating less localized plastic strain than traditional SPIF.

Furthermore, it was found that to obtain a specific wall angle value to be compared with traditional SPIF experimental results in terms of geometrical accuracy, a higher wall angle value has to be set as reference in M-SPIF to take into account the lateral offset occurring between driving magnet and tool ball during the process.

Nevertheless, the mechanics of forming in M-SPIF, including the relationships between tool and driving magnet movements, magnetic force, forming pressure, and resultant stress distribution, need to be clarified to better control the process, thus enabling the full exploitation of the process potential, such as the forming of undercuts.

4.6. M-SPIF numerical simulation: a force-based model

4.6.1. Force-based M-SPIF simulation development

With the aim to develop a numerical model able to represent both strain and section thickness distribution characterizing M-SPIF, a displacement-based numerical simulation was developed, describing the magnet-tool movement as a function of time recorded during the experiments, which were set as boundary conditions for the tool in the simulation.

Nevertheless, such a simulation approach does not really match the real process mechanics consisting in a magnetic force generated via primary magnet, which is placed underneath the workpiece, managing the magnet ball movement on blank top side. To better represent this force-based variant of traditional SPIF within the numerical model, a preliminary numerical simulation adopting VDLOAD user subroutine was developed in Abaqus/Explicit® environment.

Based on previous studies regarding VDLOAD subroutine, which allows to apply both surface loads (FL^{-2}) and body forces (FL^{-3}) as a function of position, time, velocity, etc. for a group of points defining the selected object, a brand-new numerical model with a force-controlled tool motion was set. The idea behind this model was to define each component of the magnetic force acting on tool ball (modelled as a rigid body), which is the responsible of workpiece plastic deformation along its path managed by the primary magnet movement. A 'dummy' primary magnet, modelled as a rigid body as well, was added to the model in order to materially identify the current object position during the ongoing simulation. Model front view is reported in Figure 4.19.
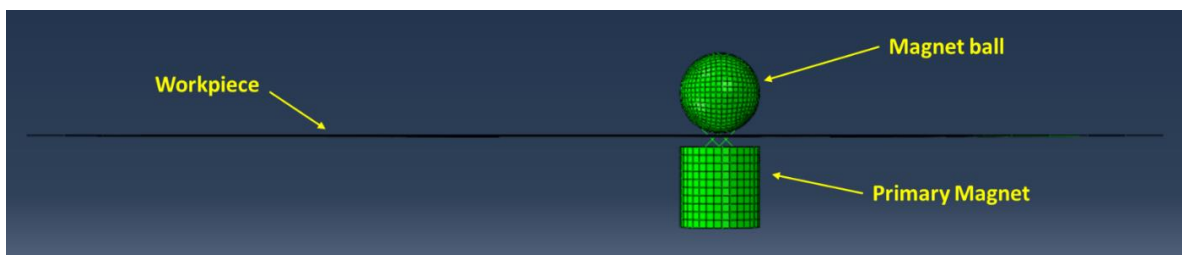


Figure 4.19 Numerical model setup.

The path coordinates related to primary magnet top surface centre were added within the subroutine (namely *x_mag*; *y_mag*; *z_mag*) in order to define the current distance along X, Y and Z axes between the primary magnet and every point being part of tool ball (namely *gap_x*; *gap_y*; *gap_z*). Body force components 'F_x', 'F_y' and 'F_z' simulating the magnetic force acting on tool ball were modelled according to a 'Force mapping' experimental procedure. The adopted setup for this procedure consisted in a $\varnothing12.7$ mm Nd-Fe-B magnet ball tool and a $\varnothing12.7\times12.7$ mm Nd-Fe-B (N42) magnet placed on other two $\varnothing25.4\times12.7$ mm Nd-Fe-B (N42) magnet as primary magnet system. The obtained results allowed to define every force component as function of vertical and in-plane distance between the primary magnet and the tool ball itself. Finally, thanks to a non-linear multiple regression it was possible to define an analytical model for 'F_x', 'F_y' and 'F_z', respectively, then implemented within the subroutine. In this way, at every time-step increment of numerical simulation, force components acting on each tool ball node are updated as a function of the current distance along X, Y and Z axes between the primary magnet and the specific node itself.

Following the already-presented step-by-step protocol in paragraph 4.4 for M-SPIF case (i), a force-based numerical simulation was carried out by setting the primary magnet 2 mm below the workpiece and an initial circular toolpath of 40 mm in diameter was repeated 10 times to deform a 0.175 mm-thick AA1060 sheet. After deformation step, spring-back analysis was carried out to determine the blank's bottom rigid translation upwards and to reset the clearance of 2 mm between the primary magnet and the workpiece bottom before the following forming step, characterized by a smaller toolpath diameter ($\Delta r = 0.25$ mm). To avoid undesired local over-deformations due to the fact that tool ball position at both step beginning and termination is the same for every single forming step, four different starting/ending positions were defined (located at 0, $-\pi/2$, $-\pi$, $\pi/2$) varying at each step.

The obtained depth value at the end of first six simulation steps (forming step + spring-back analysis) was recorded and compared with the experimental results, as reported in Table 4.3. Even though few forming steps were simulated, it can be highlighted the fact that these six simulated steps show a similar trend to experimental cases, as well as a more homogeneous depth values distribution all over workpiece bottom.

				Experimental	**Numerical**	
Phase [rad]	Step #	Toolpath Diameter [mm]	Clearance [mm]	Depth [mm]	Inner diameter depth [mm]	Lowest point depth [mm]
0	0	40	2	**1.437**	**1.36÷1.59**	1.591
−π/2	1	39.5	2	**2.183**	**2.52÷2.74**	2.737
−π	2	39	2	**2.761**	**2.92÷3.64**	3.644
π/2	3	38.5	2	**3.182**	**3.35÷.3.86**	3.863
0	4	38	2	**3.509**	**3.50÷3.94**	3.942
−π/2	5	37.5	2	**3.845**	**3.89÷4.19**	4.185
−π	6	37	2	**4.131**	**4.05÷4.55**	4.548
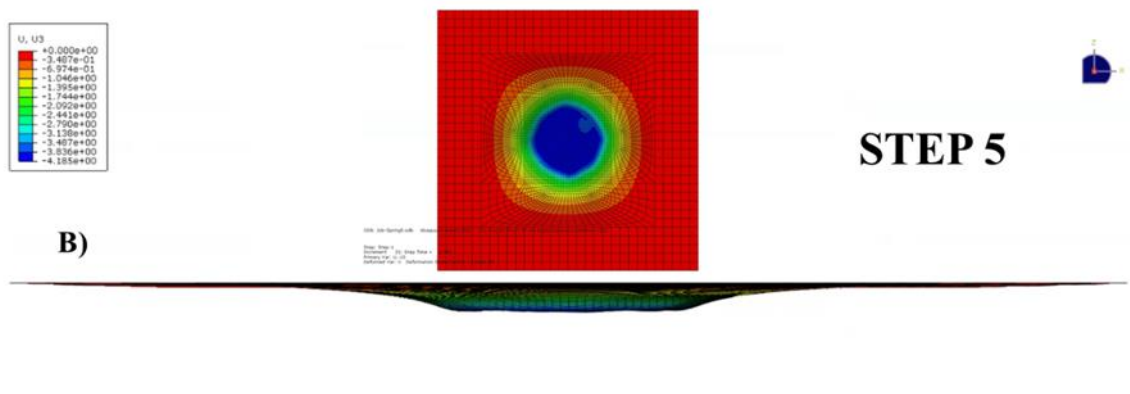
Figure 4.20 *M-SPIF force-based simulation, depth distribution.*

Figure 4.20 shows the force-based M-SPIF simulation results after the 5th forming step. As can be seen, the developed subroutine is able to drive the tool ball along a circular toolpath at each step as a consequence of the magnetic attraction provided by the primary magnet underneath the workpiece. Such a numerical model setting represents the base of M-SPIF process simulation to take into account the real process mechanics characterizing this new SPIF variant.

4.6.2. *Continuous Force-based M-SPIF simulation with feedback control*

A step-by-step procedure is high time-consuming in both experimental and numerical cases. Such an issue, currently affecting the M-SPIF operation, can be overcome by setting a continuous toolpath for the primary magnet. However, the adoption of this kind of option requires a certain groundwork. In fact, depending on the work-hardening onset in the material during the process, the required force to impose further deformations on it increases. This could lead to a gap distance increasing between magnetic tool and permanent magnet, then a drop in magnetic force followed by plastic-deformation failure. To avoid this event, an innovative feedback control implemented within the Abaqus/Explicit® subroutine was developed, which is able to edit the current clearance between tool ball and primary magnet to intensify magnetic force attraction.
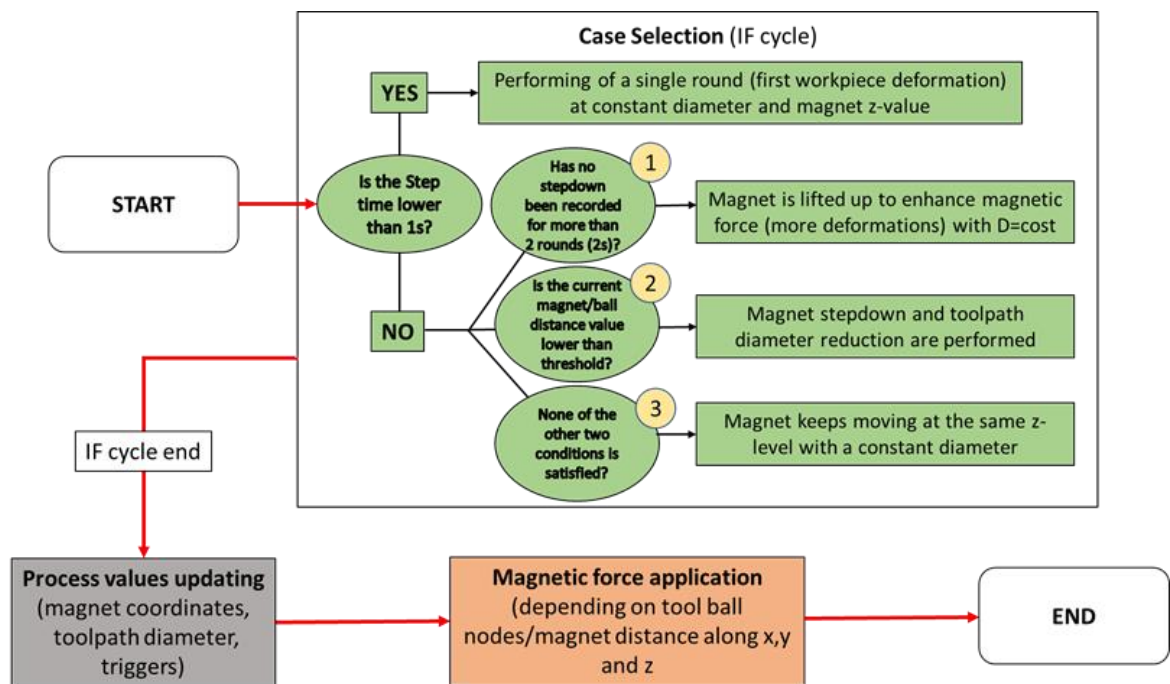
Figure 4.21 M-SPIF user's subroutine with feedback control scheme.

Figure 4.21 shows the current subroutine logic. The specific case selection is managed by a suited 'if cycle' within the VDLOAD subroutine, which is called at every time increment during simulation. For time values lower than 1 second (corresponding to a full round completion), the driving magnet describes a starting circle at fixed z-level to start blank plastic deformation gradually. After the first round, three different scenarios are available (chronologically listed):

1) The primary magnet described more than 2 rounds at the same level → the vertical load is not enough to keep forming the workpiece, the magnet is lifted up to enhance magnetic force.

2) Material is being deformed, the gap distance is closing → if gap distance value is lower than a fixed threshold, both primary magnet z-level and toolpath diameter are decreased according to desired cone wall angle.

3) The gap distance value is higher than threshold, primary magnet described less than 2 rounds at the same z-level → no further modifications are applied, the magnet keeps moving at the same level and toolpath diameter.
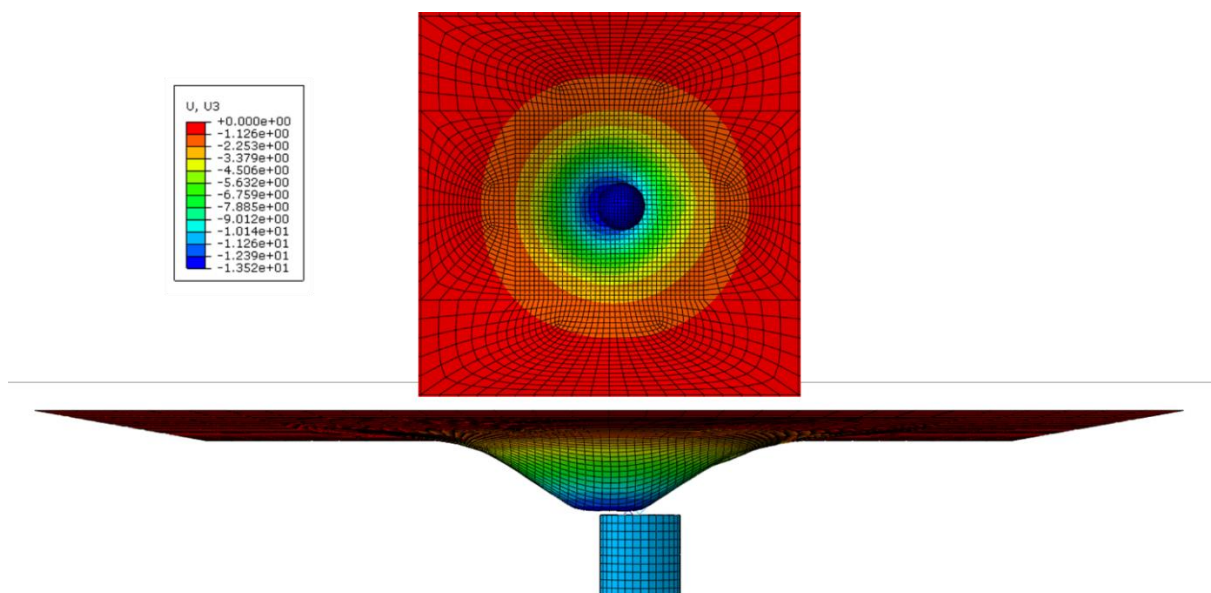
Figure 4.22 *M-SPIF simulation with feedback control, top and front view (displacement values are plotted).*

Once the specific case is selected, all subroutine main variables are updated, such as magnet coordinates, toolpath diameter and, eventually, threshold values. Then the magnetic force is applied on tool ball as a body force depending on the updated distance between itself and the driving magnet. In parallel, driving magnet coordinates are passed to second part of the subroutine managing the displacement of 'dummy' magnet object within the model, which is useful to display the current primary magnet position as well as to define possible contacts with the workpiece bottom above it.

The updated user subroutine was coupled with the already mentioned M-SPIF numerical model, using the same geometrical parameters as well as the same magnetic force model. A regular truncated cone was obtained, proving the effectiveness of the adopted solutions (Figure 4.22).

The presented numerical model, together with a magnetic force characterization for different tool/magnet setups, can represent a reliable predicting tool for M-SPIF process, which can help for a better process understanding in terms of geometrical accuracy of the formed part, stress and strain distribution, and magnet/tool interaction during process. Additionally, the continuous M-SPIF simulation can be used as a reverse engineering method for the development of a suited experimental setup with force feedback control. This can lead to a drastic processing time reduction and a better control of the tool motion over the blank, enabling the adoption of different toolpaths for complex shape manufacturing.

5. Conclusions

5.1. Summary

In this dissertation, the capabilities of the *Multi-Directional Path* SPIF and *Magnetic Field assisted* SPIF processes in lightweight sheet metal processing have been investigated under different aspects. The effectiveness of these peculiar sheet metal forming technologies has been assessed both through experimental campaigns to manufacture different shapes and numerical simulations. Summing up, from the obtained results the following general conclusions can be drawn:

- *Multi-Directional Path* SPIF and M-SPIF processes are two valid options for lightweight sheet metal alloys manufacturing. Their relative setup simplicity, together with the incremental deformation approach can be exploited in industrial applications for mid/small batches production.

- Dedicated numerical model was developed to simulate both *Multi-Directional Path* SPIF and M-SPIF processes, giving insight on the processes mechanics and providing effective tools for products quality prediction.

- In *Multi-Directional Path* SPIF, the material usage from multiple workpiece areas and the optimized bottom part exploitation are the key aspects of this strategy success over conventional multi-Path ones: the section thickness as well as the experimental and numerical strain analysis demonstrate how the full usage of this area, from which conventional strategies allowed to channel just a small amount of material (close to the wall), leads to the manufacture of a sound square cup with vertical walls.

- A new incremental forming process, namely *Magnetic Field-Assisted* SPIF principle was proposed to overcome limitations of traditional SPIF, such as a limited wall angle, vertical and lateral tool encumbrance and the inability to produce undercut geometries. The performed experiments demonstrated the feasibility of the proposed concept by manufacturing a 5 mm deep truncated cone with the wall angle of 15˚. The obtained wall angle and cone height were different from the designed values. These results were due to the limitations of the adopted setup, such as the magnetic force acting on the tool, but the conditions can be adjusted by modifying the magnet configuration and gap between the tool and magnet.

- Unlike traditional SPIF, in which the workpiece is deformed by copying the tool motion, M-SPIF results in a deformation by copying instead the tool pressure.

- By using a different process setup, then enhancing the magnetic force acting on tool ball, a regular truncated cone 12.3 mm in depth and a wall angle value of 38.5° was obtained by M-SPIF operation. From a direct process analysis, it was observed how the direction of the magnetic force gradually points more outward as the M-SPIF process progresses. In contrast, the resultant forming force in traditional SPIF is consistently directed downwards (perpendicular to the sheet surface).

- From the performed comparison between components made by traditional SPIF and M-SPIF, it can be stated that while the dominant component of the forming force in traditional SPIF is constantly directed perpendicular to the workpiece surface, the dominant component of the forming force in M-SPIF is directed toward the driving magnet (on the opposite side of the sheet), and the direction continually changes during forming. In this way, the force direction can be controlled to improve strain distribution and formability.

- Although the major plastic strain is slightly higher at the centre of the truncated cone in M-SPIF, numerical simulations showed that overall M-SPIF enables forming of a sheet while generating less localized plastic strain than traditional SPIF.

- The mechanics of forming in M-SPIF, including the relationships between tool and driving magnet movements, magnetic force, forming pressure, and resultant stress distribution, need to be furtherly clarified to better control the process, thus enabling the full exploitation of the process potential, such as the forming of undercuts.

- An innovative force-based numerical simulation for a M-SPIF continuous operation was developed. The numerical model, together with a magnetic force characterization for different tool/magnet setups, can represent a reliable predicting tool for M-SPIF process, which can help for a better process understanding in terms of geometrical accuracy of the formed part, stress and strain distribution, magnet/tool interaction during process, etc. Additionally, the continuous M-SPIF simulation can be used as a reverse engineering method for the development a suited experimental setup with force feedback control. This can lead to a drastic processing time and a better control of tool motion over the blank, enabling the adoption of different toolpaths for complex shape manufacturing.

5.2. Outlook and future developments

This dissertation provided an extended process analysis of two innovative SPIF variants, aiming to introduce *Multi-Directional Path* SPIF and M-SPIF as appealing options to be exploited in the optics of lightweight sheet metal alloys manufacturing.

The experimental and numerical campaigns allowed to investigate the feasibility of *Multi-Directional Path* SPIF in vertical walls processing for non-axisymmetric components, proving that current traditional SPIF limitations in the maximum achievable draw angle can be overcome by adopting different toolpath strategies. Nevertheless, the adoption of a conventional setup including a tool mounted on the spindle of a CNC machine, represents a limitation in terms of achievable workpiece areas to be processed. Both tool's vertical and lateral encumbrance reduce the applied tilt angle between the tool itself and the blank, then limiting the multi-directional approach.

In this perspective, M-SPIF process can extend the range of possible final geometries by minimizing the tool dimension. An external tool management by means of magnetic field generated by a permanent magnet can ease the evolution of traditional SPIF toolpath strategies towards multi-directional approach, leading to a full exploitation of the blank to be worked, then manufacturing complex shapes currently unmakeable with traditional processes.

Nevertheless, M-SPIF process has to be furtherly analysed in future to achieve a full comprehension of this innovative solution, as well as a better control of it. With a suited feedback control, together with a complete understanding of process parameters and their mutual interactions, the M-SPIF can act as effective solution for industrial applications, prototyping and biomedical purposes.

References

[1]   L. Lihui, L. Kangning, G. Cai, X. Yang, C. Guo, and G. Bu, "A critical review on special forming processes and associated research for lightweight components based on sheet and tube materials," *Manufacturing Review*. 2014.

[2]   K. Zheng, D. J. Politis, L. Wang, and J. Lin, "A review on forming techniques for manufacturing lightweight complex—shaped aluminium panel components," *International Journal of Lightweight Materials and Manufacture*. 2018.

[3]   T. Furuta, "Automobile applications of titanium," in *Titanium for Consumer Applications: Real-World Use of Titanium*, 2019.

[4]   Z. Huda and P. Edi, "Materials selection in design of structures and engines of supersonic aircrafts: A review," *Materials and Design*. 2013.

[5]   S. Sankaranarayanan and M. Gupta, "Emergence of god's favorite metallic element: Magnesium based materials for engineering and biomedical applications," *Mater. Today Proc.*, vol. 39, pp. 311–316, 2020.

[6]   J. Tan, "applied sciences Applications of Magnesium and Its Alloys : A Review," 2021.

[7]   M. Z. Ibrahim, A. A. D. Sarhan, F. Yusuf, and M. Hamdi, "Biomedical materials and techniques to improve the tribological, mechanical and biomedical properties of orthopedic implants – A review article," *J. Alloys Compd.*, vol. 714, pp. 636–667, 2017.

[8]   D. Zhao, F. Witte, F. Lu, J. Wang, J. Li, and L. Qin, "Current status on clinical applications of magnesium-based orthopaedic implants: A review from clinical translational perspective," *Biomaterials*, vol. 112, pp. 287–302, 2017.

[9]   T. Trzepieciński, "Recent developments and trends in sheet metal forming," *Metals (Basel).*, vol. 10, no. 6, pp. 1–53, 2020.

[10]   G. J. Dong, C. C. Zhao, and M. Y. Cao, "Flexible-die forming process with solid granule medium on sheet metal," *Trans. Nonferrous Met. Soc. China (English Ed.*, vol. 23, no. 9, pp. 2666–2677, 2013.

[11]   X. Yang, L. Lang, K. Liu, and B. Liu, "Mechanics analysis of axisymmetric thin-walled part in warm sheet hydroforming," *Chinese J. Aeronaut.*, vol. 28, no. 5, pp. 1546–1554, 2015.

[12]   G. Zhou, Y. Wang, and L. Lang, "Accuracy analysis of complex curvature parts based on the rigid-flexible hydroforming," *Int. J. Adv. Manuf. Technol.*, vol. 99, no. 1–4, pp. 247–254, 2018.

[13]   W. Hongyu, T. Fei, W. Zhen, Z. Pengchao, S. Juncai, and J. Shijun, "Simulation research about rubber pad forming of corner channel with convex or concave mould," *J. Manuf.*

Process., vol. 40, no. May 2018, pp. 94–104, 2019.

[14]   I. Irthiea, G. Green, S. Hashim, and A. Kriama, "Experimental and numerical investigation on micro deep drawing process of stainless steel 304 foil using flexible tools," *Int. J. Mach. Tools Manuf.*, vol. 76, pp. 21–33, 2014.

[15]   Q. Zhang, Z. R. Wang, and T. A. Dean, "International Journal of Machine Tools & Manufacture The mechanics of multi-point sandwich forming," vol. 48, pp. 1495–1503, 2008.

[16]   J. J. Chen, M. Z. Li, W. Liu, and C. T. Wang, "Sectional multipoint forming technology for large-size sheet metal," *Int. J. Adv. Manuf. Technol.*, vol. 25, no. 9–10, pp. 935–939, 2005.

[17]   M. Abosaf, K. Essa, A. Alghawail, A. Tolipov, S. Su, and D. Pham, "Optimisation of multi-point forming process parameters," *Int. J. Adv. Manuf. Technol.*, vol. 92, no. 5–8, pp. 1849–1859, 2017.

[18]   C. Bell, J. Corney, N. Zuelli, and D. Savings, "A state of the art review of hydroforming technology: Its applications, research areas, history, and future in manufacturing," *Int. J. Mater. Form.*, vol. 13, no. 5, pp. 789–828, 2020.

[19]   S. Bagherzadeh, M. J. Mirnia, and B. Mollaei Dariani, "Numerical and experimental investigations of hydro-mechanical deep drawing process of laminated aluminum/steel sheets," *J. Manuf. Process.*, vol. 18, pp. 131–140, 2015.

[20]   S. H. Zhang and J. Danckert, "Development of hydro-mechanical deep drawing," *J. Mater. Process. Technol.*, vol. 83, no. 1–3, pp. 14–25, 1998.

[21]   O. Music, J. M. Allwood, and K. Kawai, "A review of the mechanics of metal spinning," *J. Mater. Process. Technol.*, vol. 210, no. 1, pp. 3–23, 2010.

[22]   K. I. Ahmed, M. S. Gadala, and M. G. El-Sebaie, "Deep spinning of sheet metals," *Int. J. Mach. Tools Manuf.*, vol. 97, pp. 72–85, 2015.

[23]   M. Abd-Alrazzaq, M. Ahmed, and M. Younes, "Experimental Investigation on the Geometrical Accuracy of the CNC Multi-Pass Sheet Metal Spinning Process," *J. Manuf. Mater. Process.*, vol. 2, no. 3, p. 59, 2018.

[24]   T. Childerhouse and H. Long, "Processing maps for wrinkle free and quality enhanced parts by shear spinning," *Procedia Manuf.*, vol. 29, pp. 137–144, 2019.

[25]   S. Hatori, A. Sekiguchi, and A. Özer, "Conceptual design of multipurpose forming machine and experiments on force-controlled shear spinning of truncated cone," *Procedia Manuf.*, vol. 15, pp. 1255–1262, 2018.

[26]   Q. Xia, G. Xiao, H. Long, X. Cheng, and X. Sheng, "A review of process advancement of novel metal spinning," *Int. J. Mach. Tools Manuf.*, vol. 85, no. 381, pp. 100–121, 2014.

[27] Z. R. Han, Z. J. Fan, Y. Xiao, and Z. Jia, "The constant temperature control system of multi-pass and die-less shear spinning by flame heating," *Int. J. Adv. Manuf. Technol.*, vol. 97, no. 5–8, pp. 2439–2446, 2018.

[28] C. Brummer, S. Eck, S. Marsoner, K. Arntz, and F. Klocke, "Laser-assisted metal spinning for an efficient and flexible processing of challenging materials," *IOP Conf. Ser. Mater. Sci. Eng.*, vol. 119, no. 1, 2016.

[29] F. Niklasson, "Shear Spinning of Nickelbased Super-Alloy 718," in *Proceedings of the 9th International Symposium on Superalloy 718 {\&} Derivatives: Energy, Aerospace, and Industrial Applications*, 2018, pp. 769–778.

[30] R. Prakash and R. P. Singhal, "Shear spinning technology for manufacture of long thin wall tubes of small bore," *J. Mater. Process. Tech.*, vol. 54, no. 1–4, pp. 186–192, 1995.

[31] E. Leszak, "Apparatus and process for incremental dieless forming," *Google.Com*, p. 19, 1967.

[32] J. R. Duflou *et al.*, "Single point incremental forming: state-of-the-art and prospects," *International Journal of Material Forming*. 2018.

[33] A. K. Behera, R. A. de Sousa, G. Ingarao, and V. Oleksik, "Single point incremental forming: An assessment of the progress and technology trends from 2005 to 2015," *Journal of Manufacturing Processes*. 2017.

[34] J. Jeswiet, F. Micari, G. Hirt, A. Bramley, J. Duflou, and J. Allwood, "Asymmetric single point incremental forming of sheet metal," *CIRP Ann. - Manuf. Technol.*, 2005.

[35] L. Filice, L. Fratini, and F. Micari, "Analysis of material formability in incremental forming," *CIRP Annals - Manufacturing Technology*. 2002.

[36] M. B. Silva, M. Skjoedt, P. A. F. Martins, and N. Bay, "Revisiting the fundamentals of single point incremental forming by means of membrane analysis," *Int. J. Mach. Tools Manuf.*, 2008.

[37] J. Jeswiet and E. Hagan, "Rapid proto-typing of a headlight with sheet metal," in *Technical Paper - Society of Manufacturing Engineers. MF*, 2002, no. MR02-205, pp. 1–6.

[38] L. Filice, L. Fratini, and F. Micari, "Analysis of material formability in incremental forming," *CIRP Ann. - Manuf. Technol.*, vol. 51, no. 1, pp. 199–202, 2002.

[39] R. Aerens, P. Eyckens, A. Van Bael, and J. R. Duflou, "Force prediction for single point incremental forming deduced from experimental and FEM observations," *Int. J. Adv. Manuf. Technol.*, 2010.

[40] S. R. Marabuto, D. Afonso, J. A. F. Ferreira, F. Q. Melo, M. Martins, and R. J. De Alves Sousa, "Finding the best machine for SPIF operations. A brief discussion," *Key Eng. Mater.*,

vol. 473, pp. 861–868, 2011.

[41] G. Ambrogio, F. Gagliardi, S. Bruschi, and L. Filice, "On the high-speed Single Point Incremental Forming of titanium alloys," *CIRP Ann. - Manuf. Technol.*, vol. 62, no. 1, pp. 243–246, 2013.

[42] H. Vanhove, A. Mohammadi, Y. Guo, and J. R. Duflou, "High-speed single point incremental forming of an automotive aluminium alloy," *Key Eng. Mater.*, vol. 622–623, pp. 433–439, 2014.

[43] B. Lu *et al.*, "Mechanism investigation of friction-related effects in single point incremental forming using a developed oblique roller-ball tool," *Int. J. Mach. Tools Manuf.*, vol. 85, pp. 14–29, 2014.

[44] N. G. Azevedo, J. S. Farias, R. P. Bastos, P. Teixeira, J. P. Davim, and R. J. Alves de Sousa, "Lubrication aspects during Single Point Incremental Forming for steel and aluminum materials," *Int. J. Precis. Eng. Manuf.*, vol. 16, no. 3, pp. 589–595, 2015.

[45] J. R. Duflou, B. Callebaut, J. Verbert, and H. De Baerdemaeker, "Laser assisted incremental forming: Formability and accuracy improvement," *CIRP Ann. - Manuf. Technol.*, vol. 56, no. 1, pp. 273–276, 2007.

[46] V. U. Brussel and K. U. Leuven, "Development of an Inverse Method for Identification," no. May, 2007.

[47] A. Bhattacharya, K. Maneesh, N. Venkata Reddy, and J. Cao, "Formability and surface finish studies in single point incremental forming," *J. Manuf. Sci. Eng. Trans. ASME*, vol. 133, no. 6, pp. 1–8, 2011.

[48] F. Micari, G. Ambrogio, and L. Filice, "Shape and dimensional accuracy in Single Point Incremental Forming: State of the art and future trends," *J. Mater. Process. Technol.*, vol. 191, no. 1–3, pp. 390–395, 2007.

[49] K. Essa and P. Hartley, "An assessment of various process strategies for improving precision in single point incremental forming," *Int. J. Mater. Form.*, vol. 4, no. 4, pp. 401–412, 2011.

[50] J. R. Duflou, B. Callebaut, J. Verbert, and H. De Baerdemaeker, "Improved SPIF performance through dynamic local heating," *Int. J. Mach. Tools Manuf.*, vol. 48, no. 5, pp. 543–549, 2008.

[51] A. Mohammadi, H. Vanhove, A. Kumar Behera, A. Van Bael, and J. R. Duflou, "In-process hardening in laser supported incremental sheet metal forming," *Key Eng. Mater.*, vol. 504–506, pp. 827–832, 2012.

[52] A. K. Behera and H. Ou, "Effect of stress relieving heat treatment on surface topography and dimensional accuracy of incrementally formed grade 1 titanium sheet parts," *Int. J. Adv.*

Manuf. Technol., vol. 87, no. 9–12, pp. 3233–3248, 2016.

[53]   G. Hussain, L. Gao, N. Hayat, and L. Qijian, "The effect of variation in the curvature of part on the formability in incremental forming: An experimental investigation," *Int. J. Mach. Tools Manuf.*, vol. 47, no. 14, pp. 2177–2181, 2007.

[54]   M. B. Silva, M. Skjoedt, N. Bay, and P. A. F. Martins, "Revisiting single-point incremental forming and formability/failure diagrams by means of finite elements and experimentation," *J. Strain Anal. Eng. Des.*, 2009.

[55]   P. Eyckens, *Formability in incremental sheet forming: Generalization of the Marciniak-Kuczynski model*, no. May. 2010.

[56]   K. Jackson and J. Allwood, "The mechanics of incremental sheet forming," *J. Mater. Process. Technol.*, vol. 209, no. 3, pp. 1158–1174, 2009.

[57]   R. Malhotra, L. Xue, T. Belytschko, and J. Cao, "Mechanics of fracture in single point incremental forming," *J. Mater. Process. Technol.*, vol. 212, no. 7, pp. 1573–1590, 2012.

[58]   M. B. Silva, P. S. Nielsen, N. Bay, and P. A. F. Martins, "Failure mechanisms in single-point incremental forming of metals," *Int. J. Adv. Manuf. Technol.*, 2011.

[59]   W. C. Emmens and A. H. van den Boogaard, "An overview of stabilizing deformation mechanisms in incremental sheet forming," *J. Mater. Process. Technol.*, vol. 209, no. 8, pp. 3688–3695, 2009.

[60]   W. C. Emmens, G. Sebastiani, and A. H. van den Boogaard, "The technology of Incremental Sheet Forming-A brief review of the history," *J. Mater. Process. Technol.*, vol. 210, no. 8, pp. 981–997, 2010.

[61]   X. Shi, L. Gao, H. Khalatbari, Y. Xu, H. Wang, and L. Jin, "Electric hot incremental forming of low carbon steel sheet: Accuracy improvement," *Int. J. Adv. Manuf. Technol.*, vol. 68, no. 1–4, pp. 241–247, 2013.

[62]   S. W. Kim, Y. S. Lee, S. H. Kang, and J. H. Lee, "Incremental forming of Mg alloy sheet at elevated temperatures," *J. Mech. Sci. Technol.*, vol. 21, no. 10, pp. 1518–1522, 2007.

[63]   G. Palumbo and M. Brandizzi, "Experimental investigations on the single point incremental forming of a titanium alloy component combining static heating with high tool rotation speed," *Mater. Des.*, vol. 40, pp. 43–51, 2012.

[64]   A. Mohammadi, H. Vanhove, A. Van Bael, and J. R. Duflou, "Towards accuracy improvement in single point incremental forming of shallow parts formed under laser assisted conditions," *Int. J. Mater. Form.*, vol. 9, no. 3, pp. 339–351, 2016.

[65]   A. Mohammadi, H. Vanhove, A. Van Bael, M. Seefeldt, and J. R. Duflou, "Effect of laser transformation hardening on the accuracy of SPIF formed parts," *J. Manuf. Sci. Eng. Trans.*

ASME, vol. 139, no. 1, pp. 1–12, 2017.

[66] A. Göttmann *et al.*, "Laser-assisted asymmetric incremental sheet forming of titanium sheet metal parts," *Prod. Eng.*, vol. 5, no. 3, pp. 263–271, 2011.

[67] G. Fan, L. Gao, G. Hussain, and Z. Wu, "Electric hot incremental forming: A novel technique," *Int. J. Mach. Tools Manuf.*, vol. 48, no. 15, pp. 1688–1692, 2008.

[68] G. Ambrogio, L. Filice, and F. Gagliardi, "Formability of lightweight alloys by hot incremental sheet forming," *Mater. Des.*, vol. 34, pp. 501–508, 2012.

[69] Y. H. Ji and J. J. Park, "Formability of magnesium AZ31 sheet in the incremental forming at warm temperature," *J. Mater. Process. Technol.*, vol. 201, no. 1–3, pp. 354–358, 2008.

[70] Y. H. Ji and J. J. Park, "Incremental forming of free surface with magnesium alloy AZ31 sheet at warm temperatures," *Trans. Nonferrous Met. Soc. China (English Ed.*, vol. 18, no. SPEC. ISSUE 1, pp. s165–s169, 2008.

[71] G. Ambrogio, L. Filice, and G. L. Manco, "Warm incremental forming of magnesium alloy AZ31," *CIRP Ann. - Manuf. Technol.*, vol. 57, no. 1, pp. 257–260, 2008.

[72] L. Galdos, E. S. De Argandoña, I. Ulacia, and G. Arruebarrena, "Warm incremental forming of magnesium alloys using hot fluid as heating media," *Key Eng. Mater.*, vol. 504–506, pp. 815–820, 2012.

[73] T. A. Perkins, T. J. Kronenberger, and J. T. Roth, "Metallic forging using electrical flow as an alternative to warm/hot working," *J. Manuf. Sci. Eng. Trans. ASME*, vol. 129, no. 1, pp. 84–94, 2007.

[74] J. Magargee, R. Fan, and J. Cao, "Analysis and observations of current density sensitivity and thermally activated mechanical behavior in electrically-assisted deformation," *J. Manuf. Sci. Eng. Trans. ASME*, vol. 135, no. 6, pp. 1–8, 2013.

[75] D. Adams and J. Jeswiet, "Single-point incremental forming of 6061-T6 using electrically assisted forming methods," *Proc. Inst. Mech. Eng. Part B J. Eng. Manuf.*, vol. 228, no. 7, pp. 757–764, 2014.

[76] M. Ham and J. Jeswiet, "Forming limit curves in single point incremental forming," *CIRP Ann. - Manuf. Technol.*, 2007.

[77] S. Matsubara, "A computer numerically controlled dieless incremental forming of a sheet metal," *Proc. Inst. Mech. Eng. Part B J. Eng. Manuf.*, 2001.

[78] D. Young and J. Jeswiet, "Wall thickness variations in single-point incremental forming," in *Proceedings of the Institution of Mechanical Engineers, Part B: Journal of Engineering Manufacture*, 2004.

[79] J. R. Duflou *et al.*, "Process window enhancement for single point incremental forming

through multi-step toolpaths," *CIRP Ann. - Manuf. Technol.*, 2008.

[80] M. Skjoedt, M. B. Silva, P. A. F. Martins, and N. Bay, "Strategies and limits in multi-stage single-point incremental forming," *J. Strain Anal. Eng. Des.*, 2010.

[81] M. Skjoedt, N. Bay, B. Endelt, and G. Ingarao, "Multi stage strategies for single point incremental forming of a cup," *Int. J. Mater. Form.*, 2008.

[82] Z. Liu, Y. Li, and P. A. Meehan, "Vertical wall formation and material flow control for incremental sheet forming by revisiting multistage deformation path strategies," *Mater. Manuf. Process.*, 2013.

[83] D. Xu, R. Malhotra, N. V. Reddy, J. Chen, and J. Cao, "Analytical prediction of stepped feature generation in multi-pass single point incremental forming," in *Journal of Manufacturing Processes*, 2012.

[84] G. Buffa, M. Gucciardi, L. Fratini, and F. Micari, "Multi-directional vs. mono-directional multi-step strategies for single point incremental forming of non-axisymmetric components," *J. Manuf. Process.*, 2020.

[85] I. M. Russo, C. J. Cleaver, J. M. Allwood, and E. G. Loukaides, "The influence of part asymmetry on the achievable forming height in multi-pass spinning," *J. Mater. Process. Technol.*, 2020.

[86] S. Tanaka, "Incremental sheet metal formed square-cup obtained through multi-stepped process," in *Procedia Manufacturing*, 2018.

[87] X. Shi, G. Hussain, G. Zha, M. Wu, and F. Kong, "Study on formability of vertical parts formed by multi-stage incremental forming," *Int. J. Adv. Manuf. Technol.*, 2014.

[88] K. Kitazawa and M. Nakane, "Hemi-ellipsoidal stretch-expanding of aluminum sheet by CNC incremental forming process with two path method," *Keikinzoku/Journal Japan Inst. Light Met.*, 1997.

[89] P. A. F. Martins, N. Bay, M. Skjoedt, and M. B. Silva, "Theory of single point incremental forming," *CIRP Ann. - Manuf. Technol.*, 2008.

[90] H. Meier, B. Buff, R. Laurischkat, and V. Smukala, "Increasing the part accuracy in dieless robot-based incremental sheet metal forming," *CIRP Ann. - Manuf. Technol.*, vol. 58, no. 1, pp. 233–238, 2009.

[91] Z. Liu, "Heat-assisted incremental sheet forming: a state-of-the-art review," *Int. J. Adv. Manuf. Technol.*, vol. 98, no. 9–12, pp. 2987–3003, 2018.

[92] G. Buffa, D. Campanella, and L. Fratini, "On the improvement of material formability in SPIF operation through tool stirring action," *Int. J. Adv. Manuf. Technol.*, vol. 66, no. 9–12, pp. 1343–1351, 2013.

[93]   G. Buffa, D. Campanella, R. Mirabile, and L. Fratini, "Improving formability in SPIF processes through high speed rotating tool: Experimental and numerical analysis," in *Key Engineering Materials*, 2013.

[94]   M. Kleiner, C. Beerwald, and W. Homberg, "Analysis of process parameters and forming mechanisms within the electromagnetic forming process," *CIRP Ann. - Manuf. Technol.*, vol. 54, no. 1, pp. 225–228, 2005.

[95]   X. H. Cui *et al.*, "Electromagnetic incremental forming (EMIF): A novel aluminum alloy sheet and tube forming technology," *J. Mater. Process. Technol.*, 2014.

[96]   X. Cui, J. Mo, J. Li, X. Xiao, B. Zhou, and J. Fang, "Large-scale sheet deformation process by electromagnetic incremental forming combined with stretch forming," *J. Mater. Process. Technol.*, vol. 237, pp. 139–154, 2016.

[97]   J. TAN, M. ZHAN, and H. LI, "Dependence on forming parameters of an integral panel during the electromagnetic incremental forming process," *Chinese J. Aeronaut.*, vol. 31, no. 7, pp. 1625–1634, 2018.

[98]   H. wei Li, X. Yao, S. liang Yan, J. He, M. Zhan, and L. Huang, "Analysis of forming defects in electromagnetic incremental forming of a large-size thin-walled ellipsoid surface part of aluminum alloy," *J. Mater. Process. Technol.*, vol. 255, no. July 2017, pp. 703–715, 2018.

[99]   K. Guo, X. Lei, M. Zhan, and J. Tan, "Electromagnetic incremental forming of integral panel under different discharge conditions," *J. Manuf. Process.*, vol. 28, pp. 373–382, 2017.

[100]   L. Qiu, Y. Yu, Z. Wang, Y. Yang, Y. Yang, and P. Su, "Analysis of electromagnetic force and deformation behavior in electromagnetic forming with different coil systems," *Int. J. Appl. Electromagn. Mech.*, vol. 57, no. 3, pp. 337–345, 2018.

[101]   V. Psyk, D. Risch, B. L. Kinsey, A. E. Tekkaya, and M. Kleiner, "Electromagnetic forming - A review," *J. Mater. Process. Technol.*, vol. 211, no. 5, pp. 787–829, 2011.

[102]   G. Buffa, H. Yamaguchi, M. Gucciardi, D. Pinard, and L. Fratini, "Magnetic field-assisted single-point incremental forming with a magnet ball tool," *CIRP Ann.*, vol. 70, no. 1, pp. 265–268, 2021.

[103]   M. Gucciardi, D. Benson, L. Fratini, G. Buffa, and H. Yamaguchi, "Development of Magnetic Field-Assisted Single-Point Incremental Forming," *Key Eng. Mater.*, vol. 883, pp. 189–194, 2021.

Publications List

[1]   G. Buffa, M. Gucciardi, L. Fratini, and F. Micari, "Multi-directional vs. mono-directional multi-step strategies for single point incremental forming of non-axisymmetric components," J. Manuf. Process., 2020.

[2]   M. Gucciardi, D. Benson, L. Fratini, G. Buffa, and H. Yamaguchi, "Development of Magnetic Field-Assisted Single-Point Incremental Forming," Key Eng. Mater., vol. 883, pp. 189–194, 2021.

[3]   G. Buffa, H. Yamaguchi, M. Gucciardi, D. Pinard, and L. Fratini, "Magnetic field-assisted single-point incremental forming with a magnet ball tool," CIRP Ann., vol. 70, no. 1, pp. 265–268, 2021.

[4]   A. Latif, M. Gucciardi, G. Ingarao, and L. Fratini, "Outlining the Limits of Friction Stir Consolidation as Used as an Aluminum Alloys Recycling Approach," in Sustainable Design and Manufacturing, 2022, pp. 169–180.